Studying the structural phase transition of organic $Cu(DCNQI)_2$ with ultrafast electron diffraction

by

Nancy Payne

Thesis presented in partial fulfilment of the requirements for the degree of Master of Science in Laser Physics in the Physics Department at Stellenbosch University

Supervisors: Prof. Heinrich Schwoerer
Prof. Jens Pflaum

December 2017

Declaration

By submitting this thesis electronically, I declare that the entirety of the work contained therein is my own, original work, that I am the sole author thereof (save to the extent explicitly otherwise stated), that reproduction and publication thereof by Stellenbosch University will not infringe any third party rights and that I have not previously in its entirety or in part submitted it for obtaining any qualification.

Date: December 2017 .....

Abstract

Studying the structural phase transition of organic $Cu(DCNQI)_2$ with ultrafast electron diffraction

N. E. Payne

Department of Physics,
University of Stellenbosch,
Private Bag X1, Matieland 7602, South Africa.

Thesis: MSc

September 2017

Organic molecular solids combine the richness of molecular and solid state physics. The structure and properties of organic solids can be modified to a great extent—for example, by utilising isotope effects, addition of side chains, and forming alloys—resulting in a highly tailorable group of materials with a wide range of anisotropic electrical, magnetic and optical properties. The radical-ion salts of copper-dicyanoquinonediimine [$Cu(DCNQI)_2$] are an excellent example, exhibiting high one-dimensional electrical conductivities at room temperature and abrupt metal-insulator transitions upon cooling of more than six orders of magnitude. The reverse insulator-metal transition can be photoinduced using an ultrashort optical laser pulse, turning the crystal from a plastic-like insulator to a metal-like conductor within 10^{-12} seconds. This phase transition is associated with structural changes of the crystal lattice which can be observed using ultrafast electron diffraction (UED).

This thesis describes the preparation of high quality 50 nm thick samples of monocrystalline $Cu(Me,Br\text{-}DCNQI)_2$ by use of an ultramicrotome, the experimental setup and procedure, and the preliminary results of our UED experiments. The crystal lattice dynamics associated with the insulator-metal transition are studied in two regimes: 1) just below the phase transition temperature, and 2) far below the phase transition temperature. Time-resolved experiments allow direct observation of the structural changes at an atomic level and on the primary timescales of lattice dynamics. This sheds light on the driving forces behind the phase transition in different regimes, and the coupling strengths between electronic and vibrational degrees of freedom and their role in facilitating the insulator-metal transition.

Uittreksel

Bestudering van strukturuele fase verandering van organiese $Cu(DCNQI)_2$ met ultra-vinnige elektron diffraksie

("Studying the structural phase transition of organic $Cu(DCNQI)_2$ with ultrafast electron diffraction")

N. E. Payne

Departement Fisika,
Universiteit van Stellenbosch,
Privaatsak X1, Matieland 7602, Suid Afrika.

Tesis: MSc

September 2017

Die struktuur en eienskappe van organiese vaste stowwe kan tot 'n groot mate verander word, wat hoogs 'n aanpasbare groep materiale met 'n wye verskeidenheid anitroop elektriese, magnetiese en optiese eienskappe moontlik maak. Die radikale ioon soute van $Cu(DCNQI)_2$ is 'n uitstekende voorbeeld. Hierdie sout besit hoë een-dimensiÃ≪le elektriese geleidingsvermoë by kamer temperatuur en die vermoë om skielik om te skakel van geleier na nie-geleibare materiaal tydens die verkoeling van ongeveer ses ordes van grote. Die teenoorgestelde verandering kan deur lig geïduseer word deur middel van ultra-vinnige laser pulse, wat die sout kristal verander van 'n plastiekagtige nie-geleier na 'n metaalagtige geleier binne 10^{-12} sekondes. Hierdie fase verandering word gëassosieer met strukturuele veranderinge van die kristalrooster wat waar geneem kan word deur ultra-vinnige elektron diffraksie (UED).

Hierdie teseis beskryf die voorbereiding van hoë kwaliteit 50 nm dikte skyfies, van mono-laag $Cu(Me,Br\text{-}DCNQI)_2$ deur gebruik te maak van 'n ultra-mikrotoom, die eksperimentele opstelling en prosedure, en die voorlopige resultate van ons UED eksperimente. Die kristalrooster dinamika gëassosieer met die nie-geleier-geleier verandering word bestudeer in twee kenmerkende toestande: een, net onder die fase veranderings temperatuure, en twee, vêr onder die fase veranderings temperatuur. Eksperimente met tyd opgeloste resolusie stel ons in staat om die stukturuele veranderinge direk waar te neem op 'n atomiese vlak en op die primêre tydskaal van die rooster dinamika. Dit stel ons ook in staat om meer te weet van die dryfkragte agter die fase verandering in die verskillende regimes, en die koppeling tussen elektroniese en vibrasionelegrade van vryheid en hul rol in die fasilitering van die nie-geleier-geleier verandering.

Acknowledgements

First and foremost, a huge thank you to Heinrich and Bart for all the fun, patience and support over the last few years. It's been incredibly rewarding working with you guys, and I'm a better person and researcher because of it. Thank you!

Many thanks to everyone who has made the lab, office and department such a great environment to work in: Essraa, Anneke, Ruan, Iulia, Neway and Olufemi, and all the lovely members of the Laser Research Institute. An extra special thanks to the fantastic technical support of the physics department and their many contributions to our project, and Lize Engelbrecht for training, advice and sympathies regarding sample prep and my rocky relationship with the ultramicrotome.

Of course, life exists outside a Master's. All my love to Indla, who made the greatest writing companion a girl could hope for, and Nick, who has put up with more physics talk than any mathematician deserves. You never know, some of it might come up in a pub quiz one day.

Contents

1. Motivation

Organic molecular crystals are an exciting class of materials that take advantage of the versatile nature of organic molecules, which remain largely intact within the crystal lattice and thus contribute to the macroscopic properties of the solid. However, the incorporation of molecules into a periodic structure can give rise to further characteristics due to intermolecular bonding. For example, the conductivities of organic solids range from insulating to semi-conducting to superconducting [1]. Interestingly, the macroscopic properties of organic solids can be tuned by making precise changes to the molecular structure through the addition of rest groups, side chains, isotope effects, and so on. Such modifications allow investigation into a wealth of materials with tunable optical, electronic and magnetic properties.

Furthermore, due to the periodic nature of crystals, the atomic-level structure of organic solids can be resolved using techniques such as x-ray crystallography, revealing the structure of complex molecules such as drugs and their receptor proteins [2]. Ultrafast electron diffraction (UED) experiments take the investigations a step further by combining atomic-level spatial resolution with sub-100 femtosecond to picosecond temporal resolution. Although UED is not suitable for a full structural analysis of crystalline materials, it can be combined with the equilibrium structural data obtained from x-ray crystallography to yield information on the structural *changes* in non-equilibrium situations. This grants access to the study of a huge range of chemical processes on their primary timescales, such as ring-opening reactions [3], with potential to study biological processes such as conformation changes in receptor proteins or the light-harvesting complexes involved in photosynthesis.

A particularly interesting class of quasi-one-dimensional organic molecular solids were discovered in the 1970s, the charge density wave (CDW) conductors [4]. Depending on temperature, such materials can experience a periodic modulation of the electron density (a charge density wave) and an associated deformation of the crystal lattice (a periodic lattice distortion). The formation of a CDW is associated with the opening of a band gap as theorised by Peierls in 1930, thus such a phase transition is also known as a Peierls transition. An example of CDW conductors are the radical-ion salts of $Cu^{+}(DCNQI)_2^{-}$, which initially attracted interest due to the extremely high one-dimensional conductivity of Cu(DMe-DCNQI)$_2$ (DMe indicates two CH_3 rest groups) [5]. Partial deuteration of the hydrogens on the $DCNQI^{-}$ molecules causes the salt to undergo a dramatic metal-to-insulator Peierls transition upon cooling [6], where the extent of deuteration has a systematic effect on the phase transition temperature. The reverse insulator-to-metal transition can be photoinduced on ultrafast timescales [7], which could lead to potential applications in ultrafast optical switches in nanoelectronics.

However, although the macroscopic electronic properties of Cu(DCNQI)$_2$ salts have been well studied, the microscopic origins of such dramatic behaviour can only be indirectly inferred (for example, from electron spin resonance measurements). UED experiments aim to shed light on the microscopic details of the structural phase tran-

sition by directly observing the atomic motions of the crystal lattice on the primary timescales of the structural and electronic changes. Combined with complimentary studies such as ultrafast conductivity measurements, UED experiments help in developing a deeper understanding of the relationship between electronic and vibrational degrees of freedom within the crystal and their link to the phase transition.

To set the scene for our experimental results, first the structure and properties of $Cu(DCNQI)_2$ are examined in detail in Chapter 2, followed by a brief introduction to diffraction theory and crystal structure in Chapter 3. An in-depth description of the experimental setup and procedure is offered in Chapter 4, including a comprehensive discussion of the sample preparation procedure. Finally, Chapter 5 presents the results of both temperature-dependent and time-resolved studies on $Cu(Me,Br\text{-}DCNQI)_2$. Some preliminary discussion on a real-space interpretation of the time-resolved data will conclude the work.

2. Radical-ion salts of $Cu(DCNQI)_2$

The radical-ion salts of M(2,5-R_1,R_2-dicyanoquinonediimine)$_2$ (denoted by M(R_1,R_2-DCNQI)$_2$) exhibit a high one-dimensional conductivity at room temperature and (in the case of M = Cu) can undergo a structural metal-to-insulator transition upon cooling. The insulator-to-metal transition can be photoinduced [7], and with ultrafast electron diffraction (UED) we are able to study the resulting structural dynamics of the crystal lattice associated with the insulator-to-metal transition. This chapter covers the properties of the Cu(R_1,R_2-DCNQI)$_2$ salts and offer experimental evidence of ultrafast photoswitching of the insulator-to-metal transition, indicating the suitability of Cu(R_1,R_2-DCNQI)$_2$ as a candidate for study with UED.

2.1 Structure and conductivity of M(R_1,R_2-DCNQI)$_2$ salts

The structure of M(R_1,R_2-DCNQI)$_2$ is shown in Figure 2.1 and consists of 2,5-disubstituted R_1,R_2-DCNQI molecules (from now on referred to as DCNQI) interconnected by metal ions (M = Cu, Ag, Li, Na, K, Tl, and NH_4) [8; 9; 10]. In this thesis I focus

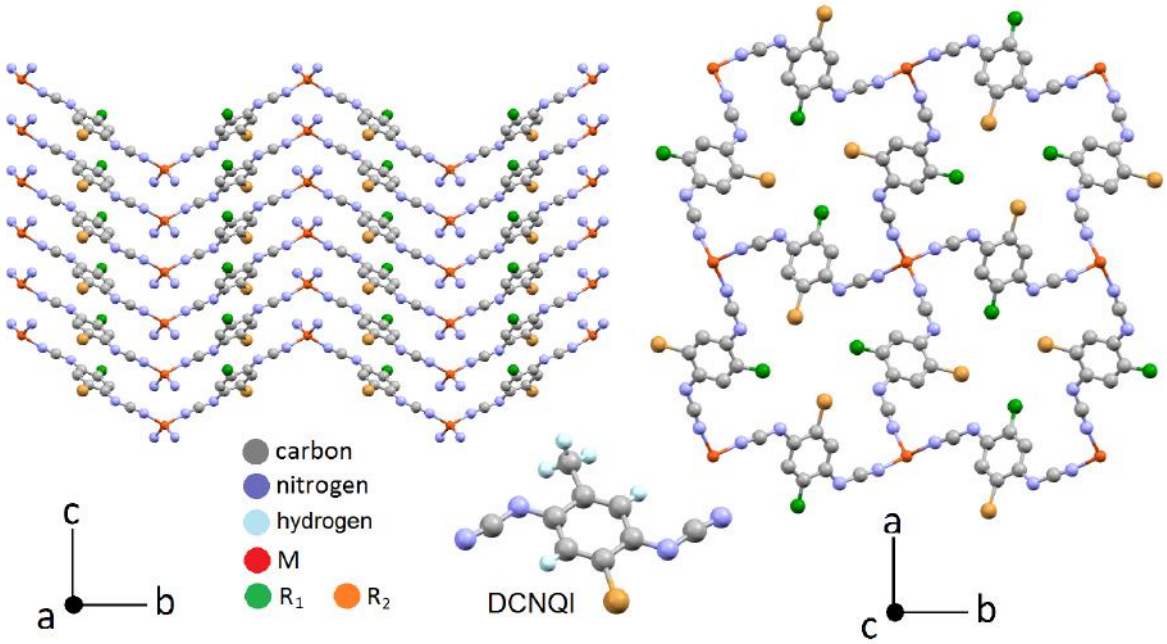

Figure 2.1: Left: The stacking structure of M(R_1,R_2-DCNQI)$_2$ salts (hydrogens removed). The stacking axis is the *c* crystal axis. **Right:** A projection of the *a*-*b* plane of the unit cell of M(R_1,R_2-DCNQI)$_2$, where the central metal ions (red) can be Cu, Ag, Li, Na, K, Tl and NH_4, and the rest groups (green and gold) can be CH_3 (Me), CH_3O (MeO), Cl, Br and I (hydrogens removed). A single R_1,R_2-DCNQI molecule where R_1 = CH_3 is also shown; each hydrogen can be replaced with a deuterium atom. The crystal structure of M(R_1,R_2-DCNQI)$_2$ was obtained from x-ray diffraction experiments by the Barbour Group, Stellenbosch University.

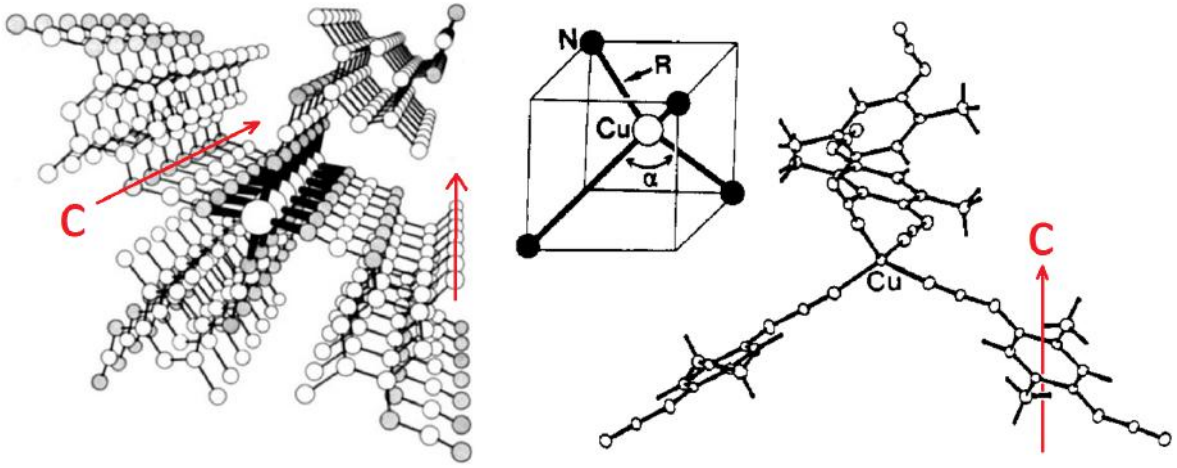

Figure 2.2: Left: A perspective view of the crystal structure of M(R$_1$,R$_2$-DCNQI)$_2$ around the *c* axis, which is parallel to the M–M chain and the DCNQI stacks (adapted from [5]). **Centre and right:** The tetrahedral geometry around the metal ion (e.g., M = Cu), emphasising the different orientations of the DCNQI rings with respect to the *c* axis (adapted from [11]).

on the Cu salts due to their exotic properties. Possible rest groups on the DCNQI molecules are R$_1$, R$_2$ = CH$_3$ (Me), CH$_3$O (MeO), Cl, Br and I [5]. The DCNQI molecules are inclined with respect to the *c* crystal axis and form one-dimensional columns parallel to the *c* axis, as shown in Figure 2.1 (left). A projection of the *a*-*b* plane of the unit cell (i.e., looking along the stacks) is shown in Figure 2.1 (right). The three-dimensional stacking structure is emphasised in Figure 2.2. The crystal structures shown in colour were obtained from x-ray diffraction experiments by the Barbour Group, Stellenbosch University.

In addition to the wide variety of metal ions and rest groups, isotope effects (e.g., [12; 13; 14; 6]) and alloy effects (e.g., [15; 16; 17; 18]) can also be used to tune the physical properties of Cu(R$_1$,R$_2$-DCNQI)$_2$ crystals. For example, selective deuteration of different hydrogens on the DCNQI molecule has been shown to allow particularly fine control of the electronic properties of the crystals [6]. Regarding alloys, Nishio et al. [16] found that the properties of Cu(DMe$_{1-x}$MeBr$_x$-DCNQI)$_2$ varied hugely on the extent of doping (x) with MeBr molecules. All in all, Cu(R$_1$,R$_2$-DCNQI)$_2$ salts accept a diverse range of possible constituents which result in salts that display a variety of drastically different behaviours. Importantly the difference in properties from salt to salt is systematic and understandable (as will be discussed in detail below), thus lessons learned from such crystals could lead the way towards tailor-made materials for specific applications as required.

Even though the chemical composition of Cu(R$_1$,R$_2$-DCNQI)$_2$ is highly changeable, the crystal structures of different salts have only minor differences in lattice parameters (e.g., [19]). Each metal ion is tetrahedrally coordinated to four DCNQI molecules as shown in Figure 2.2 (right). The tetrahedral geometry around the metal ion is distorted in all M(DCNQI)$_2$ salts from a "perfect" tetrahedral symmetry (T_d) to a distorted symmetry (D_{2d}). The extent of distortion in Cu(DCNQI)$_2$ can be characterised by the N–Cu–N angle α (see Figure 2.2, centre), with $\alpha = 109.5°$ indicating perfect T_d symmetry and $\alpha \neq 109.5°$ indicating a distorted symmetry. The extent of

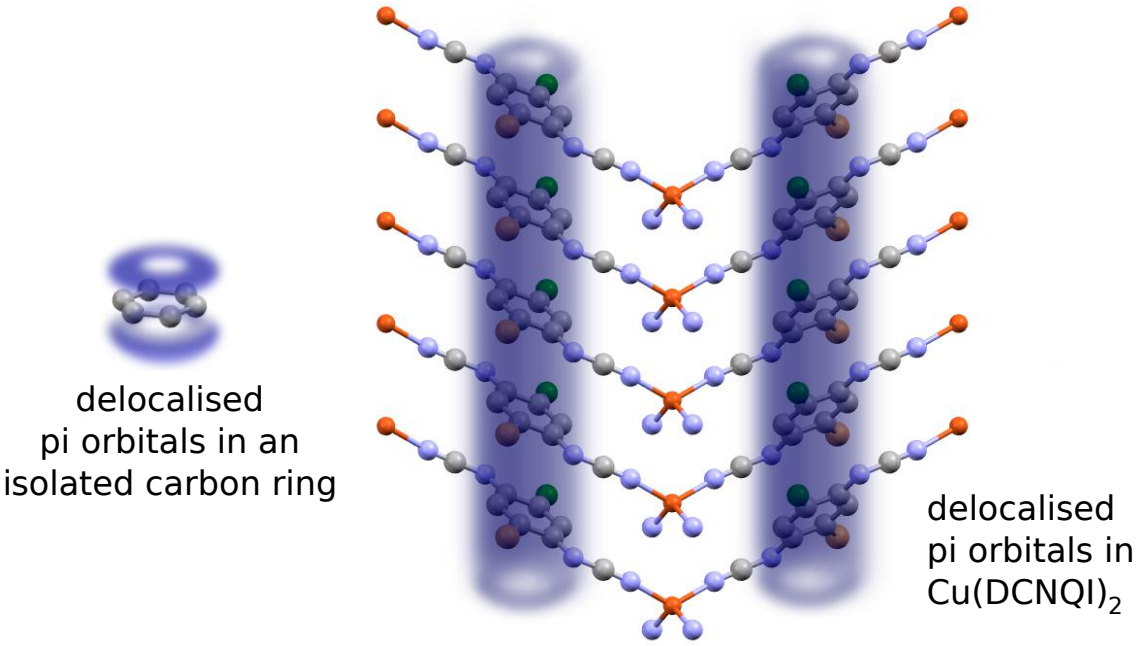

Figure 2.3: Left: The delocalised π orbital in benzene visualised in blue. **Right:** In Cu(DCNQI)$_2$ crystals, the π orbitals of the DCNQI rings overlap along the stacking axis, resulting in a delocalisation of electrons along the c axis.

distortion will prove key in explaining the electronic properties of Cu(R$_1$,R$_2$-DCNQI)$_2$ salts (e.g., [20; 13]). At room temperature and under ambient pressure, α ranges from approximately 122–127° in different salts (e.g., [19]).

All M(R$_1$,R$_2$-DCNQI)$_2$ salts are good electrical conductors along their c axis (i.e., along the DCNQI columns). For example, the conductivity of Cu(DMe-DCNQI)$_2$ along the stacking axis can reach as high as 5×10^5 S cm^{-1} at 3.5 K [5], comparable to that of copper at room temperature (6×10^5 S cm^{-1} [21]). The unusually high conductivity of Cu(DMe-DCNQI)$_2$ for an organic molecular solid is attributed to the orbitals of the DCNQI molecules (e.g., [1]). The delocalised π electrons of DCNQI form not only the usual molecular orbital above and below the six-membered carbon rings, but also overlap along the c axis as shown in Figure 2.3 (right). Thus the stacking axis is also the highly conducting axis, as electrons are delocalised across all contributing p orbitals. Conductivity along the metal ion chains does not occur as the M–M distance is relatively large. For example, the Cu–Cu distance in Cu(Me,Br-DCNQI)$_2$ is 388 pm compared to 256 pm in Cu(metal).

The Peierls transition in Cu(DCNQI)$_2$

For comparison of Cu salts to non-Cu salts, Figure 2.4 shows several representative normalised conductivities of non-Cu salts with respect to temperature. The conductivities tend to gradually decrease upon cooling and all are semi-conducting below around 80 K. However, particular Cu(DCNQI)$_2$ crystals are able to undergo an electronic phase transition upon cooling or under pressure. In fact, Cu(DCNQI)$_2$ salts can be divided into three distinct categories depending on their behaviour under ambient pressure:

- **Group I:** salts that remain metallic to low temperatures. E.g., Cu(DMe-DCNQI)$_2$.
- **Group II:** salts that undergo a single metal-to-insulator (M-I) transition upon cooling. E.g., Cu(MeBr-DCNQI)$_2$.
- **Group III:** salts that undergo a metal-to-insulator transition upon cooling, and a reentry into the metallic phase upon further cooling. E.g., Cu(DMe-DCNQI-d$_8$)$_2$, where d$_8$ indicates deuteration of all DCNQI hydrogens.

To gain some insight into this wealth of behaviours, we can consider the band structure of Cu(DCNQI)$_2$. The electronic configuration of copper is [Ar] 3d^{10} 4s^1. For a single copper ion the five d orbitals have similar energy. However, in a crystal with tetrahedral geometry (i.e., the copper ion forms bonds with four ligands), a splitting in the energy levels occurs: the two d$_{x^2-y^2}$ and d_{z^2} orbitals (labelled E_g in Figure 2.5, left) are pushed lower in energy than the d$_{xy}$, d$_{yz}$ and d$_{zx}$ orbitals (labelled T_{2g} in Figure 2.5, left). This

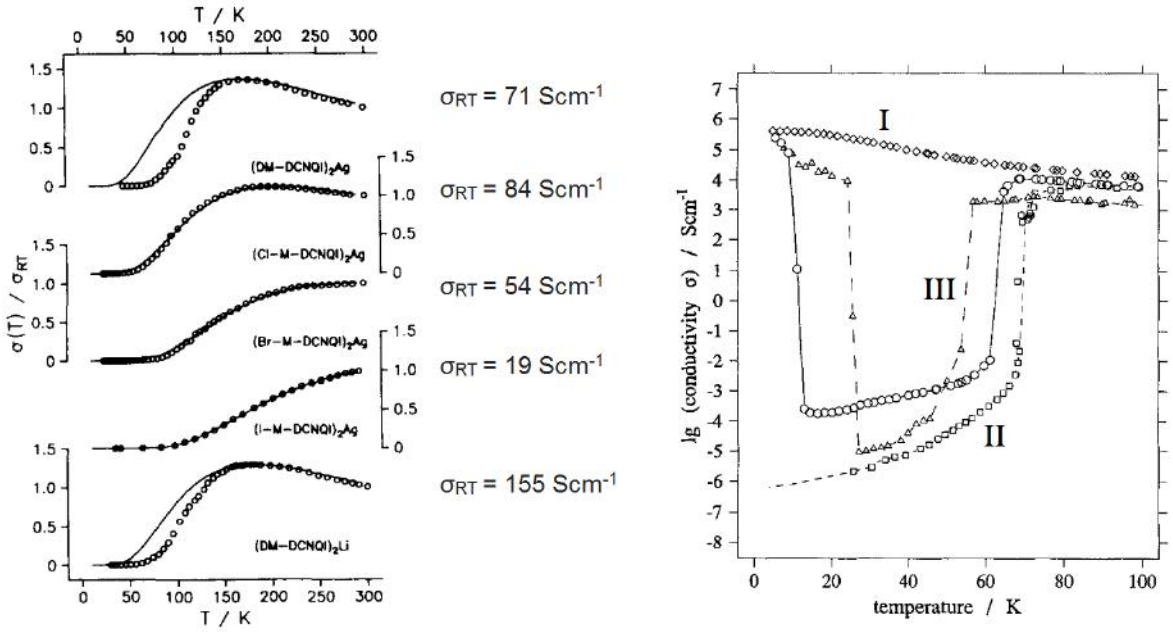

Figure 2.4: Left: The conductivity of non-Cu salts is relatively low at room temperature (around 100 S cm^{-1}) and the salts are semi-conducting below around 80 K [22]. **Right:** In contrast, Cu(DCNQI)$_2$ salts either show a metallic conductivity to low temperatures (Group I), undergo a metal-insulator transition upon cooling (Group II), or can exhibit metal-insulator-metal behaviour, with the reentry into the metallic phase upon further cooling (Group III) [23].

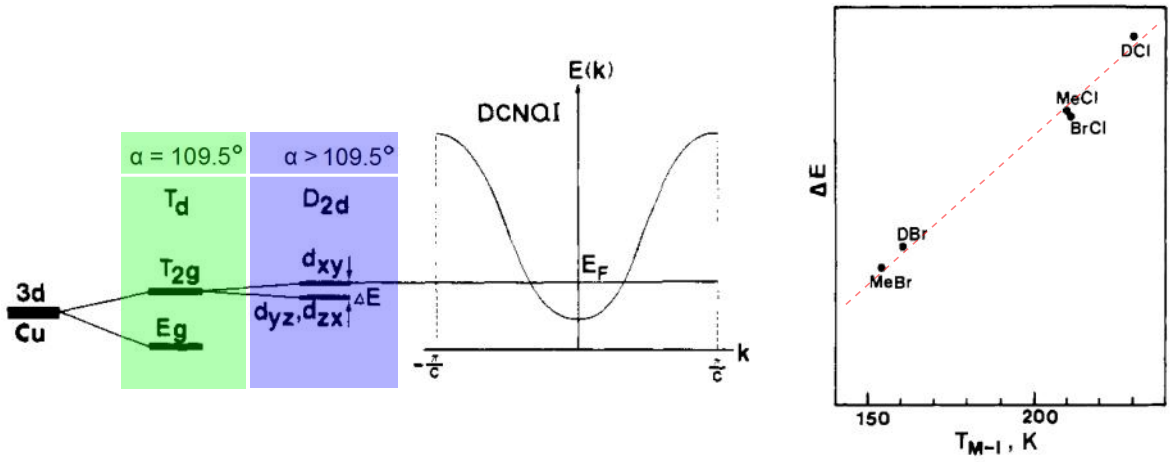

Figure 2.5: Left: The splitting of the d energy levels of the Cu ion due to distortion of the tetrahedral geometry, where T_d indicates the perfect tetrahedral geometry ($\alpha = 109.5°$) and D_{2d} indicates the distorted symmetry ($\alpha > 109.5°$ in our case). The energy splitting ΔE is related to the N–Cu–N angle α. **Right:** The clear relationship between ΔE and the M-I transition temperature T_{M-I} in various Cu(DCNQI)$_2$ salts (dashed line to guide the eye). Figures adapted from [11].

can be explained with ligand field theory and the interaction of the ligand fields with the Cu orbitals (e.g., [24]).

If the crystal has perfect tetragonal geometry ($\alpha = 109.5°$), the d_{xy}, d_{yz} and d_{zx} orbitals have equal energy. However, if the tetrahedral geometry is distorted ($\alpha > 109.5°$) as is the case for Cu(DCNQI)$_2$ crystals, the degeneracy of the d_{xy}, d_{yz} and d_{zx} orbitals is lifted: the d_{xy} orbital is pushed higher in energy and the d_{yz} and d_{zx} orbitals are pushed lower (see Figure 2.5, left). The d_{xy} orbital lies close in energy to the Fermi level of the π orbital of DCNQI, and interaction of the d_{xy} orbital with the π orbital is believed to be key in understanding the unusual behaviours of the crystal.

The difference in energy between the d_{xy} orbital and the d_{yz}, d_{zx} orbitals is denoted by ΔE and is labelled in Figure 2.5 (left). The greater the tetrahedral distortion (i.e., the larger the value of α), the greater the energy difference ΔE between the d_{xy} and d_{yz}, d_{zx} levels, which corresponds to a greater degree of electron transfer from Cu to DCNQI [19] and a greater formal charge of the Cu atom. As shown in Figure 2.5 (right), there is an excellent correlation between ΔE and the temperature at which the metal-insulator transition occurs in different Cu(DCNQI)$_2$ salts. This indicates a relationship between the electronic properties of Cu(DCNQI)$_2$ and a structural parameter in the crystal, the N–Cu–N angle α.

A consequence of the π-d interaction is that the DCNQI columns can become electronically connected to each other: depending on the exact nature of the π-d orbital interaction, the crystal can also conduct perpendicular to the stacks in addition to the conductivity along the DCNQI stacks. It has been shown that the Cu salts differ from the other metal ion salts in this regard; the ratio of conductivities parallel and perpendicular to the stacking axis in non-Cu salts is approximately 5000, but in Cu salts can be around 15 at room temperature [25]. That is, the Cu crystals are able to exhibit three-dimensional conductivity rather than just one-dimensional, due to the π-d orbital interaction.

Charge density wave formation in Cu(DCNQI)$_2$

In the high temperature metallic state, the Cu ions in Cu(DCNQI)$_2$ are known to be in a mixed valence state with a ratio of Cu^+ : $Cu^{2+} \approx 2{:}1$ from x-ray photoelectron spectroscopy (XPS) experiments (e.g., [20]). However, in the low temperature insulating phase, a localisation of the "previously itinerant" Cu^{2+} states occurs and the charge ordering becomes static: (...Cu^+ Cu^{2+} Cu^+...). That is, the electron density along the c crystal axis is modulated with a periodicity three times greater than the lattice periodicity. This modulation of electron density is called a charge density wave (CDW) and is shown schematically in Figure 2.6. The formation of a CDW is associated with an accompanying periodic lattice distortion (PLD).

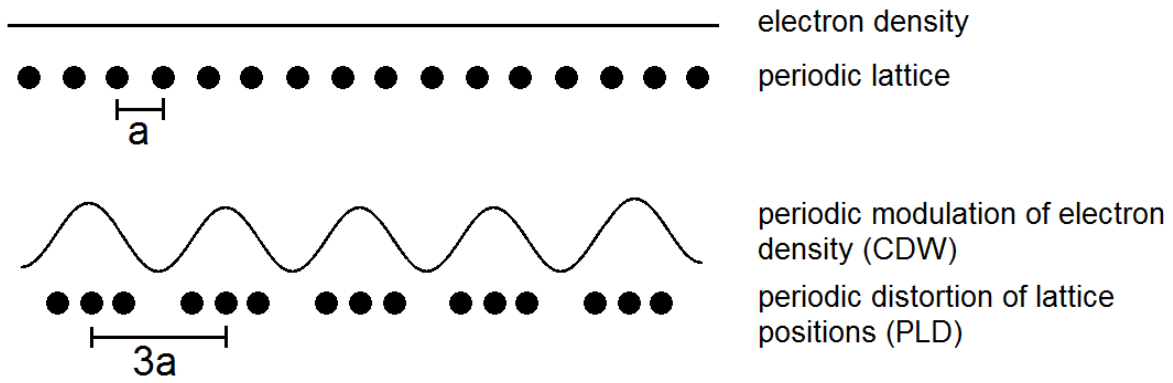

Figure 2.6: Simplified schematic to visualise the formation of a charge density wave and the associated periodic lattice distortion.

The Cu^{2+} states can be detected by electron spin resonance (ESR) and can be used to infer whether crystals are in the conducting or insulating phase. For example, von Schütz et al. [26] used simultaneous conductivity and ESR measurements to deduce that a "critical volume" is required for the crystal to undergo a phase transition: once 20% of the crystal is ESR-active (i.e., 20% of the volume has localised Cu^{2+} states), the bulk crystal experiences an abrupt M-I transition and the conductivity drops by several orders of magnitude.

Why does this metal-insulator phase transition occur in some Cu(DCNQI)$_2$ salts but not others? The formation of a charge density wave was first theorised by Peierls (the M-I transition is often referred to as a Peierls transition) and will only occur when it is energetically favourable to distort the crystal lattice in order to lower electron energies.

To explain why a Peierls transition may be energetically favourable in one-dimensional systems, we turn to band theory. As the Peierls transition occurs when Cu(DCNQI)$_2$ is a good conductor along c, the one-dimensional free electron model is a suitable starting point (where 'free' in this model refers to the fact that the electrons do not interact with anything—each other, the lattice, etc). The energy eigenstates of such a model can be found by solving the Schrödinger equation for a free particle with $V(\mathbf{r}) = 0$ and have the form of plane waves with a parabolic dispersion relation, $E = \hbar^2 k^2 / 2m$ (the dotted line in Figure 2.7) [27].

The free electron model can be extended to electrons in a periodic potential such as a crystal. For a periodic potential $V(\mathbf{r})$, it must be the case that $V(\mathbf{r}) = V(\mathbf{r} + \mathbf{a})$,

where a is the lattice constant along the relevant axis (see Section 3.2 for details on crystal structure nomenclature). The effect of applying a periodic potential to the free electron model is to multiply the plane wave energy eigenstates by a periodic function with the same periodicity of the potential. This is called Bloch's theorem. Thus in k-space (reciprocal space) the periodicity of the nearly-free electron dispersion is $2\pi/a$. To avoid degeneracies in the electron energies, band gaps appear in the dispersion curves of the nearly-free electron model, pushing states below the band gap down in energy and pushing states above the band gap up in energy (see Figure 2.7, solid line).

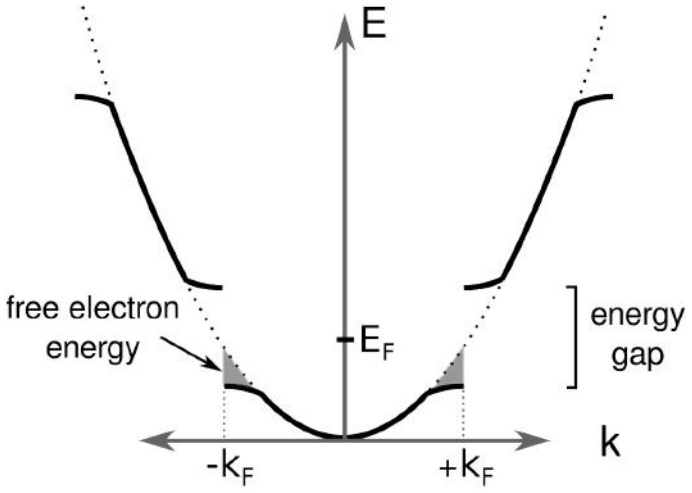

Figure 2.7: The formation of a band gap becomes energetically favourable if the energy gained from lowering the electron energies just below the Fermi surface is greater than the energy cost of modulating the lattice positions. Figure adapted from [28].

That is, if a band gap forms *at the Fermi energy*, a lower energy configuration can be achieved if the energy required for PLD formation is less than the gain in electron energy from the lowering of the band edge. The energy for PLD formation is simply the elastic energy required to modulate the lattice positions and depends on the chemical composition of the crystal. The energy gained from such a transition will only be significant if most electrons are in their ground state (i.e., few electrons are thermally excited across the band gap), meaning the Peierls transition becomes more favourable at lower temperatures.

It should be emphasised that the ability for a material to undergo a Peierls transition is based on a one-dimensional model, thus such behaviour is predicted for materials with one-dimensional (or quasi-one-dimensional) properties, such as the conductivity of Cu(DCNQI)$_2$. However, from this model it is unclear how two- or three-dimensional behaviour would affect the properties of a material and whether the the transition may be suppressed [29]. For example, the Group I Cu(DCNQI)$_2$ salts are quasi-three-dimensional to low temperatures (inferred from the ratio of the longitudinal and transverse conductivity, $\sigma_\parallel$ and $\sigma_\perp$) and remain conducting to low temperature—the Peierls transition is suppressed by the three-dimensional nature of the conductivity.

Experimental observation of the insulating phase

A periodic lattice distortion can be directly observed by electron (or x-ray) diffraction. In Cu(DCNQI)$_2$ the PLD results in the DCNQI layers "trimerising" along the c axis and grouping into sets of three, shown schematically in Figure 2.8 (top right). A tripling of the periodicity along c in real space results in a third of the periodicity along c^* in reciprocal space, thus so-called 'trimer' peaks will appear along c^* in the diffraction pattern at one third of the distance between the main Bragg peaks. Figure 2.8 shows the steady-state electron diffraction patterns of our particular sample Cu(Me,Br-DCNQI)$_2$ at room temperature (left) and below the phase transition temperature (right) (see Chapter 4 for experimental details). A number of trimer peaks are clearly visible in the cold image, appearing at one third of the lattice constant c^*, and are (as far as we know) the first observation of such trimer peaks by electron diffraction. Once these trimer peaks have been observed we know that the sample has undergone the PLD associated with the M-I transition.

Such trimer peaks have also been observed in x-ray diffraction experiments [30; 8], with an example shown in Figure 2.9.

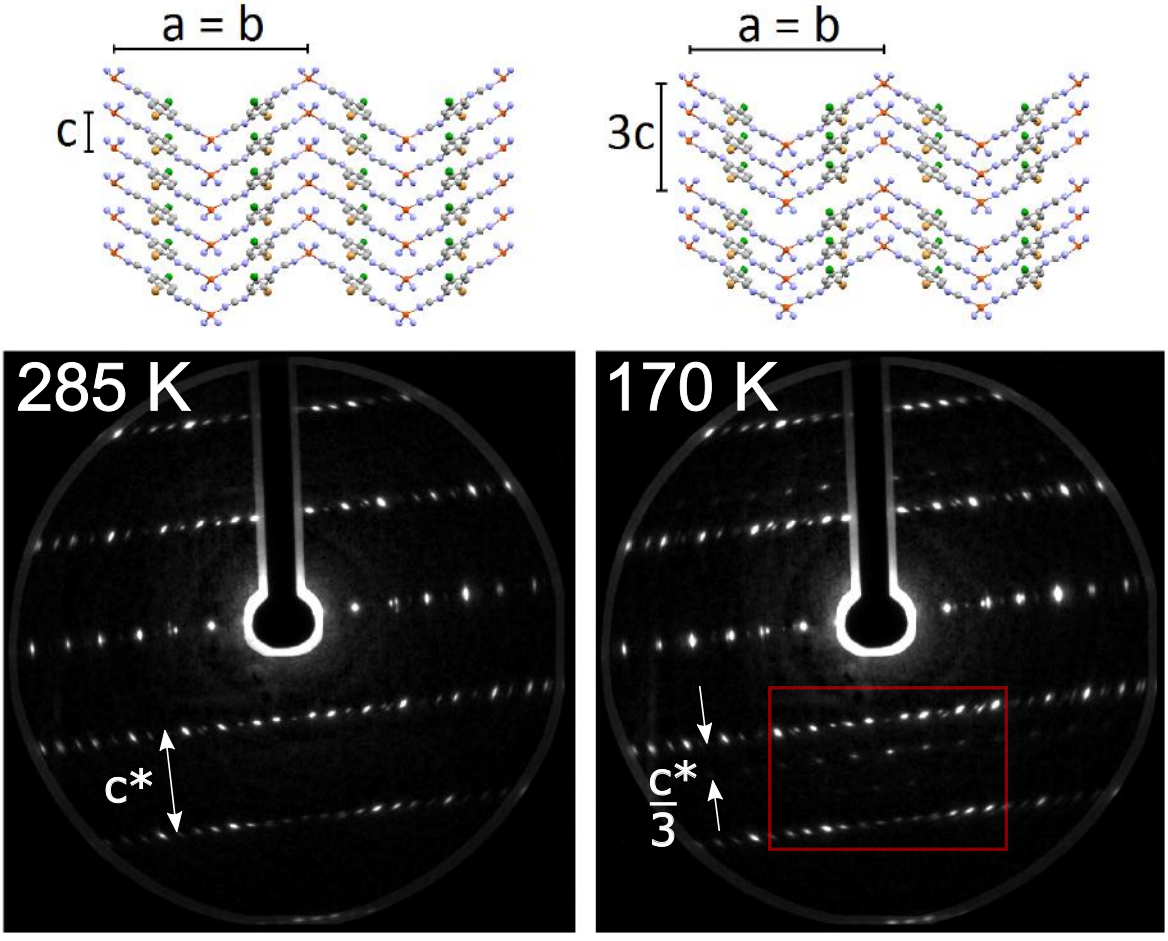

Figure 2.8: Static background-subtracted diffraction patterns of Cu(Me,Br-DCNQI)$_2$ and the corresponding schematics of the crystal structure, before (285 K, left) and after (170 K, right) the metal-insulator phase transition. As a result of the PLD associated with the phase transition, trimer peaks appear at $\frac{1}{3}c^*$ between the Bragg peaks.

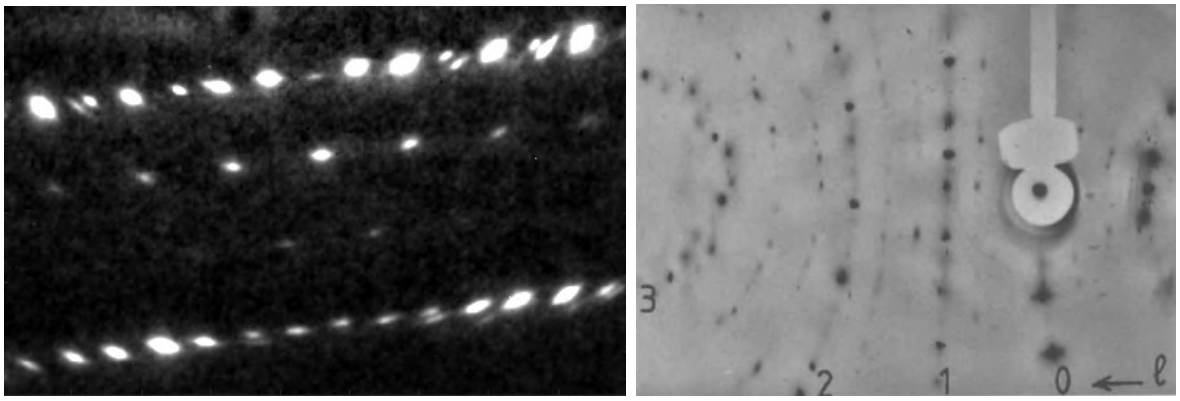

Figure 2.9: Left: Zooming in on the trimer peaks in Figure 2.8. **Right:** X-ray diffraction pattern taken at 20 K of Cu(MeCl-DCNQI)$_2$ with trimer peaks visible at $\frac{1}{3}c^*$ [8]. The trimer peaks appeared at 200 K (the M-I transition was reported to be 210 K [30]) and increased in intensity with lowering temperature.

Photoinducing the I-M phase transition in Cu(DCNQI)$_2$

Furthermore (and crucial for UED experiments), the insulator-to-metal (I-M) phase transition can be photoinduced: a short optical pulse of laser light can 'pump' the crystal from the insulating phase into the conducting phase within 30 ps as demonstrated by Karutz et al. [7]. Conductivity measurements were performed on a bulk sample of Cu(d_6-DCNQI)$_2$, monitoring the transient current response of the sample at different 'operating points' as shown in Figure 2.10 (a) [7]. Note that Cu(d_6-DCNQI)$_2$ is a Group III salt and reenters the metallic phase upon further cooling at approximately 40 K.

Measurements when optically exciting the crystal at operating point 1 (op1), just below the phase transition temperature, show that the sample's conductivity can be restored on fast (< 30 ps) timescales (time resolution limited) and decays on much longer timescales of hundreds of nanoseconds. The rise of the transient current for Cu(d_6-DCNQI)$_2$ is shown in Figure 2.10 (b), and the long decay for the alloy h_8/d_6-Cu(DCNQI)$_2$ is shown in Figure 2.10 (d). Optically pumping a sample of h_8/d_6-Cu(DCNQI)$_2$ at operating point 3 (op3), just above the reentry transition temperature, also results in a fast return of the sample's conductivity and a slow decay over hundreds of nanoseconds (Figure 2.10 (f)). The dashed lines in Figures 2.10 (d) and (f) indicate the conductivity of the sample in the metallic phase, highlighting that the conductivity upon photoexcitation reaches the same value as the conductivity of the crystal in its metallic, high temperature phase. These results indicate that the bulk volume of the crystal undergoes the phase transition, not only the near-surface unit cells that are directly excited by the optical pump (the penetration depth of the pump beam is 100 nm, compared to a sample diameter of 0.2 mm).

Transient current measurements at operating point 2 (op2), approximately 15 Kelvin below the metal-insulator transition, show a different response. As displayed in Figure 2.10 (c), when pumping at op2 the transient current response displays a fast rise (~ 30 ps) and fast decay (~ 50 ps). This result corresponds to conventional photoconductivity: electrons are briefly excited into the conduction band and then relax back into the valence band on fast timescales. Moreover, long-time measurements up to

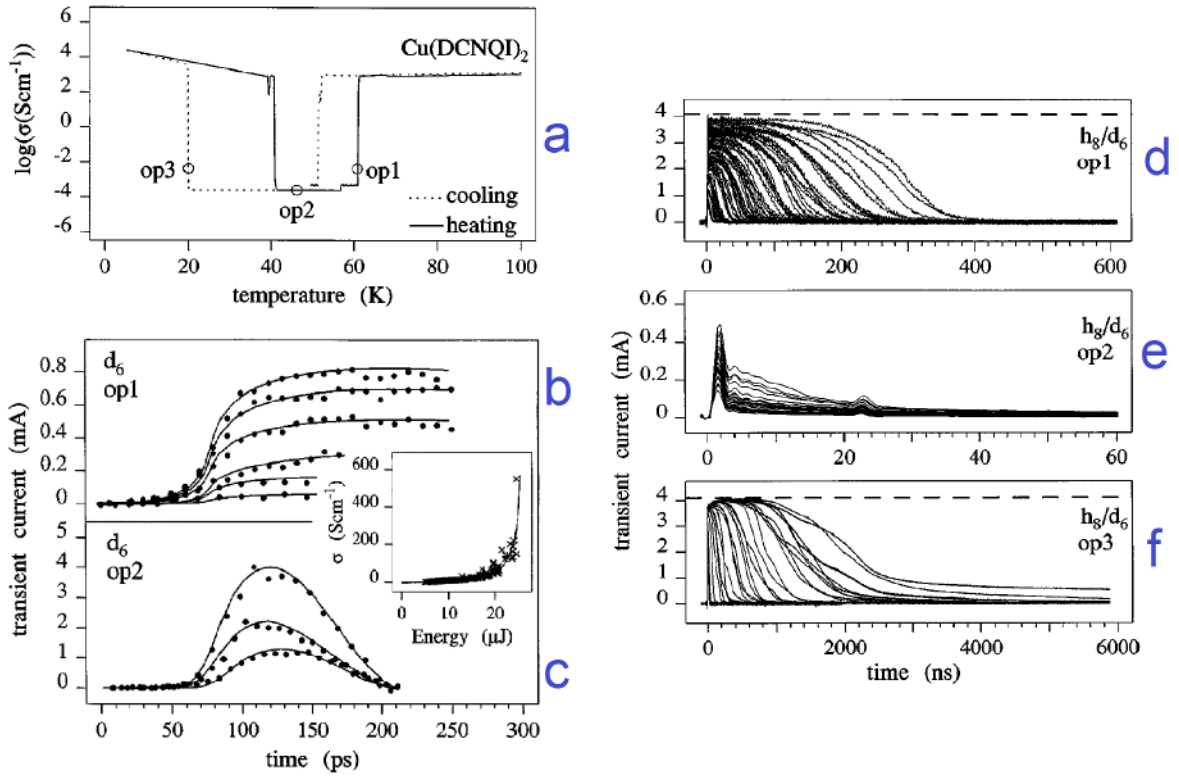

Figure 2.10: **a:** The steady-state conductivity of Cu(d_6-DCNQI)$_2$. **b and c:** transient current response measurements at op1 (b) and op2 (c) of the alloy h_8/d_6-Cu(DCNQI)$_2$. **d–f:** long-time transient current measurements on the alloy h_8/d_6-Cu(DCNQI)$_2$ at the three different operating points (the metallic conductivity is indicated by the dashed line). Figures from [7].

6000 ns at op2 on h_8/d_6-Cu(DCNQI)$_2$ show that the metallic conductivity could not be reached despite higher electric fields (see Figure 2.10 (e)). These results indicate that the bulk of the sample did not undergo the phase transition upon photoexcitation at op2 and the crystal remained insulating. Additionally, note that inducing a successful I-M transition at op3 but not op2 shows that the phase transition is not simply caused by heating due to the optical pump pulse.

The optically induced phase transition and the accompanying ultrafast structural dynamics are what we are able to study with our UED setup. Although UED experiments are unable to directly measure the conductivity of a sample, we instead have access to the structural lattice changes within the sample and will be able to make a complimentary study to the conductivity measurements discussed here.

2.2 Effect of temperature and pressure on the conductivity of Cu(DCNQI)$_2$

After discussing the behaviour and properties of the Cu(DCNQI)$_2$ salts, we will now focus on one of their most appealing features: the highly changeable chemical structure and its effect on the salt's electronic properties. The effect of different chemical compositions is to exert a "chemical" pressure on the sample (as opposed to an "external" or hydrostatic pressure). First the effect of external pressure on Cu(DCNQI)$_2$ salts will be discussed, followed by a quantitative analysis of the effects of different chemical changes and how they are physically similar to applying an external pressure.

The effect of external pressure

Aumüller et al. [5] found the conductivity of the dimethyl copper salt Cu(DMe-DCNQI)$_2$ to be 800 S cm^{-1} at 295 K under ambient pressure, and that the conductivity increases upon cooling up to 5×10^5 S cm^{-1} at 3.5 K (see Figure 2.11). Tomic et al. [31] studied the dependence of the same salt's conductivity on both temperature and pressure, and were able to make several interesting observations:

- Even a relatively small hydrostatic pressure of 100 bar applied to Cu(h_8-DCNQI)$_2$ can induce an abrupt (first order) M-I transition at around 50 K.
- A reentry from the insulating state into the metallic state is possible if the crystal is cooled further under pressures between 100–300 bar.
- A greater applied pressure results in a higher M-I transition temperature, as shown by the phase diagram of Cu(DMe-DCNQI)$_2$ in Figure 2.11.
- The greater the applied pressure, the more the first-order behaviour is suppressed (data not shown). That is, the phase transition becomes spread over many Kelvin rather than an abrupt step within several Kelvin. Similar behaviour was observed in pressure studies on Cu(MeBr-DCNQI)$_2$ by Kobayashi et al. [32].

In the years since Aumüller's first paper, many studies have been done on Cu(DCNQI)$_2$ samples under pressure (e.g., [33; 34; 35]) and it has been concluded that applying pressure to a sample yields similar results to cooling. For example, the structural changes induced by pressure are similar to those induced by lowering the temperature, and the large hysteresis observed in electronic properties upon cooling and heating is also present in pressure measurements.

The source and effect of chemical pressure

It has been shown that by altering the chemical composition of a sample, one can exert a "chemical" pressure on a sample and alter its properties such that the sample behaves as if it was under external or hydrostatic pressure [36; 14]. To understand the origins of this chemical pressure, note that different choices in deuteration, rest groups, etc. (see Figure 2.1) result in different bond lengths, angles and lattice constants of the crystal unit cell. The choices made have a more or less systematic effect on both

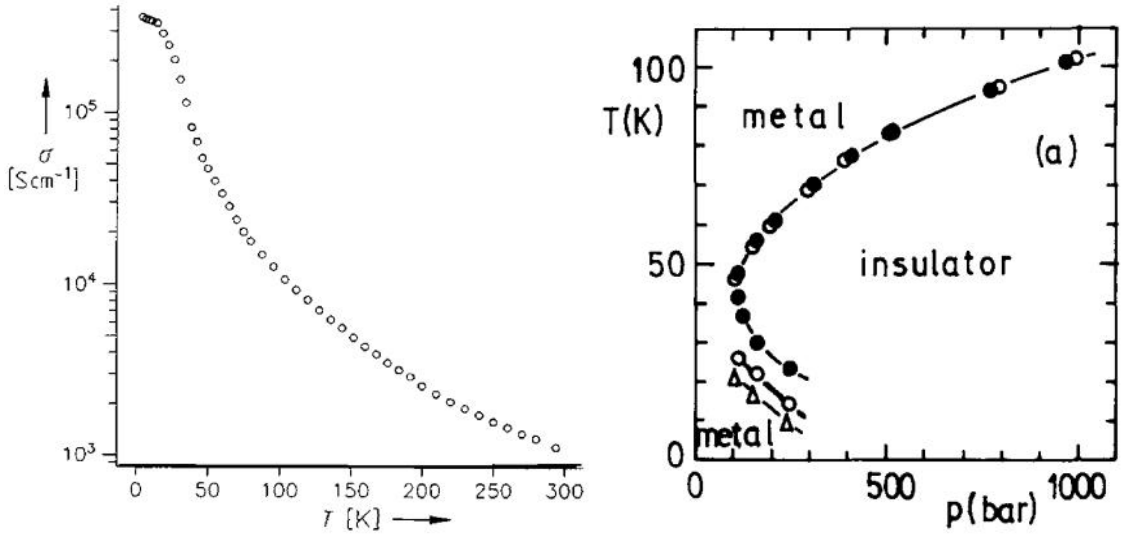

Figure 2.11: The effect of temperature and pressure on the electronic state of Cu(DMe-DCNQI)$_2$. **Left:** Cu(DMe-DCNQI)$_2$ remains conducting to low temperatures, reaching extremely high conductivities upon cooling [5]. **Right:** A M-I transition can be induced in the crystal even under low pressures of 100 bar and a reentry into the metallic state is possible upon further cooling under pressures between 100–300 bar [31].

the lattice parameters and the phase transition temperature (or the pressure required to induce a phase transition). Here I will discuss deuteration and rest groups in detail.

The effect of deuteration

An intuitive example is that of deuteration: a C-D (carbon-deuterium) bond is shorter than a C-H (carbon-hydrogen), therefore the effect of replacing a hydrogen atom with a deuterium atom is a slight contraction of inter-molecular distances in the unit cell of the sample, leading to a smaller unit cell volume—the same effect as applying external pressure to a sample. Thus the more deuterated a sample is, the higher the chemical pressure and the less stable the metallic state, resulting in a higher phase transition temperature.

A numerical value for the effective chemical pressure applied on the sample by deuteration can be found by comparing the external pressure required to induce a phase transition in crystals with and without deuteration. From experimental results, Kato et al. [14] were able to estimate a phenomenological linear dependence of the effective pressure P_{eff} (bar) of deuteration:

$$P_{\text{eff}} = 80(a_1 + a_2 + 0.2b), \tag{2.1}$$

where a_1 and a_2 are the number of deuterons on the two DCNQI methyl groups ($0 \leq a_1 + a_2 \leq 6$), and b is the number of deuterons in the carbon ring ($0 \leq b \leq 2$), as shown in Figure 2.12 (left). For example, (2.1) tells us that deuterating a methyl hydrogen applies a higher chemical pressure to the sample than deuterating a ring hydrogen. Importantly, the close linear dependence of the transition temperature on deuteration is direct evidence that the phase transition properties of such crystals can be predictably tuned as desired.

Furthermore, Hünig et al. [6] conducted experiments on four Cu(DMe-DCNQI)$_2$ salts with varying extents of deuteration: a) [0,0;0], b) [0,3;0], c) [3,3;0] and d) [3,3;2], where the pattern of deuteration is denoted by [a_1, a_2; b]. The temperature dependence of the conductivities of the different deuterated salts is shown in Figure 2.12 (right). The most striking observation is that even deuterating a single methyl group of Cu(DMe-DCNQI)$_2$ induces an abrupt M-I transition at 58 K. Further deuteration shifts the phase transition to higher temperatures.

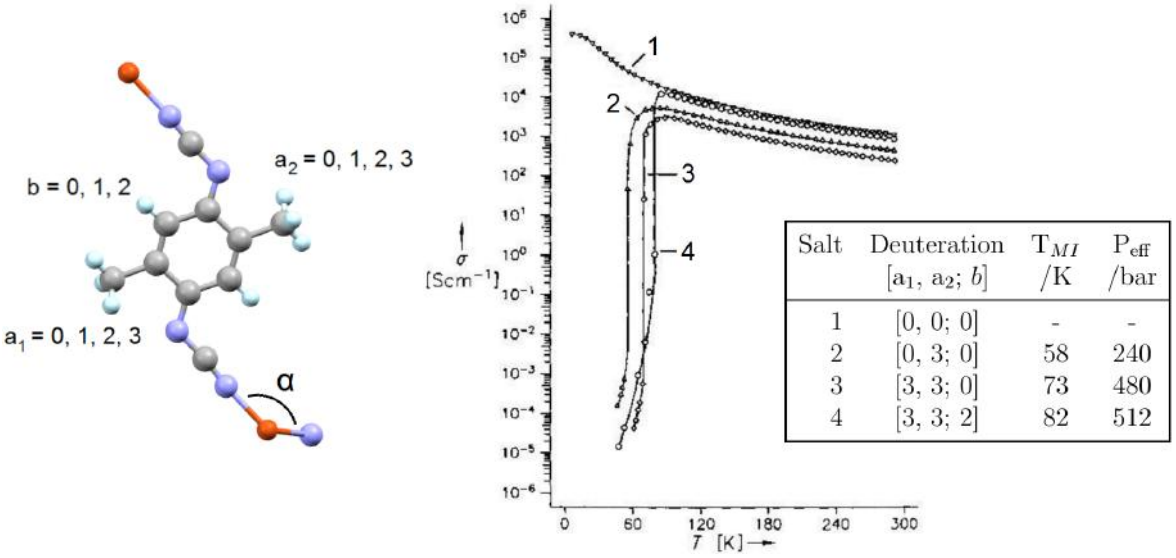

Salt	Deuteration [a_1, a_2; b]	T_{MI} /K	P_{eff} /bar
1	[0, 0; 0]	-	-
2	[0, 3; 0]	58	240
3	[3, 3; 0]	73	480
4	[3, 3; 2]	82	512

Figure 2.12: Left: The hydrogens on the DCNQI molecule can each be replaced with a deuterium atom and labelled by a_1 and a_2 (the number of deuterons on each methyl group) and b (the number of deuterons on the carbon ring). **Right:** The effect of deuteration on the conductivity of Cu(DMe-DCNQI)$_2$ (adapted from [6]), where T_{MI} is the temperature at which the metal-to-insulator transition occurs, and P_{eff} is calculated using (2.1).

The effect of different R groups

The effect of different R groups on a salt's behaviour can also be understood and is less precise than that of deuteration (i.e., a trend rather than a rigid relationship). As mentioned above, the DCNQI columns in the crystal structure are interconnected through tetrahedrally coordinated Cu ions. The N–Cu–N angle α (see Figure 2.12, left) is a measure of the degree of distortion of the tetrahedron from the T_d symmetry (i.e., distortion of α away from $= 109.5°$). Typically $\alpha \approx 122$–$127°$ for Cu(DCNQI)$_2$ crystals. The variance in α is attributed to the bulkiness of the different possible rest groups. As shown in Table 2.1 [19], bulkier rest groups lead to smaller α values, therefore a lower chemical pressure and ultimately a lower phase transition temperature. Recall that α is linked to the extent of π-d mixing between DCNQI and Cu d electrons as discussed previously, and in this way the choice of rest group can affect the electronic properties of the salt.

For easier visualisation, the relationship between α and phase transition temperature in five Group II salts is plotted in Figure 2.13 (left). A larger α results in a higher phase transition temperature. The dashed lines are to guide the eye. Also shown in Figure 2.13 (right) is the unit cell volume against phase transition temperature for the

R_1,R_2-DCNQI	a /Å	c /Å	V /Å^3	α /deg	T_{M-I} /K
MeBr-DCNQI	21.601	3.856	1799.2	125.3	155
DBr-DCNQI	21.558	3.896	1810.7	125.3	160
MeCl-DCNQI	21.559	3.823	1776.9	126.2	210
BrCl-DCNQI	21.569	3.845	1788.8	126.1	213
DCl-DCNQI	21.55	3.816	1772.2	127.1	230

Table 2.1: The effect of different rest groups R_1 and R_2 on the structural parameters and metal-insulator transition temperature T_{M-I} for several different Cu(R_1,R_2-DCNQI)$_2$ salts. Given in the table are the a and c lattice constants, the unit cell volume V, the N–Cu–N angle α, and the metal-to-insulator transition temperature T_{M-I}. Particularly note that bulkier rest groups tend to result in smaller values for α (i.e., a smaller distortion of the tetrahedral geometry around the Cu ions), resulting in a lower effective pressure and a lower phase transition temperature. Data from [19].

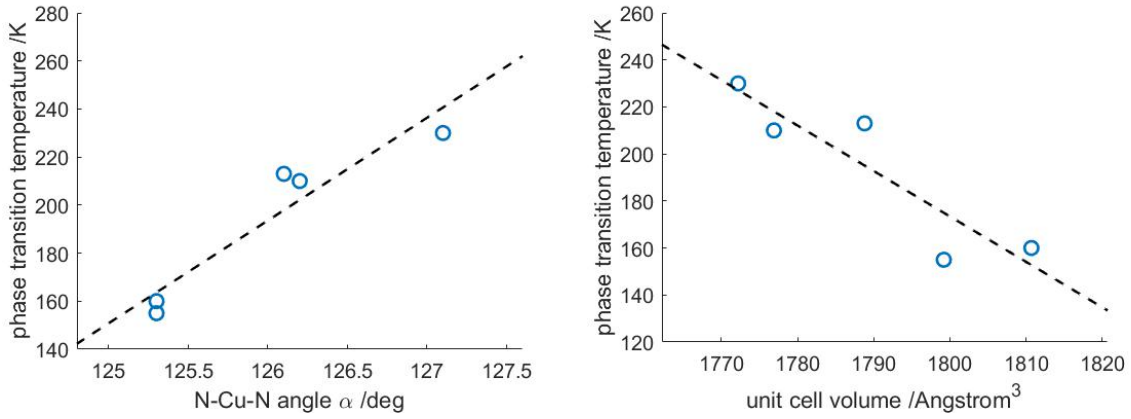

Figure 2.13: The N–Cu–N angle α and the unit cell volume of five different Cu(DCNQI)$_2$ salts, plotted against their phase transition temperatures. The dashed lines are to guide the eye. Data from [19].

same salts. A smaller unit cell (i.e., a higher effective pressure) corresponds to higher phase transition temperatures.

Many studies have been done on the range of phase transition temperatures that can be achieved by varying the R groups of Cu(DCNQI)$_2$. For example, the pressure required to induce a phase transition in Group I salts can range from 0.1–8 kbar, a huge range in pressure (e.g., [19]). Similarly, the data presented in Table 2.1 shows that the phase transition temperature of Group II salts can range from at least 155–230 K depending on R groups. As mentioned earlier, deuteration or alloys of different salts can offer further control over the transition temperature, such that the idea of tailoring a particular crystal to meet specific requirements is not far-fetched.

The significance of the N–Cu–N angle, α

As Table 2.1 shows, different constituents can have a significant effect on α. However, even for each particular salt, α has a strong dependence on temperature and pressure. For example, shown in Figure 2.14 (left) is the magnitude of α upon cooling in three

crystals of Cu(DMe-DCNQI)$_2$ with different levels of deuteration, from Groups I, II and III (note the log scale for temperature) [19]. In the Group II and III crystals, α experiences an abrupt increase of several degrees around the M-I transition temperature. Furthermore, after the Group III crystal has undergone the reentry (i.e., the M-I-M transition), α drops to the same value as the Group I crystal, which remains conducting to low temperatures and experiences only gradual changes in α. From these results it is clear there is a close relationship between α and the electronic state of the crystal, which we have previously linked to the π-d orbital overlap.

Experiments by Nishio et al. [16] also observed a strong hysteresis of α along with susceptibility during heating and cooling cycles, further evidence of the relationship between α and the electronic state. Kato et al. [11] observed quantitatively similar behaviour of α in the particular sample that we study, Cu(Me,Br-DCNQI)$_2$, as shown in Figure 2.14 (right).

With the relationship between α and the electronic state in mind, it is logical to think that α may play a role in the ultrafast structural changes of the crystal as it is photoswitched from insulating to metallic. This is a structural change we may be able to resolve in our UED experiments.

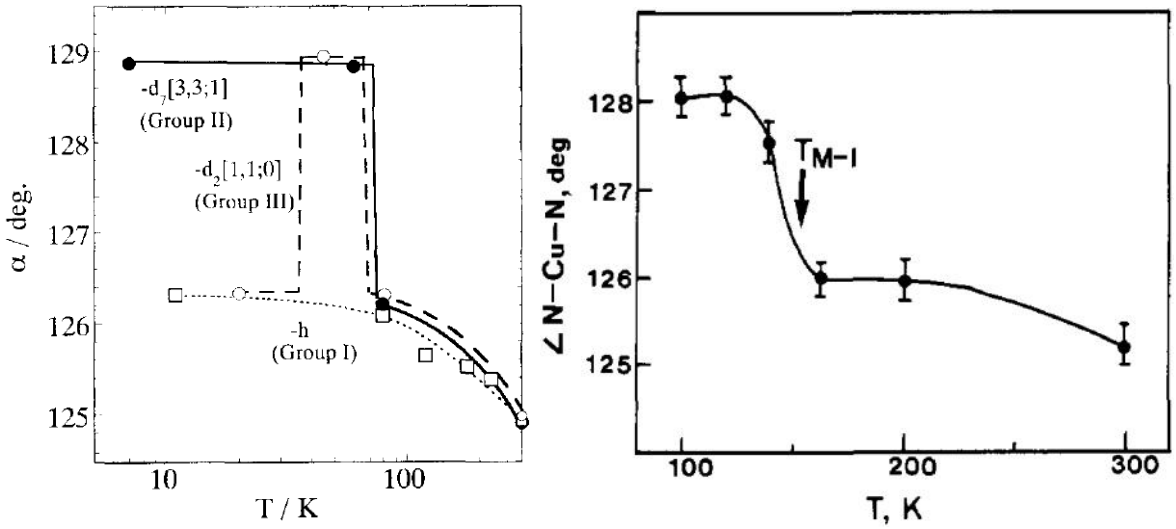

Figure 2.14: The temperature dependence of the N–Cu–N angle α for different salts. **Left:** Data from three Cu(DMe-DCNQI)$_2$ salts with different extents of deuteration [19]. **Right:** Data from Cu(MeBr-DCNQI)$_2$ [11], the same salt that we study. An increase (decrease) in α is observed near the transition temperature in the salts that undergo a M-I (I-M) transition.

To summarise, particular Cu(DCNQI)$_2$ salts are able to undergo a metal-insulator transition upon cooling and the insulator-metal transition can be photoinduced on fast timescales. The particular salt that we study is Cu(Me,Br-DCNQI)$_2$ with a metal-insulator transition temperature of 155 K. Both steady-state and time-resolved results from experiments on Cu(Me,Br-DCNQI)$_2$ will be presented in Chapter 5, with some preliminary discussion about the real-space interpretation of the data.

3. Diffraction theory and crystal structure

3.1 Diffraction patterns and Fourier transforms

Diffraction is the spreading out of a coherent wave upon encountering an obstacle or aperture. The subsequent constructive and destructive interference between different parts of the wave result in an interference pattern. The following discussion will use some simple examples to explain the nature of diffraction patterns and their relationship with Fourier transforms and reciprocal space. Although this project is on electron diffraction, much of the theory applies equally to any object with wave-like properties, from light to molecules [37] to sound waves.

Fraunhofer diffraction from a grating

Consider a plane wave of wavelength λ impinging on a general obstacle or aperture. The transmission function $u(x)$ (also known as the amplitude function) describes the amplitude of the wave that leaves the aperture. It can be shown that the far-field amplitude of the wave after passing the obstacle is the Fourier transform of the transmission function [38].

As the objects we wish to study using electron diffraction are crystals (i.e., three-dimensional gratings), let us first consider a one-dimensional grating consisting of N slits of width a spaced a distance d apart, as shown in Figure 3.1. By taking the Fourier transform of the transmission function, the far-field interference pattern intensity $I(\beta) = |U(\beta)|^2$ from N finite slits can be calculated:

$$I(\beta) \propto \left(\frac{\sin(\beta a)}{\beta a}\right)^2 \left(\frac{\sin(N\beta d/2)}{\sin(\beta d/2)}\right)^2, \tag{3.1}$$

where $\beta = k\sin(\theta)$ and k is the scattered vector, as shown in Figure 3.1. An example of the N-slit interference pattern is shown in Figure 3.1 for $N = 6$ and $d = 10a$. Here we have a result which can be related to diffraction from a crystal, i.e., a periodic arrangement of atoms or molecules of a finite size that act as a regular three-dimensional grating. For a crystal, the equivalent N will be large so the principle maxima will dominate. Note that the effective number of slits N for diffraction from a crystal will not simply be the literal number of "slits" (unit cells) impinged upon by the plane wave which is typically a huge number, but the number of unit cells over which the plane wave is spatially coherent (see Section 4.1 for more details).

Even for relatively simple real-life crystals, calculating the far-field interference patterns become complex and computationally expensive [39]. The arrangement of atoms within a crystal can be described by the *structure factor* of the unit cell (see Section 3.3) and is clearly far more complex than a slit in a grating. Consequently, the structure factor has

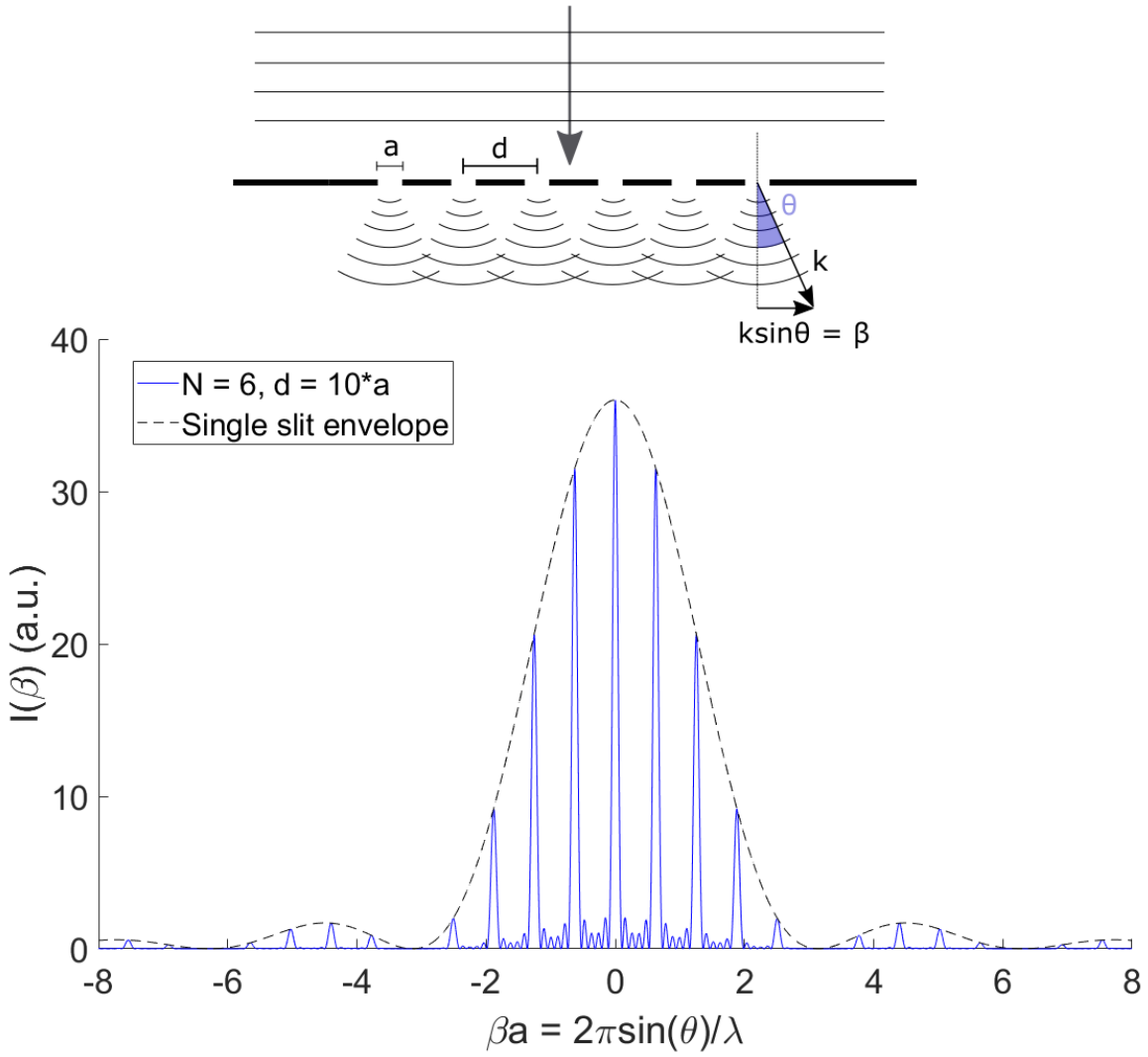

Figure 3.1: The interference pattern for a 6 slit grating, with separation d and width $a = 10d$.

a large effect on the far-field interference pattern and results in additional destructive interference, further modulating the amplitude of diffraction peaks. The thickness of real-life crystals also plays an important role, and both multiple scattering and the phase difference between waves scattered at different sample depths must be taken into account.

Even so, regardless of the increased complexity of the real world, the underlying principles of diffraction remain the same and many aspects of diffraction pattern analysis can be linked back to relatively simple arguments based on interference.

Bragg diffraction

A rigorous treatment of electron diffraction treats the incoming electrons as a plane wave and each atom in the three-dimensional crystal structure as an obstacle that scatters electrons as spherical waves. The interference between all the spherical waves is summed to find the resulting diffraction pattern, directly analogous to diffraction from an N-slit grating described above.

An equivalent and perhaps more intuitive approach exists: one can consider the crystal lattice in terms of planes of atoms, where each plane acts as a mirror that reflects the electrons. Referring to Figure 3.2, one can obtain an equation for the path difference between electrons reflecting from different planes in terms of the distance between the planes (typically denoted d) and the angle of incidence θ. From straightforward geometry the path difference is $2d\sin(\theta)$. Equating this result with the condition for constructive interference gives us Bragg's Law:

$$2d\sin(\theta) = n\lambda, \text{ where } n = 0, 1, 2, ..., \tag{3.2}$$

where d is the distance between crystal lattice planes, 2θ is the total angle of deflection of the diffracted wave (see Figure 3.2), and λ is the de Broglie wavelength of the electrons. The de Broglie wavelength is given by $\lambda = h/m_e v$, where h is Planck's constant, m_e is the electron mass and the velocity v can be found from the kinetic energy of the electrons, $E_k = \frac{1}{2}m_e v^2 = 30$ keV for non-relativistic electrons.

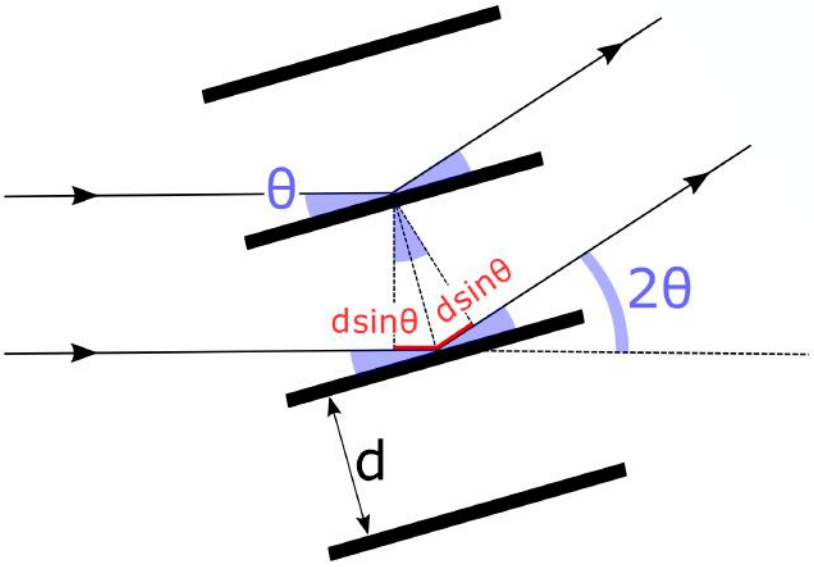

Figure 3.2: Diffraction of electrons in a crystal can be thought of as specular reflection from parallel lattice planes in the crystal. The path length difference, $2d\sin(\theta)$, between the two different reflections must be equal to an integer number of wavelengths, $n\lambda$, for constructive interference to occur.

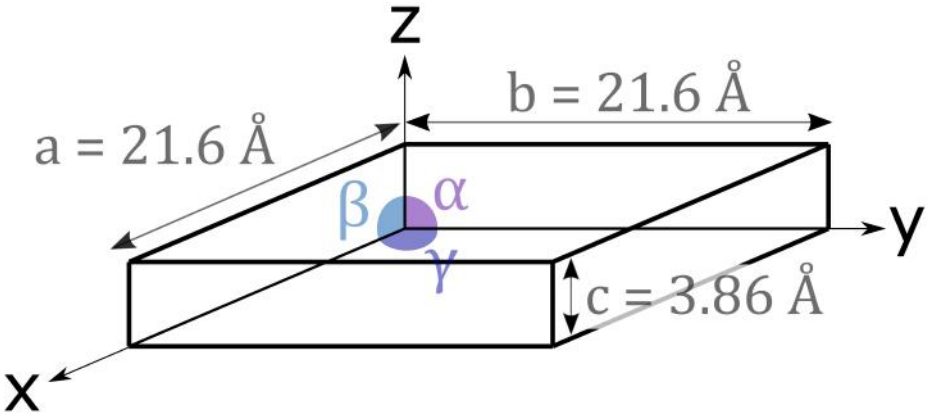

Figure 3.3: The unit cell dimensions of Cu(Me,Br-DCNQI)$_2$. The side lengths are $a = b =$ 21.6 Å and $c = 3.86$ Å, and the angles are $\alpha = \beta = \gamma = 90°$. The position of atoms within the unit cell is shown in Figure 2.1.

3.2 Basic crystal structure in three dimensions

Crystals are periodic and the unit that is repeated to form the overall periodic structure is known as the unit cell. The unit cell of a three-dimensional lattice is described by six parameters: the three side lengths a, b and c, and the three angles α, β and γ (see Figure 3.3). The simplest three-dimensional lattice is the simple cubic lattice ($a = b = c$ and $\alpha = \beta = \gamma = 90°$), and the crystal that we study, Cu(DCNQI)$_2$ (introduced in Chapter 2), has a tetragonal lattice ($a = b \neq c$, and $\alpha = \beta = \gamma = 90°$).

The direct lattice and reciprocal lattice

In a direct (real space) lattice, each lattice point $\mathbf{R}$ can be described by an integer sum of the primitive lattice vectors, starting from an arbitrary lattice point denoted by $[0, 0, 0]$. $\mathbf{R}$ is given by

$$\mathbf{R} = u\mathbf{a_1} + v\mathbf{a_2} + w\mathbf{a_3}, \tag{3.3}$$

where $\mathbf{a_i}$ are the primitive lattice vectors, and u, v and w are integers. A specific vector in the direct lattice (i.e., a vector going from one lattice point to another) can be denoted by $[uvw]$.

Using the definition of a lattice point $\mathbf{R}$ on the direct lattice given by (3.3), the reciprocal lattice $\mathbf{G}$ can be defined as [40]:

$$\mathbf{G} = h\mathbf{b_1} + k\mathbf{b_2} + l\mathbf{b_3}, \tag{3.4}$$

where h, k and l are integers (known as the Miller indices), and $\mathbf{b_i}$ are lattice vectors of the reciprocal lattice which have the property $\mathbf{a_i} \cdot \mathbf{b_j} = 2\pi\delta_{ij}$. For example, consider the simple cubic lattice with side length a. The direct lattice vectors $\mathbf{a_i}$ are $a\hat{\mathbf{x}}, a\hat{\mathbf{y}}$ and $a\hat{\mathbf{z}}$, and the corresponding reciprocal lattice vectors $\mathbf{b_i}$ are $\frac{2\pi}{a}\hat{\mathbf{x}}$, $\frac{2\pi}{a}\hat{\mathbf{y}}$ and $\frac{2\pi}{a}\hat{\mathbf{z}}$.

Similarly to (3.3), the notation (hkl) can be used to describe a specific vector in reciprocal space. Conventionally a bar is used to indicate negative Miller indices. E.g., $(\bar{1}11)$ would be used to denote (-111).

Lattice planes

A plane can be defined by a vector normal to the plane. In this way, every reciprocal lattice vector $\mathbf{G}$ can be used to describe a so-called 'family' of lattice planes normal to $\mathbf{G}$. The magnitude of the reciprocal lattice vector $|\mathbf{G}|$ is related to the distance d between the planes by $d = 2\pi/|\mathbf{G}|$ [40]. In the context of electron diffraction, this means that for each reciprocal lattice vector (that is, a peak in the diffraction pattern) there is a corresponding family of lattice planes.

As any reciprocal lattice vector can be described by its Miller indices given by (3.4), we can also use Miller indices to denote the corresponding family of planes. It can be seen that the family described by the Miller indices (100) (for example) is equivalent to the family described by the indices $(\bar{1}00)$. The notation {100} can be used to denote all equivalent families of planes. When it comes to analysing diffraction patterns, all peaks belonging to each {hkl} set can be treated the same—the same physical planes result in each of the different peaks, thus the response of the peaks should be the same.

3.3 Scattering directions and amplitudes

Scattering directions and the Ewald sphere

Not all possible lattice planes in a crystal result in constructive interference (i.e., a peak in the diffraction pattern). A construction called the Ewald sphere can be used to visualise which planes result in a diffraction peak for incoming electrons of wavelength λ and is shown in Figure 3.4 in two dimensions.

As described in Section 3.1 and as shown in Figure 3.2, an incoming electron beam elastically scatters off a crystal plane with a total deflection angle 2θ. It is useful to describe the electrons in terms of their incident and transmitted wave vectors, $\mathbf{k}$ and $\mathbf{k}'$ respectively. The Ewald sphere has its origin at the tip of $\mathbf{k}$ and a radius of $|\mathbf{k}| = |\mathbf{k}'| = 2\pi/\lambda$. By geometry and under the condition of Bragg's law, it can be shown that the magnitude of the scattering vector $|\Delta\mathbf{k}| = |\mathbf{k}' - \mathbf{k}| = 2\pi/d$, i.e., the magnitude of a reciprocal lattice vector $\mathbf{G}$. The base of this scattering vector defines the origin of reciprocal space. The reciprocal lattice can now be superimposed on top of the Ewald sphere (a cubic lattice has been chosen for simplicity).

It can be shown that the Bragg condition is satisfied for every reciprocal lattice point that sits on the surface of the Ewald sphere (e.g., [40]). In other words, the only peaks that appear in the diffraction pattern are those that correspond to reciprocal lattice points on the surface of the Ewald sphere. This explains why only a few diffraction peaks are visible for each orientation of the sample in x-ray crystallography; the Ewald sphere overlaps with few reciprocal lattice points. If the full crystal structure is to be determined, the sample must be rotated with respect to the beam and a diffraction pattern acquired at each sample orientation, compiling a three-dimensional pattern with as many diffraction peaks as possible.

In our UED experiments we do not rotate the sample but acquire diffraction images at a single sample orientation, thus our electron diffraction patterns are a two-dimensional slice of the reciprocal lattice. However, electrons interact more strongly with matter

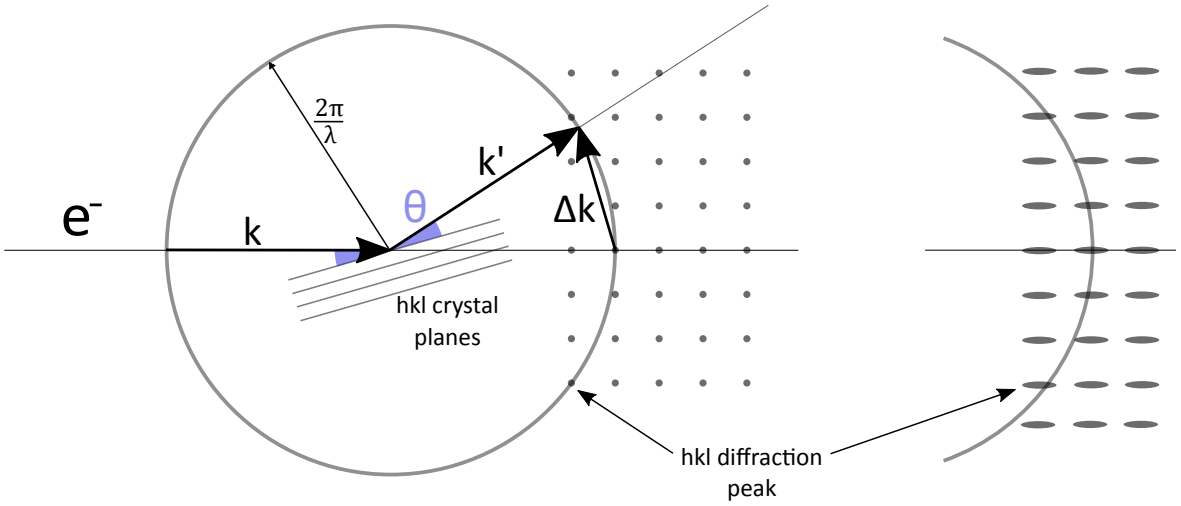

Figure 3.4: Left: The Ewald sphere construction, demonstrating the relation between a particular set of parallel {hkl} lattice planes and diffraction peaks. Only {hkl} peaks that overlap with the surface of the Ewald sphere satisfy Bragg's Law and appear in the diffraction pattern. **Right:** A thin crystal sample (i.e., like those used in transmission electron diffraction) results in elongation of reciprocal lattice points (a relaxation of the interference conditions) and more peaks appear in the diffraction pattern.

than x-rays and our samples must be very thin (< 100 nm) in order to transmit the electrons. One effect of a sample being thin along the axis of electron propagation is to elongate the reciprocal lattice points along the same direction (i.e., the conditions for interference are relaxed) as shown in Figure 3.4 (right). Due to this elongation, many more reciprocal lattice points overlap with the surface of the Ewald sphere (that is, more reflections satisfy the Bragg condition) and appear in the diffraction pattern. The de Broglie wavelength for electrons used in diffraction experiments is also typically shorter than that for x-rays, leading to a larger Ewald sphere radius in electron diffraction experiments and therefore more overlapping reciprocal lattice points.

It should be emphasised that electron diffraction is rarely used to help determine the overall structure of the crystal and that this is usually done by x-ray crystallography. In contrast, a pulsed electron beam in diffraction mode can be used to study ultrafast *changes* in a crystal structure after (for example) photoexcitation, due to their greater interaction strength and stronger diffraction signals. Combining knowledge of the static structure determined by x-ray crystallography and the ultrafast changes observed by electron diffraction, we can work towards the real-space structural changes within the crystal—the two techniques are complimentary. In the case of studying $Cu(DCNQI)_2$ salts with UED, the structure determination by x-ray crystallography is a vital starting point for interpretation of the electron diffraction data.

Scattering amplitudes

The Ewald sphere construction can tell us which peaks can appear in a diffraction pattern but not about their amplitudes. The *intensity* of a diffraction peak depends on the structure of the unit cell of the crystal, which elements are present and how the atoms are arranged. Specifically, the structure factor $F(\mathbf{G})$ is the amplitude for scattering to occur in a particular direction $\mathbf{G} = \mathbf{k}' - \mathbf{k}$. For electrons, $F(\mathbf{G})$ is the

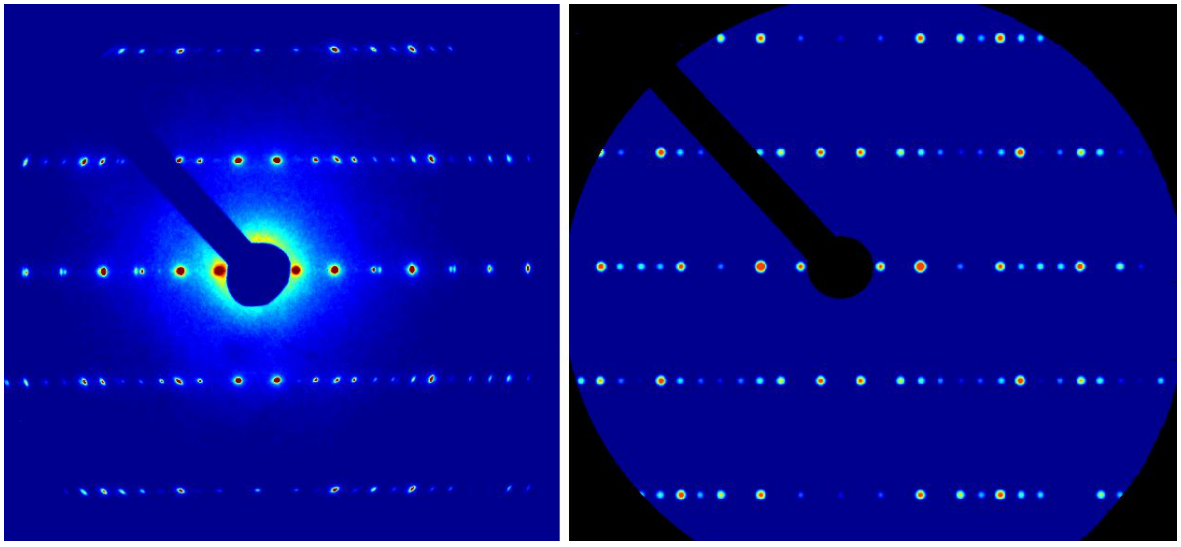

Figure 3.5: Comparison of experimental and simulated diffraction patterns. **Left:** Experimental steady-state electron diffraction pattern of Cu(Me,Br-DCNQI)$_2$ taken using our setup. **Right:** Simulated diffraction pattern from a single crystal of Cu(Me,Br-DCNQI)$_2$ using Crystalmaker [41].

three-dimensional Fourier transform of the electron density of the crystal unit cell. This is directly analogous to Fraunhofer diffraction, but instead of taking the Fourier transform of the aperture transmission function we are taking the Fourier transform of the electron density.

For electron diffraction simulations, the electron density must therefore be known. However, this quantity is difficult to obtain (experimentally or by calculation). Some approximations are commonly used when one wishes to calculate an estimation of the scattering intensity distribution from a particular crystal (i.e., simulate the diffraction pattern that a known crystal structure would generate). The simplest approximation is that the atoms in the crystal structure behave as isolated atoms (e.g., chemical bonds are ignored), and that the total *atomic* potential can be approximated as a superposition of the individual atomic potentials [39].

The software we use for simulating diffraction patterns from crystal structures is CrystalMaker [41], which requires as input the crystal structure, obtained by x-ray crystallography by the Barbour Group, Stellenbosch University. Although approximations are involved in the calculations, good agreement of the Bragg peak intensity distribution can be found between the simulated diffraction patterns from CrystalMaker and our experimental diffraction patterns, as shown in Figure 3.5.

To summarise, the reciprocal lattice vectors determine where constructive interference can occur in the diffraction pattern. The Ewald sphere can be used to see which of the reciprocal lattice points will appear in a single diffraction pattern at a particular electron wavelength and sample orientation. The structure factor determines the amplitude and phase of each diffraction peak.

4. Experimental setup and procedure

4.1 Achieving high temporal and spatial resolution

The aim of ultrafast electron diffraction (UED) is to obtain "molecular movies" that map out the motions of atoms on the relevant time scales in real space. To accomplish this task we need to obtain high temporal resolution in order to follow dynamics that occur on hundreds of femtoseconds to picoseconds (e.g., electron-phonon and phonon-phonon coupling), and high spatial resolution to probe structural lattice changes on the order of picometers (e.g., the amplitude of the periodic lattice distortion).

Temporal resolution and the pump-probe technique

The optical pump-probe technique can be used to study dynamics faster than the detector's response time. In our case, the detector is a "slow" camera but sub-picosecond temporal resolution can be obtained using the pump-probe technique. The trick is that for most of the detector's acquiring time it is not acquiring any data, and only for a very short time window does the camera "see" anything. An excellent analogy is a stroboscope: if placed in an entirely dark room, a brief flash of light (much shorter than the temporal resolution of the human eye [42]) will still reveal the surroundings to a human bystander as a *snapshot* in time, with a much shorter temporal resolution than would be possible with constant illumination (e.g., a lamp).

The same principle is applied in UED experiments. A sub-ps pulsed electron beam (the "probe") is sent through a crystal sample and the diffracted electrons hit the detector. Only in that sub-ps time window will the detector "see" anything, and for the rest of the time when the electron beam is off, the camera will effectively be in a dark room seeing nothing. However, we wish to observe ultrafast *dynamics*, therefore before the electrons probe the sample, an optical laser pulse "pumps" the sample and excites some dynamics (in our case, a structural metal-insulator phase transition). The electrons then arrive at some time delay Δt after the laser pump pulse, taking a sub-ps snapshot of the crystal structure. The time delay is then varied and a series of snapshots at different time delays is built up, compiling a "molecular movie". The sample must be 'reset' or allowed to recover in between snapshots. The achievable temporal resolution in our UED setup is approximately 1.2 ps, as will be discussed in depth later in this section, but sub-100 fs pulses have been achieved in other UED experiments (e.g., [43]).

For a sample to be suitable for pump-probe experiments, it must have certain properties. The sample must survive being pumped multiple times, the dynamics must evolve identically each time, and the sample must recover to its initial state before the next snapshot is taken (i.e., the photoinduced changes must be reversible). Single-shot UED experiments can be performed on samples which are irreversibly changed or damaged after a few pump shots, but these require much brighter electron sources for sufficient

signal to noise ratios and also samples that are easy to acquire so many can be produced. The sample we study, $Cu(DCNQI)_2$, was introduced in depth in Chapter 2 and is an excellent candidate for pump-probe experiments.

Spatial resolution

High spatial resolution is achieved by accelerating the probe electrons to a sufficiently high energy. An electron needs a de Broglie wavelength less than $2d$ (where d is the length scale of interest) so that we are not diffraction limited. The electrons used in our experiments are non-relativistic and have an energy of 30 keV, corresponding to a wavelength of 0.07 Å, which is sufficiently less than the length-scales of the crystal structure we are interested in (our crystal lattice constants are $a = b = 21.6$ Å and $c = 3.86$ Å).

However, structural changes within the unit cell will be much smaller than the crystal lattice constants. Our UED setup can be sensitive to such small changes because the changes occur throughout the periodic crystal sample. For example, the periodicity of the PLD is $3c$, therefore we require a transverse coherence length *greater* than $3c$ to observe it. The transverse coherence length is the range over which two different spatial parts of the beam are still able to constructively interfere (in reality no wave is exactly a plane wave and different spatial parts of the beam will have slightly different phases). In fact, we require the electron probe to be coherent over multiple unit cells, i.e., greater than $a = b = 21.6$ Å. A lower bound for the transverse coherence length of the setup can be determined from a diffraction pattern if the relevant crystal lattice parameters are known. Consider the N-slit diffraction pattern (see Section 3.1). It can be shown that

$$N = x/\Delta x, \tag{4.1}$$

where N is the number of slits of the diffraction grating (i.e., the number of unit cells over which the electron beam is coherent), x is the distance between two (main) maxima, and Δx is the FWHM of one of the maxima, as shown in Figure 4.1. The transverse coherence length can then be calculated by multiplying N by the distance between the "slits" (either c or a, depending on which integrated lineout is taken). For the experimental data shown in Figure 4.1 the lower bound for the transverse coherence

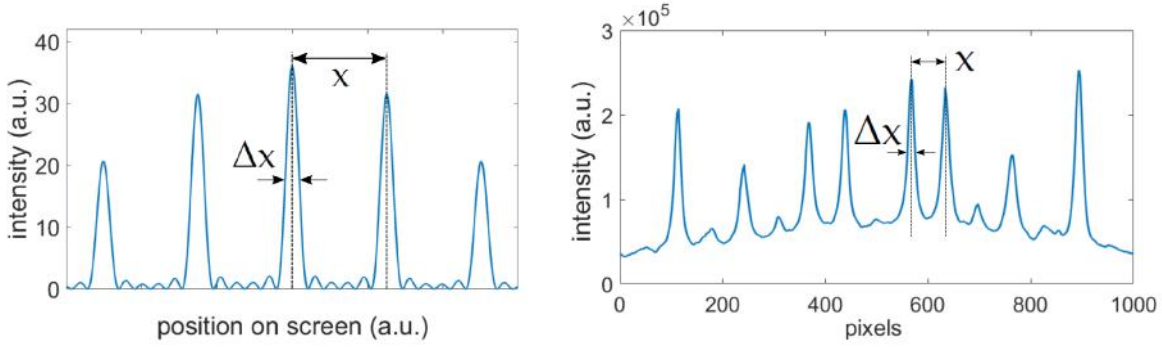

Figure 4.1: Left: The theoretically calculated N-slit interference pattern (see Section 3.1), with the FWHM Δx and the distance between main maxima x labelled. **Right:** The integrated lineout from a typical diffraction pattern acquired by the setup. The ratio of Δx and x can be used to calculate the transverse coherence length of the electron beam.

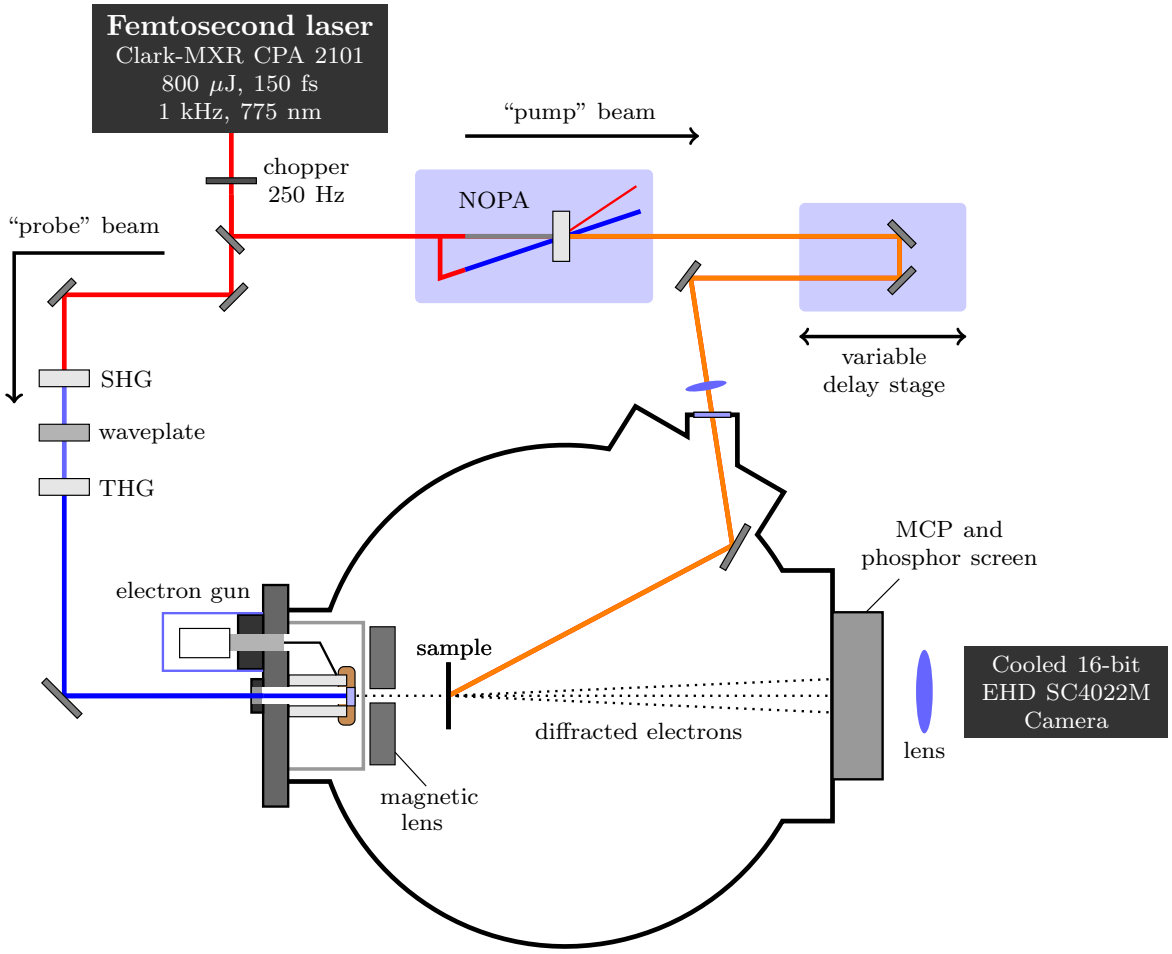

Figure 4.2: The UED experimental setup. The pump beam and the probe beam are overlapped in space and time at the sample position in the chamber.

length is 103 Å, which is sufficiently larger than the largest crystal lattice parameter, $a = b = 21.6$ Å. This method gives a lower bound for the coherence length as peaks may be additionally broadened by other factors, e.g., the beam spot size.

4.2 The pump and the probe

We use an amplified Ti Sapphire laser (Clark-MXR CPA2101) to produce the femtosecond pulsed laser beam. The laser system operates at a repetition rate of 1 kHz and ultimately produces laser pulses with a central wavelength of 775 nm and duration of 150 fs.

A chopper is placed in the beam path to reduce the repetition rate of the laser during experiments, as it was observed that the $Cu(DCNQI)_2$ samples did not fully recover between pump pulses at a repetition rate of 1 kHz. A suitable repetition rate was found to be 250 Hz (i.e., one pulse every 4 ms). After the chopper, the laser beam is split into two paths: the pump path and the probe path, as shown in Figure 4.2. The generation and properties of the pump and the probe beams will be described in the following sections.

The pump

The pump beam is used to optically excite the sample and thus needs a suitable intensity and wavelength. The pump intensity must be high enough to initiate dynamics but not so high that the sample is irreversibly damaged or destroyed. The damage threshold varies between samples and is approximately 2–3 mJ/cm^2 for 50 nm thick Cu(DCNQI)$_2$, obtained by trial and error. Damage from pumping is the limiting factor in how long an experiment can run so the pump intensity is strictly monitored and controlled during a measurement. Absorption measurements by Bart Smit (PhD) showed that the absorption of the sample does not depend on the polarisation of the pump beam.

The wavelength of the pump is approximately 620 nm and was chosen to coincide with the maximum absorption of the DCNQI$^-$ ion (see Figure 4.3), as the DCNQI molecule is responsible for most of the optical absorption of the sample [7]. Attempts to pump samples at the fundamental laser wavelength of 775 nm were unsuccessful—samples were destroyed at powers not high enough to optically induce a structural change—so a noncollinear optical parametric amplifier (NOPA) is used to generate 620 nm pulses. Figure 4.3 shows the molecular extinction of the DCNQI$^-$ ion in solution and the absorption at the NOPA wavelength of 620 nm is about 50 times greater than at the fundamental laser wavelength of 775 nm.

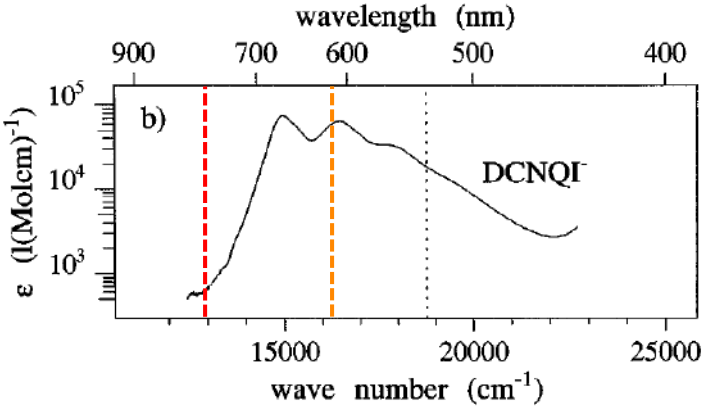

Figure 4.3: The molecular extinction ϵ of the DCNQI$^-$ ion in a CH_3CN solution at room temperature (adapted from [7]). The fundamental wavelength of our laser (775 nm) and the wavelength of our pump (620 nm) are indicated by the red and orange dashed lines.

The NOPA

The noncollinear optical parametric amplifier (NOPA) setup is shown in Figure 4.4 and works by splitting the incoming 775 nm beam into two paths, P1 and P2. The first path (P1) passes through a sapphire crystal to generate white light. The resulting white light pulse is chirped, meaning that different spectral components have different temporal positions in the pulse. This chirped beam will be our *seed* pulse. The remaining portion of the beam is sent along P2 and is frequency doubled to 387.5 nm in a β-Barium borate crystal (labelled BBO 1), and this will be the *pump* pulse for the NOPA.

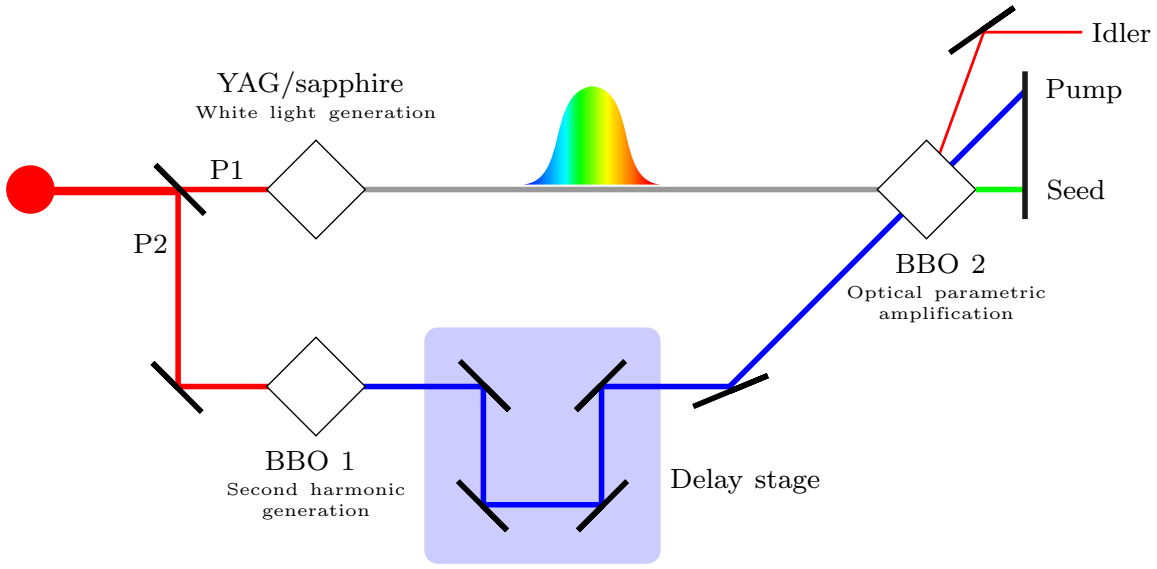

Figure 4.4: The noncollinear optical parametric amplifier (NOPA) setup used for generation of 620 nm pulses.

These two pulsed beams (the white light seed and the frequency doubled UV pump) are then overlapped in space and time in a second BBO crystal (labelled BBO 2). Depending on where the UV pulse spatially overlaps with the chirped white light pulse, photons can be generated with a frequency of at least 500–700 nm by optical parametric amplification, using the relation:

$$\nu_{\text{pump}} - \nu_{\text{seed}} = \nu_{\text{idler}}, \tag{4.2}$$

where ν_{pump} is the frequency of the UV pump pulse, ν_{seed} is the frequency of the white light seed pulse that the UV pump pulse spatially overlaps, and ν_{idler} is the frequency of the NOPA output pulse, known as the idler.

Given that the input pulses are 150 fs, it is reasonable to assume that the output pulses are < 200 fs [44]. As the electron probe pulses are longer than a picosecond, the optical pump pulses will not significantly affect the temporal resolution. The maximum power yield of the NOPA is typically 2 to 4 mW at 1 kHz which is much greater than the sample damage threshold, thus is more than sufficient.

The pump beam at the sample

The 620 nm output of the NOPA is focused using a 750 mm lens onto the sample inside the vacuum chamber. The diameter of the pump focus at the sample is approximately 100 μm and the area of exposed sample is 55 $\times$ 55 μm (see Figure 4.5). A typical fluence for time-resolved measurements on $Cu(DCNQI)_2$ is 1–2 mJ/cm^2.

It is important that the sample is homogeneously photoexcited so that the electrons probe as much excited sample as possible, for a good signal to noise ratio. Previous group member Andrea Rohwer measured the attenuation coefficient α of $Cu(DCNQI)_2$ for 600–700nm light to be $\alpha \approx 90{,}000$ cm^{-1} [45]. The penetration depth l is defined as the length of sample required to attenuate the transmitted intensity to $1/e \approx 0.37$ of its initial value and is related to the attenuation coefficient by $l = 1/\alpha$. Therefore

the penetration depth of 620 nm light is approximately 111 nm, compared to a typical sample thickness of 50 nm.

Using the relation $I/I_0 = \mathrm{e}^{-\alpha x}$, where x is depth and α is taken to be 90,000 cm^{-1}, the intensity at the back surface of a 50 nm thick sample is $I/I_0 \approx 0.64$. This agrees with transmission measurements made by Bart Smit, who estimated a sample transmission of 70%.

Additionally, previous group member Kerstin Haupt [46] calculated that reflection of the transmitted pump beam from the back surface of the crystal sample and consequent interference leads to an almost homogeneous intensity profile within a 30 nm thick sample. Thus it can be estimated that the volume of the sample is close to being homogeneously photoexcited by the pump beam.

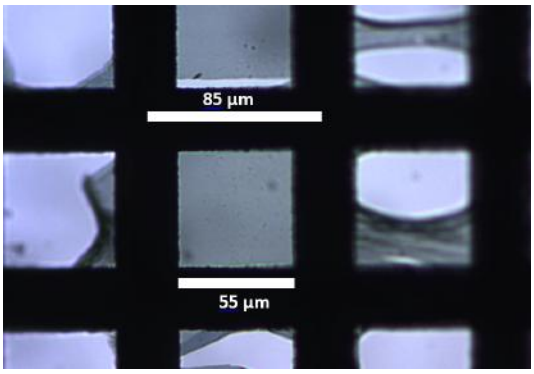

Figure 4.5: A TEM grid hole with a 50 nm thick, free-standing film of Cu(Me,Br-DCNQI)$_2$. The surrounding mesh holes will be covered so that the probe electrons only "see" the high quality crystal cut in the centre.

The probe

In order to generate electron pulses to probe the structure of the crystal sample, we make use of the photoelectric effect from a gold photo-cathode sputtered onto a window of the vacuum chamber. The work function of such gold films is 4.5 eV, thus ultraviolet light is needed to generate electrons. The fundamental 775 nm beam is frequency-tripled to obtain 258 nm laser pulses.

The 258 nm UV beam is focused onto the 10 nm gold photo-cathode with a spotsize of ~ 35 μm, as shown in Figure 4.6. The 258 nm (4.8 eV) laser pulses generate low-energy electrons (< 1 eV) from the gold film. As an electron energy of approximately 30 keV is required, the electrons are then accelerated by a strong electric field in the compact electron gun. An electric field of 10 MV/m is used to minimise the travel time of the electron pulses in order to limit the effect of pulse broadening due to Coulomb repulsion. Stronger electric fields risk arcing between the anode and cathode. After acceleration to 30 keV, the electron beam is focused by a magnetic lens placed just before the sample. See the MSc thesis of Bart Smit [47] for a more detailed description of the electron gun.

Thus the pulsed 258 nm laser beam yields a pulsed electron beam which can be focused and aligned through the sample, then onto the detection system using the magnetic

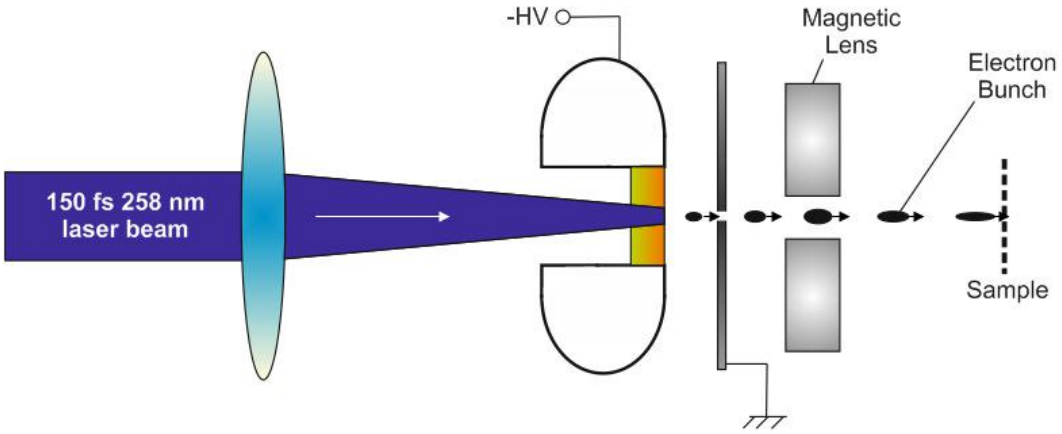

Figure 4.6: Sketch of the electron gun. The 258 nm pulsed laser beam is focused onto a gold photocathode to produce a pulsed electron beam, which is then accelerated by a strong electric field and focused using a magnetic lens. Figure from [47]).

lens. The spot size of the electron beam at the sample position is approximately 500 μm which is significantly larger than the area of sample exposed, meaning that the entire area of sample is probed by electrons.

Duration of the probe pulse

The electron pulses initially have the same temporal duration as the incident laser pulses. However, the electron pulses broaden significantly over time due to electrostatic repulsion. Pulse broadening is one of the major battles in UED experiments and as our time resolution is ultimately limited by the duration of the probe beam, it is important to limit or actively counteract the broadening of the electron pulses. This can be done in several ways, including:

- Accelerate the electrons as fast as possible (i.e., as high an accelerating electric field as possible, without arcing) to reduce the time over which the electron pulse can broaden.
- Further reduce the travel time of electrons between cathode and sample by using a compact electron gun or reducing the cathode to sample distance.
- Decrease the number of electrons per pulse, which will increase the time required to obtain the same signal.
- Use a compressor to actively counteract pulse broadening (e.g., see [48]).

As part of his MSc project, Bart Smit used ASTRA (A Space charge TRacking Algorithm [49]) to simulate the broadening of the electron pulses and to investigate the dependence of the pulse duration on the number of electrons per pulse, the accelerating electric field strength, the propagation distance, etc. [47]. The anode to sample distance is approximately 6 cm and an electron number of 6000 electrons per pulse is typically used for time-resolved experiments. Based on these numbers, the ASTRA simulations predict an electron pulse duration of 1.2 ps.

The electron pulse duration can be experimentally measured using a streak camera (see [48] for details). Streak camera measuremnts performed by Bart Smit [47] in our UED setup measured an electron pulse duration of 1.6 ps for approximately 10,000 electrons per pulse with a propagation distance of 5 cm. Measurements with varying electron number and pulse propagation distance were in good agreement with the ASTRA simulations.

It should be noted that our temporal resolution is not identical to the electron pulse duration but is more specifically the *response* of the system, which is a convolution of the electron pulse duration, the optical pump pulse duration, and any errors (for example, timing jitter between subsequent shots). The optical pump pulse duration is < 200 fs and errors due to timing jitter were shown to be 50 fs by a previous group member Günther Kassier [50], therefore the time resolution is dominated by the electron pulse duration.

4.3 Vacuum chamber

Most of the experimental setup was in place before my arrival, so please refer to the MSc thesis of Bart Smit [47] for a more detailed description of the vacuum chamber.

As it is necessary for the electron beam to propagate in a vacuum, the vacuum in the chamber is less than 10^{-8} mbar during experiments. A good vacuum also prevents arcing and the formation of condensation at low temperatures, a major problem in the first vacuum chamber built by the group.

Detection system

The detection system in the vacuum chamber combines a micro channel plate (MCP) with a phosphor screen and a charge-coupled device (CCD) camera fitted with an objective lens. The MCP amplifies the signal of a single diffracted electron via secondary emission. The amplified signal is then accelerated onto a phosphor screen and is energetic enough to photoexcite the screen. The emitted light is then imaged onto the CCD camera by the lens.

Cryostat and cooling procedure

During experiments the samples can be cooled down to approximately 45 K using a closed cycle helium cryostat. Sample temperatures of 90–150 K are typical for the pump-probe experiments on $Cu(DCNQI)_2$. Samples are cooled with a cooling rate of approximately 0.5 K per minute for two reasons: samples have been observed to suffer damage due to high cooling rates, and Pinteric et al. [51] found that the slower (bulk) samples were cooled, the more likely they were to undergo the M-I phase transition. A cold finger extends down into the chamber and is thermally coupled to the sample mount by a copper braid. By controlling the cold finger temperature and cooling rate, the temperature of the sample mount can be precisely controlled and therefore also the sample temperature. The cold finger is mechanically decoupled from the compressor to reduce vibrations at the sample.

4.4 Obtaining suitable samples for UED

In order to conduct transmission electron diffraction[1], very thin (< 100 nm) samples must be used for several reasons. Firstly, the sample must be transparent to electrons and thin enough so that secondary scattering events are rare. Secondly, the penetration depth of the pump beam must be large enough that a sufficient fraction of the sample is pumped, otherwise the diffraction patterns obtained will overwhelmingly reflect the unpumped structure and changes due to pumping may be too small to analyse or detect. Conversely, the sample must be *thick* enough such that the probability of scattering is high enough to generate a diffraction pattern with a good signal to noise ratio. The sample must also be thick enough to act as a bulk sample and undergo the phase transition, as it was previously unknown whether a thin monocrystalline film would exhibit the same behaviour as a bulk sample—a sample thickness of 50 nm corresponds to a mere 23 crystal unit cells ($a = b = 21.6$ Å). A sample thickness of 50 nm was found to be a good compromise between difficulties in sample preparation and diffraction pattern quality. Thicker samples often yielded lower quality diffraction patterns, whereas thinner samples were more difficult to reliably prepare.

The material that we study is the radical-ion salt Cu(Me,Br-DCNQI)$_2$ introduced in Chapter 2. Bulk samples of Cu(Me,Br-DCNQI)$_2$ are grown by electrolysis by Florian Hüwe in Würzburg [52] and are needle-like in appearance (see Figure 4.7) with a square cross-section and relatively flat shiny faces (the *a*-*c* and *b*-*c* planes). A Leica ultramicrotome and Micro Star diamond knife were used to directly cut the crystal along these planes, resulting in monocrystalline slices with a thickness of 50 nm.

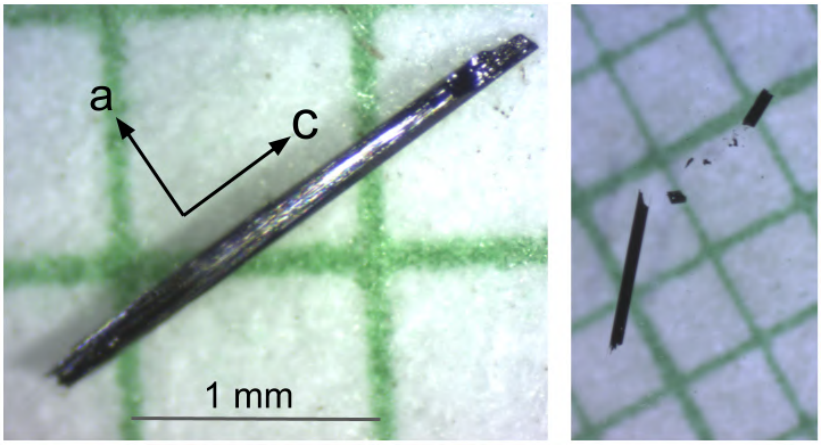

Figure 4.7: Crystal needle of Cu(Me,Br-DCNQI)$_2$ (left) and needle after cutting with a razorblade to obtain smaller fragments (right). Both imaged on mm graph paper.

There are other methods to produce thin samples depending on the crystal sample and resources available, including the "scotch tape method", focused ion beam milling, and thermal evaporation. The scotch tape method is only effective for layered crystals with very weak bonds between layers (e.g., graphite). Focused ion beam (FIB) milling involves milling a slab of sample from a bulk crystal using an ion beam and is promising

[1]Reflection electron diffraction can be used to characterise the surface of a material but not probe the bulk and yields lower quality diffraction patterns.

for preparing TEM samples but costly for small-scale projects and non-robust samples, and can result in sample contamination from the ion beam [53]. Thin-film deposition methods such as thermal evaporation have been previously used to create thin films of $Cu(DCNQI)_2$ crystals (e.g., [54]) but produce polycrystalline samples and require a substrate rather than resulting in a free-standing film. In our case, obtaining thin monocrystalline samples using a microtome was the simplest and fastest approach.

Our sample preparation procedure

As producing high quality thin samples is one of the greatest difficulties and bottlenecks in UED experiments, it was a major part of my project and the sample preparation procedure will be discussed in detail. Starting with bulk needles with dimensions of approximately $0.1 \times 0.1 \times 2$ mm^3, the preparation process is as follows:

1. Cut crystal needles into 0.3–0.5 mm pieces
Cut the needles on graph paper under a microscope (see Figure 4.7), using a clean razor blade to avoid getting any dirt or grease on the crystal.

2. Glue crystal piece onto a resin cone
Glue the crystal piece onto a resin cone using normal superglue (see Figure 4.8). This was achieved by first putting glue onto the resin, then picking the sample up with the glue. An alternative to gluing the crystal on the surface of the resin finger is to embed the sample *inside* the resin, as shown in Figure 4.9 (left). Although this did yield some successful samples that underwent the metal-insulator transition, the orientation of the crystal within the resin is unknown and it is impossible to accurately align the diamond knife to the crystal surface. Thus gluing is the preferred method to produce crystal cuts that result in a high quality diffraction pattern.

3. Trim the resin surface for cutting
The resin surface around the sample is trimmed in a trapezoidal shape as shown in Figures 4.8 (right) and 4.9 (left) to avoid resin getting in the way of the knife. The lines visible on the surface of the crystal visible in Figure 4.8 (right) are due to imperfections in the knife edge.

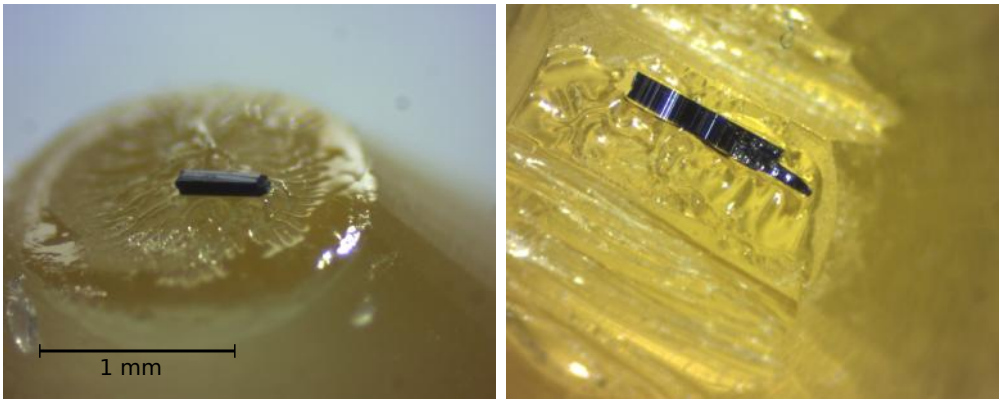

Figure 4.8: Left: A crystal fragment glued on top of a resin finger in preparation for the microtome. **Right:** A crystal fragment after cutting with the microtome. The lines visible on the cut fragment are due to imperfections on the diamond knife edge.

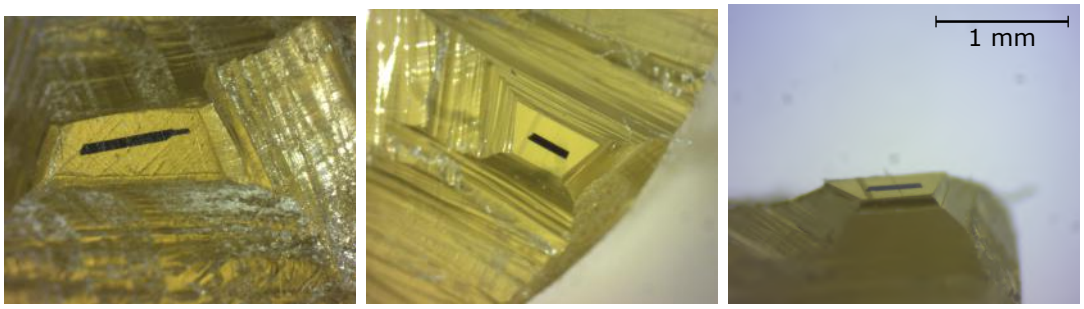

Figure 4.9: Embedding samples in resin for cutting. **Left:** Top view of an embedded crystal, after the surrounding resin has been trimmed in a trapezoidal shape. The textured surface of the resin makes it impossible to tell at which angle the crystal below sits, making proper alignment impossible. **Centre and right:** A different embedded crystal after cutting.

4. Prepare the microtome

Alignment of the knife edge with a flat crystal surface can be done using reflections from the shiny surface of the crystal and should be done as accurately as possible. The water level of the bath (see Figure 4.10) should be as low as possible whilst maintaining contact with the knife edge; too much water will hinder cutting and also transfer water droplets onto the crystal surface and the back of the knife. The diamond knife should be cleaned before and after every cutting session using a trimmed polystyrene rod and 100% ethanol.

5. Cut the crystal

Once the sample is aligned, cutting can begin. The microtome arm moves the sample in a cyclic motion (see Figure 4.10, left) and the arm moves forward by an amount equal to the cut thickness for each revolution. The sample is moved against the stationary diamond knife like moving cheese against a cheese grater. If everything is in order, a slice of crystal will be cut off and float on the surface of the water. A cutting speed of 0.4 mm/s regularly worked well for a desired cut thickness of 30–70 nm.

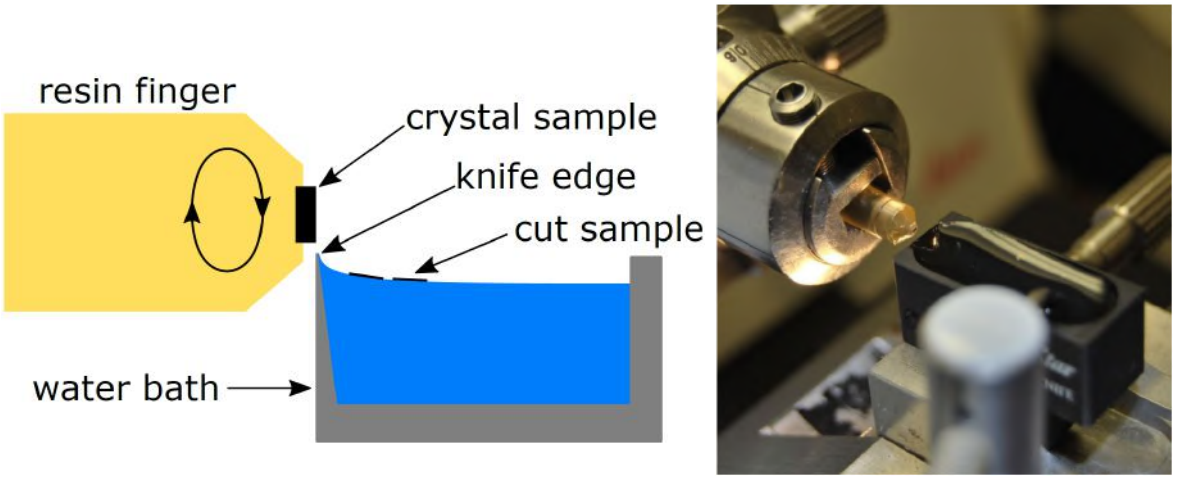

Figure 4.10: Left: The cutting motion of the microtome arm grates the crystal against the knife edge, causing thin slices of crystal to float onto the water surface. **Right:** A photo of the microtome arm holding a resin finger, above the diamond knife and water bath. Figures adapted from [46].

6. Pick up the cut sample from the water surface
Several methods can be used to transfer samples from the water surface to a TEM grid. I chose to lower the TEM grid onto the top of the sample and lift it from the water surface as this allowed careful alignment of the grid above the sample. Alternatively, the sample can be picked up from below or a small loop can be used to capture the sample and transfer it into a grid. No single method showed a clear advantage beyond personal preference. The grids most commonly used were copper TEM grids with 300 lines per inch although several different grid types were trialled (see Appendix A).

7. Let the sample dry on the grid
Once the sample has been transferred to a TEM grid it is usually accompanied by a large water droplet. Drying the grid using filter paper can cause serious damage to the fragile sample so we allow the grids to dry in air before storing. Even when air-drying, some mesh holes that are fully covered by sample appear to "pop" during the drying process, leaving behind little or no sample. With luck and perseverance, enough fully-covered mesh holes survive for imaging in the vacuum chamber.

8. Mount the TEM grids for imaging in the vacuum chamber
Conducting silver paste suitable for use in high vacuum is used to "glue" grids to a sample mount whilst maintaining good thermal contact between the grid and the sample mount. First a 100 μm aperture is glued to the sample mount, then the grid is manoeuvred on top of the aperture such that the desired mesh hole is aligned over the aperture hole, then glued in place. The aperture is to ensure that the electron beam only probes the chosen mesh-hole of high-quality sample (i.e., a single crystal with no damage or cracks). Figure 4.11 shows two examples of samples that have been glued, with the silver paint, aperture and copper grid labelled. The $Cu(DCNQI)_2$ sample is visible in Figure 4.11 (left) as dark areas on the copper grid. Bart Smit (PhD) found that it is possible to cut the grid into several pieces using nail trimmers, so if there are multiple good samples on a single grid then all could be imaged separately. The two grids shown in Figure 4.11 have been trimmed in this way.

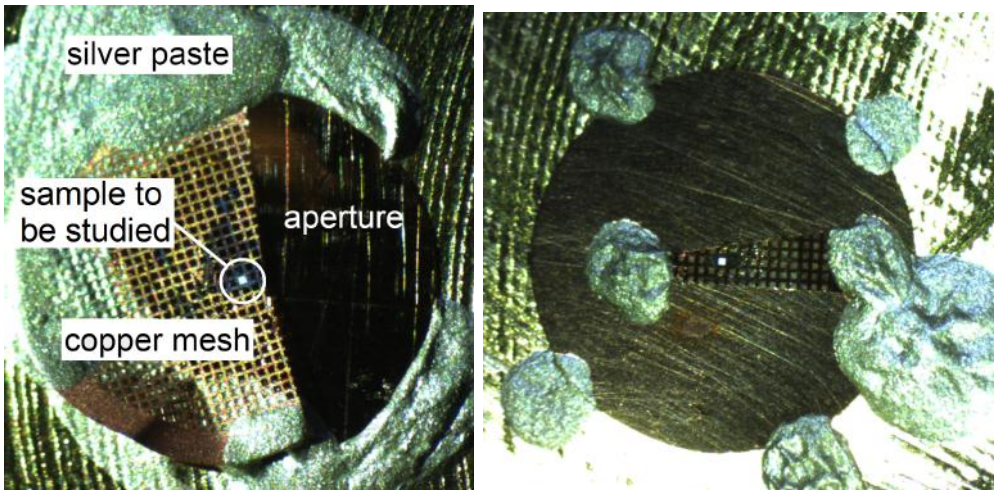

Figure 4.11: Two mounted samples. The silver paste holds the aperture and grid in place and maintains thermal coupling between the sample and the sample mount. Both grids shown have been cut with nail clippers as there were multiple good samples on a single grid. As shown in the right image, very thin sections of the grid can be cut.

4.5 Experimental procedure and post-processing of data

Once a high quality sample has been prepared, it is mounted in the vacuum chamber and a static diffraction pattern is acquired. If the pattern is of sufficiently high quality, the sample is cooled to below its phase transition temperature and a time-resolved measurement can be performed. The time at which the pump and probe arrive simultaneously at the sample is called *time zero*. Time zero can be estimated within ± 3 ps before starting an experiment using the "mesh trick" and a mini pump-probe experiment: the pump is used to excite photoelectrons from an empty TEM grid and the generated cloud of photoelectrons deflects the electron probe beam. By changing the time delay between the pump and the probe, the time at which they arrive simultaneously can be estimated. Figure 4.12 shows the shadow image of a TEM grid at several different pump-probe delay times. The cloud of photoelectrons becomes visible in the 3rd image.

Figure 4.12: Estimating time zero: each figure shows the shadow image of a TEM grid at different delay times between pump and probe. Illumination by an optical pulse of light results in excitation of a cloud of photoelectrons from the grid, which distorts the path of the electron probe. The time delay between pump and probe at which the cloud appears can be used to accurately determine time zero.

For pump-probe experiments on Cu(Me,Br-DCNQI)$_2$, a typical range of time delays will go from -10 ps to $+10$ ps in small steps (e.g., 500 fs to 3 ps), and longer steps can be taken for longer time delays (e.g., up to $+100$ ps in 10–30 ps steps). A single scan is made up of diffraction patterns acquired at each subsequent time delay. For example, one scan could be made up of patterns acquired at pump-probe delay times of -10 ps, -9 ps, ..., 9 ps, 10 ps. An unpumped image is also acquired at the start of each scan with the optical pump beam blocked. The unpumped image is used for normalisation and to check that the sample fully recovers in between pump pulses (the unpumped image should be identical to pumped images before time zero).

To improve the signal to noise ratio, the scan is repeated many times and the diffraction patterns acquired at each time delay are averaged. As an example, if the acquisition time for a single image is 30 seconds, a typical scan takes 10–12 minutes. When operating at 250 Hz, at least 40–60 scans are required for sufficient signal to noise, depending on the sample quality. For the two datasets presented in Chapter 5, 133 and 174 scans were acquired respectively in addition to a rough initial scan, requiring approximately 72 hours of measurements in total before the sample accrued too much damage to continue. Thus the total electron number per *averaged* diffraction pattern is approximately 5×10^9 electrons (6000 electrons per pulse, 250 Hz repetition rate, 30 seconds acquiring time per image and 100 scans).

Background subtraction

As well as averaging over many scans to improve the signal to noise ratio, a background subtraction can be applied to the averaged images before analysis. Background subtraction is useful due to the non-zero background over the entire image (the dark count of the MCP is non-zero) and the large amount of non-flat background around the beam block caused by inelastic and incoherent scattering.

Several simple methods to model the background were investigated and the most successful is as follows. The method makes use of two standard image processing filters, a median and a minimum filter, which are passed over the image and apply an operation to each pixel (e.g., [55]). In general, a filter samples a subregion around each image pixel in turn, where each pixel is labelled by its $\{i, j\}$ position. The filter calculates a particular property of the surrounding subregion and a corresponding value m_{ij} (e.g., the mean of the subregion). The size of the subregion (i.e., the filter size) is an input parameter and is constant for one application of the filter. Figure 4.13 shows an example of two different filter sizes of side length $d = 30$ and $d = 120$. In Figure 4.13 the filter is centred on a diffraction peak, but will also visit every other image pixel. As the filter passes over the entire image pixel by pixel, a second image is created, where the $\{i, j\}$ pixel values of the created image correspond to the output values m_{ij} of the applied filter.

The median filter is applied to the diffraction pattern image to remove erroneous pixel values (e.g., any broken pixels on the CCD). In this case the filter replaces the $\{i, j\}$ pixel with the local median. After applying the median filter, the minimum filter is applied to the image to "see past" the intense diffraction peaks and sample the true background value that the peak is sitting on. This means that the minimum filter must be significantly larger than the diffraction peaks. For example, Figure 4.13 illustrates that a minimum filter of size $d = 30$ is too small, thus would estimate too high a value for the local background. A filter size of $d = 120$ is more suitable as it samples pixels far from the peak. However, if the minimum filter is too large, the minimum value

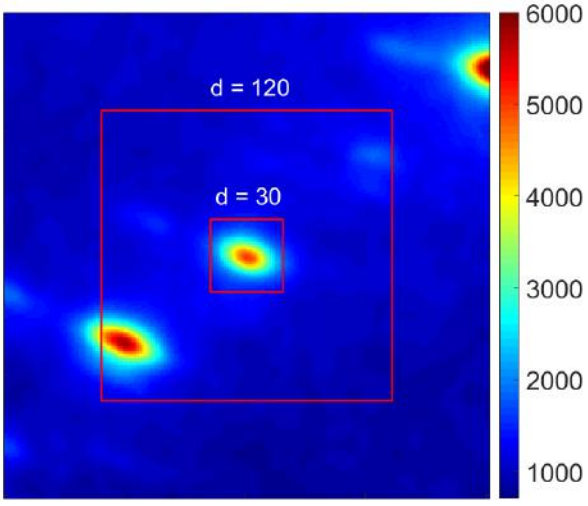

Figure 4.13: Two different minimum filter sizes are indicated by the red boxes, with side length $d = 30$ pixels and $d = 120$ pixels. The larger filter is able to sample a value closer to the 'true' local background.

obtained is no longer a 'local' background. This is important for peaks close to the beam block, where the background varies hugely over relatively short distances on the detector.

The effect of applying the median and minimum filters sequentially is to calculate an approximation to the true background whilst ignoring the diffraction signal. This approximation can be subtracted from the original image to produce an image with less background. The model background will be relatively smooth so any noise in the background will remain after subtraction—the diffraction image is not smoothed by the background subtraction process.

For demonstration, Figure 4.14 shows diffraction patterns before and after background subtraction, displayed in colour on the same scale (note the use of a log scale). It can be seen that the background around the beam block has been greatly reduced, although not completely eliminated. However, peaks in the first order now sit on a

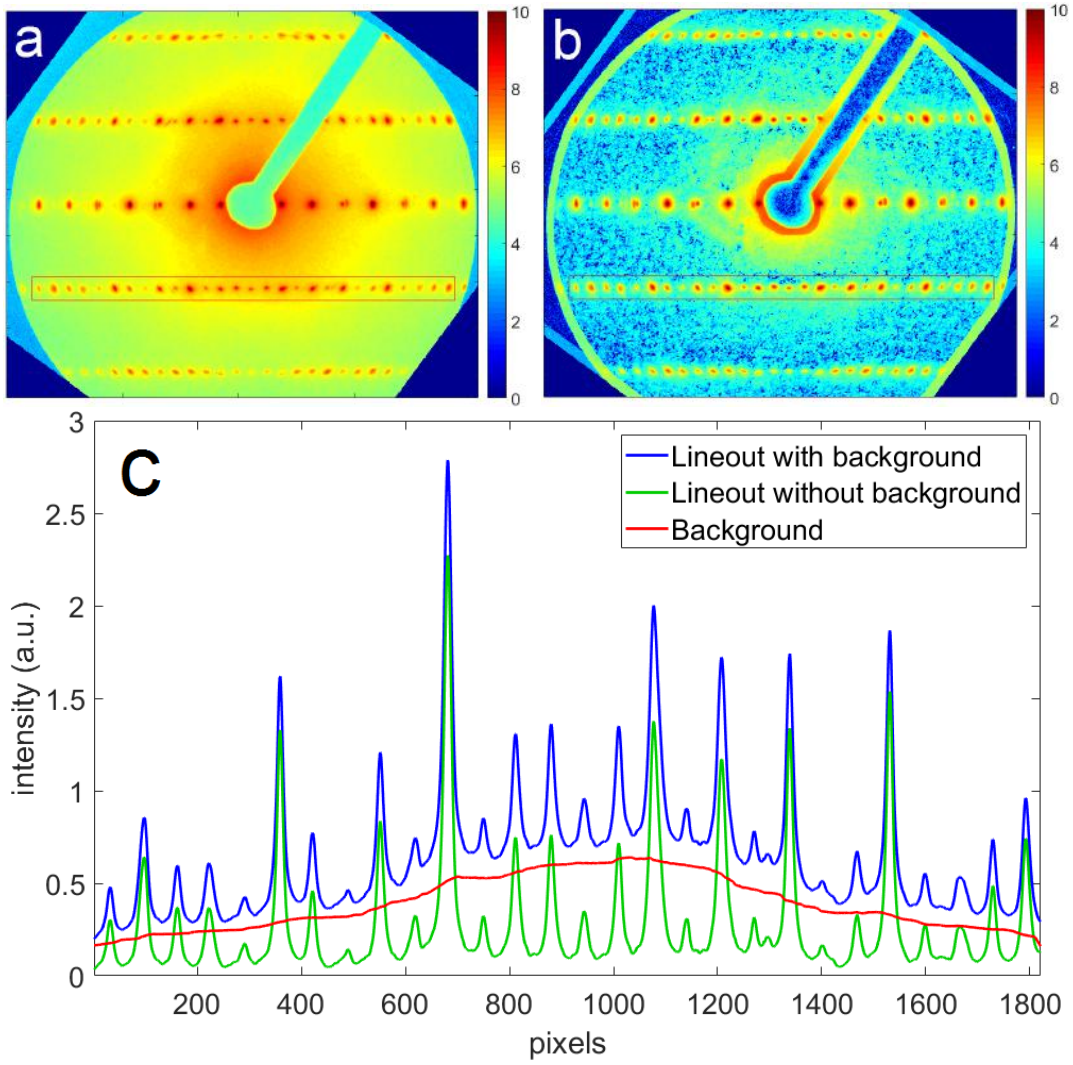

Figure 4.14: a and b: A comparison of diffraction patterns before and after applying the background subtraction (left and right, respectively). The colormap is plotted on a log scale. **c:** Lineouts of a diffraction order, before (blue) and after (green) the background subtraction. The fitted background is shown by the red line.

similar (close to zero) background and can be more easily compared. The edge effects around the border of the image and the beam block are a direct result of the filters applied and peaks in these areas should be omitted from analysis.

It is important that a background subtraction has a negligible effect on the data to be analysed, i.e., that the background subtraction does not qualitatively change the data. To study the validity of the proposed background subtraction method, the areas highlighted in Figure 4.14 (a) and Figure 4.14 (b) are integrated over and plotted in Figure 4.14 (c) in blue and green respectively. Plotted in red is the equivalent lineout of the modelled background (the modelled background is not shown). From Figure 4.14 (c) it can be seen that a background subtraction does not qualitatively affect the shape of the peaks and preserves even relatively small nuances and details in the integrated peak shapes. Importantly, the integrated intensities of even very weak peaks remain unaffected, beyond the subtraction of the more-or-less constant local background. The modelled background is not perfectly smooth but is sufficient for current purposes.

It can be seen that the background subtracted diffraction pattern does not go to zero in between peaks (diffraction peaks can be treated as Lorentzian or Gaussian distributions, which extend to infinity). As a further test of the reliability of the background subtraction, Lorentzian functions were manually fitted to each peak and the sum calculated. The result is shown in Figure 4.15 and shows that if treated as individual Lorentzians, the sum of the separate Lorentzian peaks (red) is an excellent match to the background subtracted data (blue). Lorentzian functions yielded a much better fit

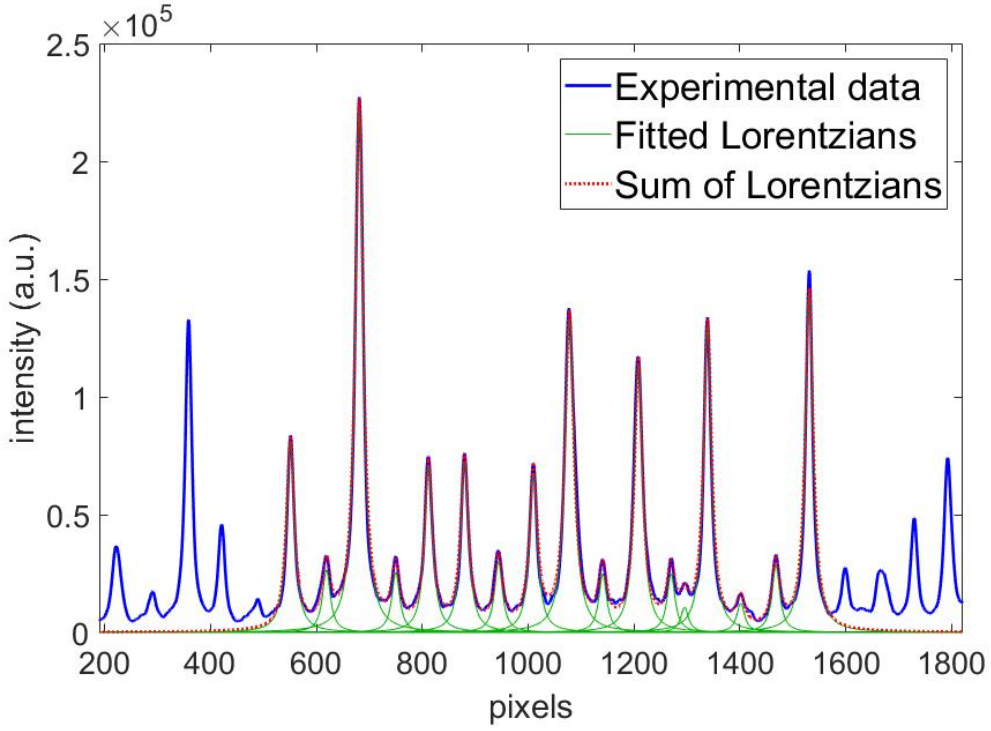

Figure 4.15: Fitting the background-subtracted data (blue) to individual Lorentzians (green). The sum of the manually fitted Lorentzians (red dashed line) is an excellent fit to the background-subtracted data.

than Gaussian functions.

With Figure 4.15 in mind, a possible future option for modelling the background would be to fit a two dimensional Lorentzian function to each diffraction peak. The Lorentzians could then be used to recreate a 'perfect' diffraction pattern, with experimental diffraction peaks replaced with a Lorentzian at the corresponding position and with the same integrated intensity.

Analysis of time-resolved scans

Once the data has undergone a background subtraction, the temporal response of different peaks can be analysed by following their intensities as a function of delay time between the pump beam and the probe beam. The centre of the peak of which the temporal response is to be analysed is selected by hand and all pixels within a particular radius of the peak centre are integrated over. If multiple peaks are selected for analysis, the peak centres are selected manually and the integrated intensities are summed for each time step to yield a single number. If analysing multiple peaks, those within the same {hkl} family are chosen as they should display similar responses (i.e., percentage intensity change and temporal evolution), as they correspond to the same lattice planes (see Section 3.2).

Figure 4.16 shows an example transient. In this example, the integrated intensity change of a single peak (normalised to its unpumped intensity) is tracked with respect to delay time between pump and probe. Upon photoexcitation (delay time = 0 ps), the intensity of the peak decreases and is plotted as a function of delay time. A fit can then be applied (see Appendix B for further details on the fitting procedure).

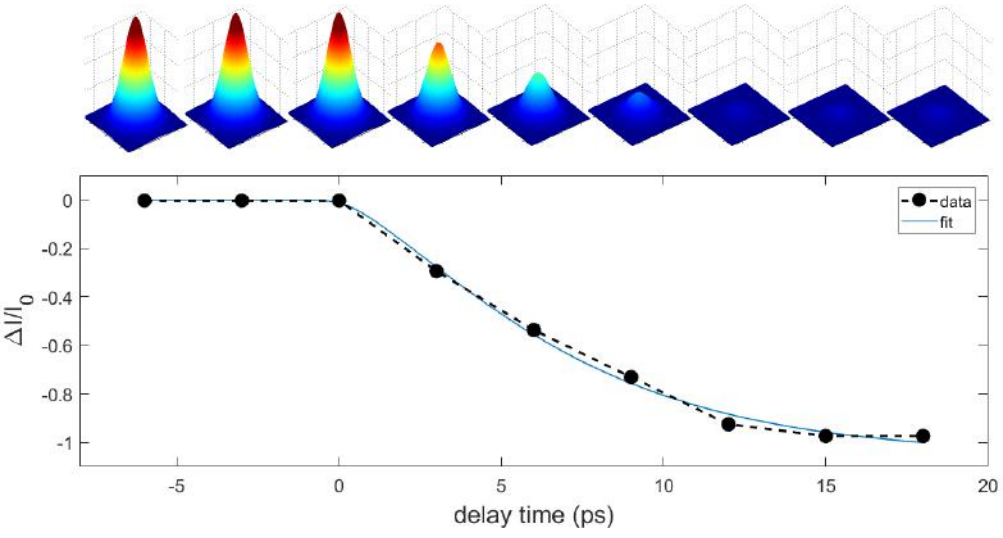

Figure 4.16: An example transient, showing the integrated intensity of a single peak plotted against the time delay between the pump beam and the probe beam.

5. UED measurements on Cu(Me,Br-DCNQI)$_2$

As introduced in Chapter 2, the radical-ion Cu(DCNQI)$_2$ salts exhibit interesting properties that can be studied by UED. The particular salt we have chosen to study is Cu(Me,Br-DCNQI)$_2$ due to its relatively high metal-insulator (M-I) transition temperature compared to the deuterated dimethyl alloys. Conductivity measurements performed on the bulk needles by Florian Hüwe [52] show that Cu(Me,Br-DCNQI)$_2$ undergoes a M-I transition at 155 K, with an abrupt drop in conductivity of about an order of magnitude (2×10^5 S/m to approximately 10^4 S/m) as shown in Figure 5.1.

The aim of our UED experiments is to study the ultrafast structural changes of a monocrystalline Cu(Me,Br-DCNQI)$_2$ sample upon photoexcitation of the insulator-metal (I-M) phase transition. Even in complex systems with many hundreds of possible degrees of freedom, it has been seen that only a few key structural modes dominate the molecular motions—a huge reduction in complexity [56]. It is these large-amplitude modes that we wish to identify in the case of the optically induced I-M transition of Cu(Me,Br-DCNQI)$_2$ and their relationship with the electronic properties of the sample.

As conductivity cannot be directly measured by a UED experiment, the evidence that the crystal has undergone its metal-insulator transition is the appearance of trimer peaks upon cooling, as explained in Chapter 2. Any reference to a transition temperature in the context of our experiments is the temperature at which the trimer peaks first become visible during the cooling (this temperature typically varies between 120–180 K but samples have even been observed in the insulating phase at room temperature). Suppression of the trimer peaks upon photoexcitation indicates that the crystal is being "pumped" from its insulating phase (trimerised crystal planes) to its conducting phase (equidistant crystal planes). Analysis of the main Bragg peak intensities upon pho-

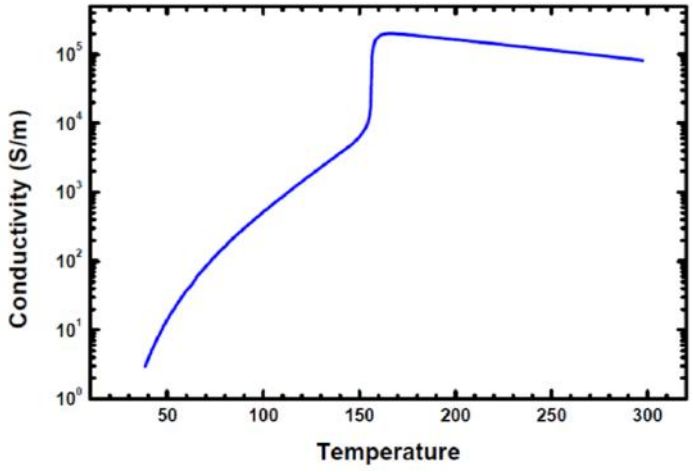

Figure 5.1: The temperature dependence of the conductivity of Cu(Me,Br-DCNQI)$_2$ upon cooling as measured by Florian Hüwe on a bulk needle [52].

toexcitation offers additional insight on the structural response of the crystal lattice. The temperature- and time-dependent behaviour of the trimer peaks will be discussed in two regimes, demonstrating that the metal-insulator transition occurs upon cooling and that the insulator-to-metal phase transition can be induced by an optical laser pulse. This will be followed by an analysis of the main Bragg peak intensities on ultrafast timescales. The analysis of the trimer and Bragg peak dynamics will elucidate the relationship between different degrees of freedom under the highly non-equilibrium conditions upon photoexcitation.

5.1 Steady-state analysis

When cooled below the transition temperature, trimer peaks appear at one third of the reciprocal lattice constant c^* as a result of the change in real-space periodicity. Figure 5.2 shows diffraction patterns after background subtraction (see Section 4.5) of Cu(Me,Br-DCNQI)$_2$ at 285 K with no trimer peaks (left) and at 170 K with several trimer peaks clearly visible between the main Bragg peaks (right). The maximum

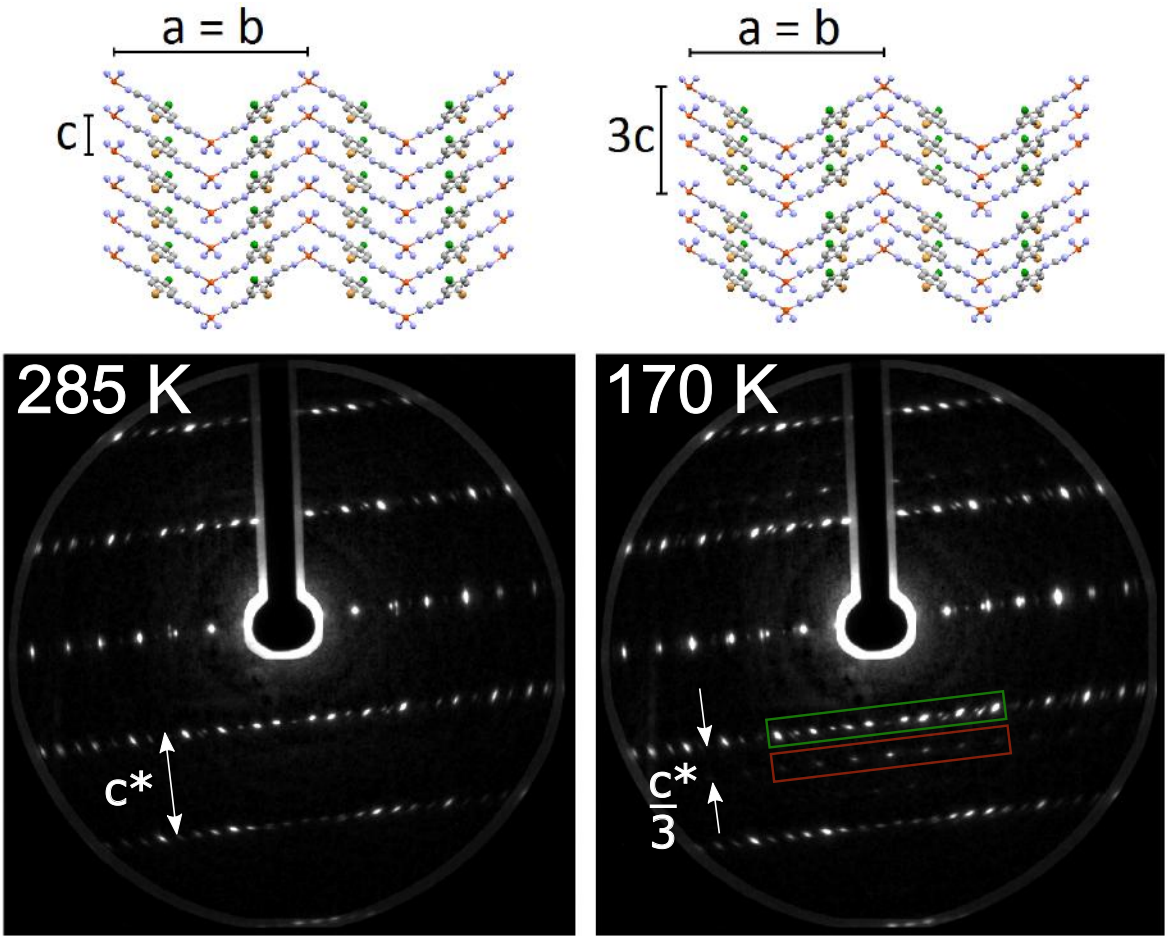

Figure 5.2: Static electron diffraction patterns of Cu(Me,Br-DCNQI)$_2$ at 285 K (left) and 170 K (right), along with the corresponding schematics of the crystal structure. Several trimer peaks are visible at 170 K as a result of the tripling of the periodicity in the real space crystal lattice.

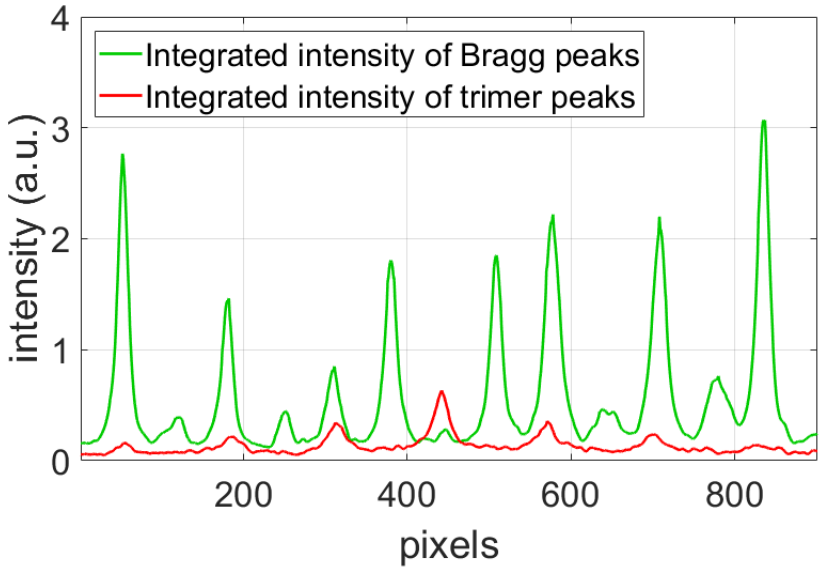

Figure 5.3: Lineouts taken from the 170 K pattern in Figure 5.2 to compare intensities of the Bragg (green) and trimer (red) peaks.

intensity of trimer peaks for a high quality sample is typically around 10–15% of the average Bragg peak intensity. For example, Figure 5.3 compares the integrated lineouts of the Bragg and trimer peaks indicated by the green and red boxes respectively in Figure 5.2.

Previous studies have observed abrupt first-order changes in the sample's conductivity upon cooling, accompanied by abrupt changes in certain lattice parameters: the c lattice constant (e.g., [7]) and the N–Cu–N angle α (e.g., [19]), as discussed in Chapter 2. In contrast to these abrupt changes, we observe a much more gradual temperature dependence of the trimer peak intensities. Upon cooling, the trimer intensities do not have a step-like temperature dependence but 'grow' into the pattern as the temperature decreases. The presence of the trimer peaks corresponds to the opening of a band gap, i.e., an additional periodicity in the crystal due to the periodic lattice distortion (PLD). The trimer peak intensity is proportional to the square of the amplitude of the PLD (how far the ions' positions are modulated from the high temperature structure), therefore an increase in trimer intensity with decreasing temperature indicates an increasing PLD amplitude with decreasing temperature.

Plotted in Figure 5.4 is the integrated intensity of a single trimer peak during cooling from 284 K to 175 K. The trimer peaks for this sample first become clearly visible at 243 K, which is higher than the typical trimer appearance temperature (120–180 K). Regardless of the absolute temperature of the phase transition, the relationship of peak intensity with temperature is a common feature of all our measurements. Previous groups have made similar measurements on bulk samples using x-ray diffraction but with different observations. Moret et al. [8] observed a similar "growing" of the trimer peak intensities with lowering temperature, similar to our own measurements. In contrast, Kato et al. [11] observed a step-like increase in trimer peak intensity at the M-I transition temperature as shown in Figure 5.4 (right). This indicates that the PLD occurred within a temperature range of several Kelvin, a much smaller range than observed in our thin film samples.

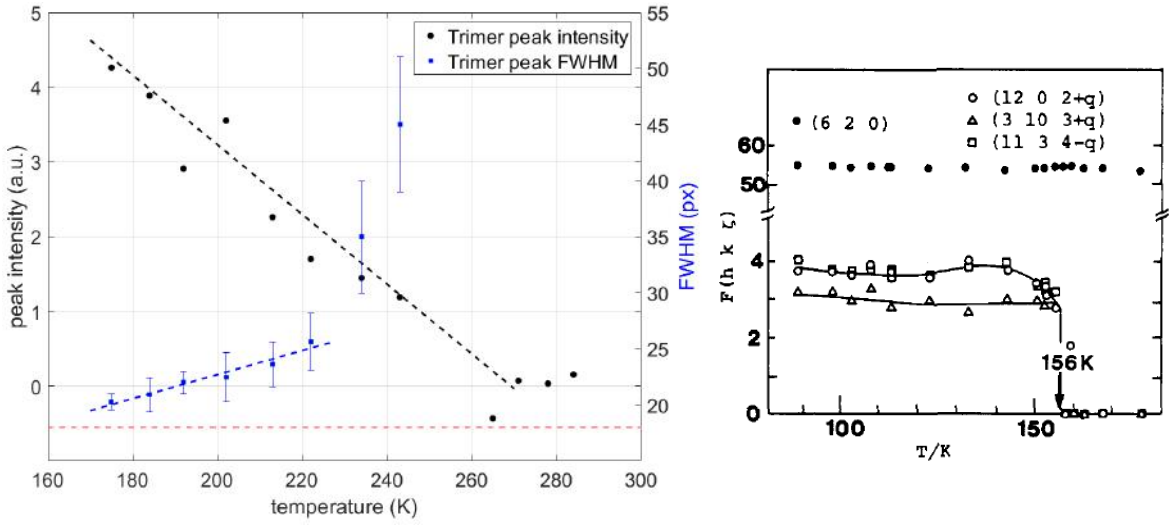

Figure 5.4: Left: The temperature dependence of the integrated intensity (black) and FWHM (blue) of a single trimer peak upon cooling from 284 K to 175 K. The dashed lines through the data are to guide the eye, and the red dashed line indicates the average Bragg peak FHWM of 18 pixels. **Right:** The temperature dependence of the intensity of two different trimer peaks (lower plots) and a 'representative' Bragg peak (upper plot) taken from x-ray diffraction measurements by Kato et al. [11].

It should be emphasised that even if the electronic phase transition *is* first order (for example, Figure 5.1), PLD formation is not necessarily a first order phenomenon. As shown by von Schütz et al. [26], 20% of the sample volume must be in the trimerised state for a bulk needle to undergo the first order drop in conductivity. In other words, a small fraction of crystal domains could undergo the PLD, which would be observed in diffraction patterns by the appearance of weak trimer peaks, but the macroscopic crystal would still be conducting. Once the sample has been cooled further and the fraction of domains in the trimer phase exceeds the threshold, the sample undergoes the first order electronic phase transition and becomes insulating. Upon further cooling, more crystal domains will undergo the structural phase transition and the crystal remains insulating.

The FWHM of a particularly high quality sample's trimer peaks during cooling was analysed and the results are shown in Figure 5.4. The FHWM decreases from approximately 45 pixels to 20 pixels upon cooling. As the transverse coherence length of the electron beam is approximately 100 Å, the decreasing FWHM of the trimer peaks could be indicative of the phase transition occurring in domains in the sample. The average FHWM of the Bragg peaks is approximately 18 pixels (compared to the final trimer peak FWHM of 20 pixels) and is indicated in Figure 5.4 by the red dashed line. Conversely, if the FHWM had been observed as constant with respect to temperature (i.e., the trimer peaks first appear with a particular FHWM which remains constant upon further cooling), this could suggest trimerisation of the crystal in domains greater in size than the coherence length of the electron beam.

Some additional considerations can be taken into account to try and explain the trimer peaks' behaviour upon cooling. Firstly, Kato et al. [11] cooled their bulk needles using a cold nitrogen stream, meaning that the entire bulk of the needle cools at the same rate

(i.e., all crystal domains are at the same absolute temperature). In our experiments however, direct thermal contact of the thin film edges with the TEM grid may result in the border/outer region of the film being cooled more than the inner portion of the film, resulting in a temperature gradient across the sample. Similarly, keeping in mind how large an effect pressure can have on a sample's phase transition temperature, a free-standing film may experience a pressure differential exerted by the TEM grid, shifting the transition temperature in different regions of the film. Both a temperature and pressure gradient would result in different regions of the crystal experiencing different local conditions and therefore undergoing the structural phase transition at different stages of the cooldown. These effects would again be reflected in the FHWM and intensity of the trimer peaks.

Contraction along the c crystal axis

An additional piece of the puzzle is the temperature dependence of the c lattice constant: an abrupt contraction along the c axis has been observed in both our experiments and by several groups previously. For example, Figure 5.5 (left) shows the c lattice constant for a variety of Cu(DCNQI)$_2$ salts that undergo the M-I phase transition [11]. The discontinuous behavior of c is common to all samples that undergo the metal-insulator phase transition and consistently occurs close to the phase transition temperature. The magnitude of the abrupt decrease is approximately 0.5% of the room temperature c lattice constant. Additionally, Figure 5.5 (right) similarly shows the (negative) expansion of the c crystal constant in the alloy of deuterated and un-

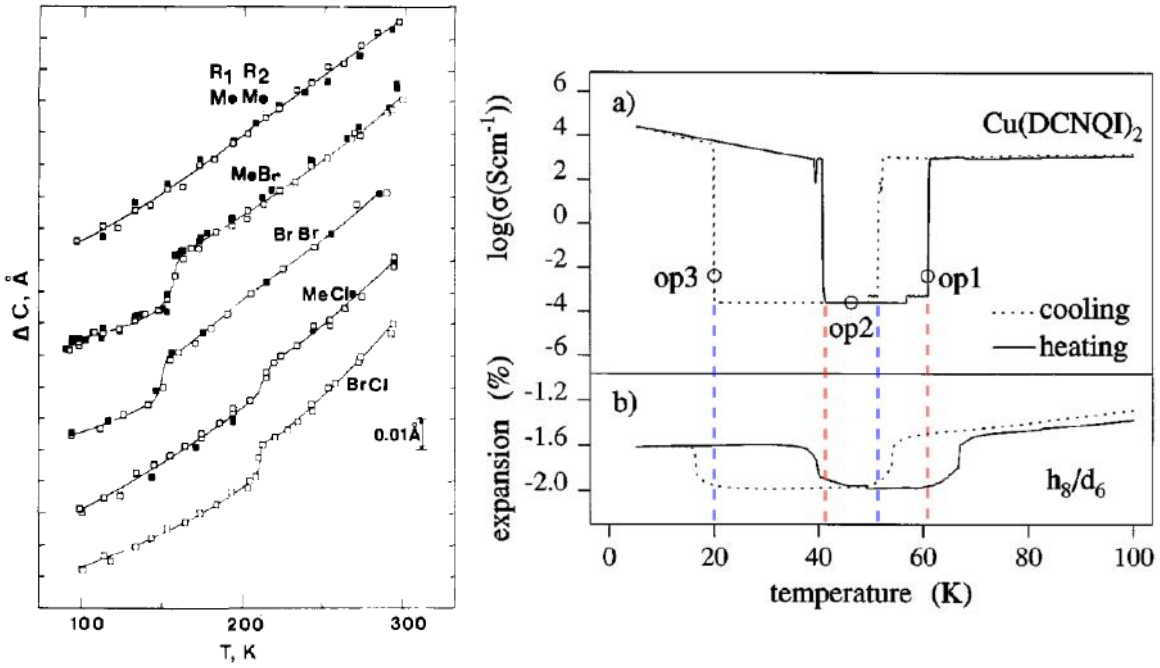

Figure 5.5: Left: The temperature dependence of the c lattice constant for five different Cu(DCNQI)$_2$ salts [11]. All Group II salts experience an abrupt decrease in c close to the M-I transition. **Right:** The temperature dependence of the c lattice constant of deuterated Cu(DCNQI)$_2$ [7]. The abrupt changes in c correspond closely (but not exactly) to the phase transition temperatures, as indicated by the dashed lines.

deuterated h_8/d_6-(70%/30%) Cu(DMe-DCNQI)$_2$, which reenters the metallic phase at lower temperatures [7]. It can be seen that upon cooling (dotted line in Figure 5.5, right), the c crystal constant abruptly *decreases* by approximately 0.4% close to the higher temperature M-I transition, then *increases* at a similar temperature to the I-M transition to the metallic phase. Similar behaviour is observed upon heating, suggesting a close relationship between the c lattice constant and the electronic state of the sample. This is reminiscent of the N–Cu–N angle α discussed in depth in Chapter 2. The red and blue dashed lines are to emphasise the slight difference in temperature between the conductivity changes and the contraction.

As the increase in α is only partially compensated for by other changes in the unit cell, the increase in α causes an overall *decrease* in the c lattice parameter of the crystal unit cell. Using the Cu(DCNQI)$_2$ structure files determined by x-ray diffraction on bulk needles by the Barbour Group (Stellenbosch University), we found that an increase in α of 2.7% (along with other minor changes) was accompanied by a contraction of the c lattice constant of 1.8%.

Our electron diffraction data from cooling thin film samples shows similar features to an extent. The relative measure of the c lattice constant can be extracted from experimental diffraction patterns as follows: two lines are fitted through the outer orders of the diffraction pattern at each temperature (Figure 5.6). The distance between these lines is proportional to c^* (or $1/c$) and is found for each diffraction pattern during cooling. After normalising to the room temperature c lattice constant, the relationship between c and temperature can be plotted. (Figure 5.6, right). We see a range of behaviours from our samples but there are some similarities. For example, the magnitude of the contraction from room temperature to 100 K is similar for all samples and is approximately 1.5–2.0% (similar to literature values). Secondly, the appearance of the trimer peaks tends to coincide with a more abrupt decrease in the c constant of approximately 0.04% (0.015 Å), again similar to literature values. We can conclude that an abrupt decrease in c is *linked* to the phase transition, potentially as a direct result of a decrease in the N–Cu–N angle, in both 50 nm thick samples and bulk needles.

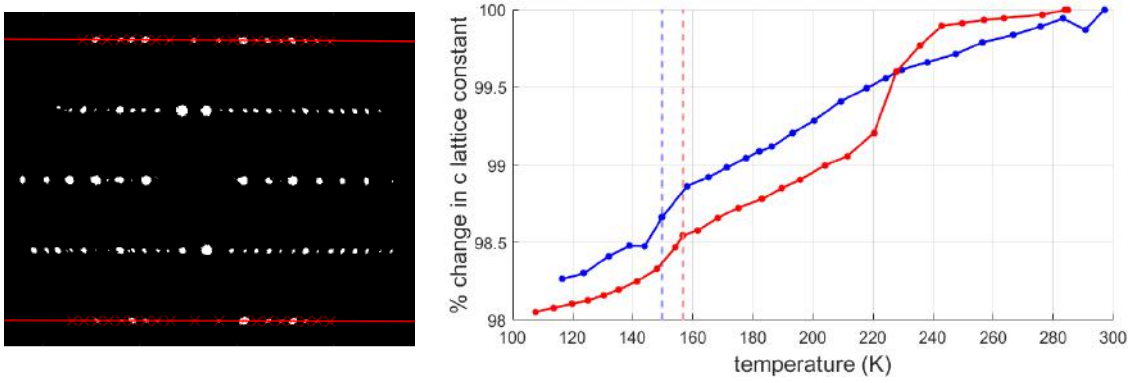

Figure 5.6: Left: A relative measure of the c lattice constant can be extracted from diffraction patterns by finding the average distance between the two outmost orders (proportional to $1/c$) and plotted with respect to temperature. **Right:** Two representative samples and plots of their c lattice contraction during cooling. The faint dashed lines mark the temperatures at which trimers appear in the respective cooldowns.

5.2 Time-resolved analysis

Once the sample has entered the insulating phase, an insulator-metal (I-M) transition can be induced by means of an optical laser pulse, as demonstrated by Karutz et al. [7] in the case of bulk needles. In our UED experiments the timescale of the PLD destruction upon photoexcitation can be deduced from the disappearance or suppression of the trimer peaks in the diffraction patterns. Any other structural changes in the unit cell (e.g., bonds stretching or bending) will be reflected in Bragg peak intensity changes.

It is important to separate the concepts of a periodic *structural* distortion (the PLD) and the periodic *electronic* distortion (the CDW). These two effects are closely associated and are often interchangeable in equilibrium conditions. However, in the highly non-equilibrium conditions induced by an ultrashort laser pulse, care must be taken. The 'pump' laser pulse transfers energy instantaneously to the electrons in the crystal sample, instantaneously destroying the CDW as shown schematically in Figure 5.7. The heavy atoms of the crystal lattice respond much more slowly than the electrons, meaning that the PLD is destroyed on much longer timescales of hundreds of femtoseconds to picoseconds. It is only the PLD that can be directly observe with electron diffraction, thus suppression of trimer peaks is specifically the destruction of the PLD—a *structural* effect—and not the charge density wave.

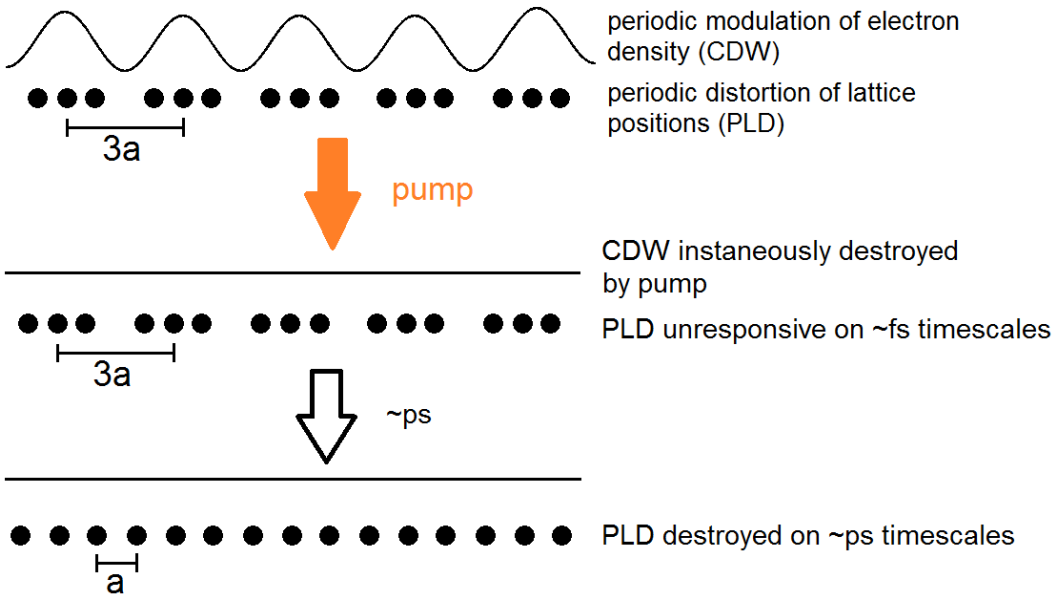

Figure 5.7: Schematic illustrating that the periodic modulation of the electron potential (the CDW) is immediately destroyed upon photoexcitation, but the periodic lattice distortion is destroyed on longer (~ps) timescales.

Fitting the time-resolved data

The transient data can be modelled as either a single exponential decay with a time constant of τ_1 and amplitude c_1, or the sum of an exponential decay and an exponential rise, with time constants of τ_1 and τ_2, and amplitudes c_1 and c_2, respectively:

$$\frac{\Delta I(t)}{I_0} = \begin{cases} 0, & \text{for } t < t_0 \\ c_1(1 - \mathrm{e}^{-t/\tau_1}) + c_2(1 - \mathrm{e}^{-t/\tau_2}), & \text{for } t \geq t_0 \end{cases} \tag{5.1}$$

To account for the electron pulse duration, the pump pulse duration and any additional timing error (e.g., jitter), which will 'smear out' the data, the model given by (5.1) must be convolved with a Gaussian response function. As described in Section 4.2, the response function is dominated by the electron pulse length of approximately 1.2 ps, and the FWHM of the response function is chosen to be the estimated electron pulse duration for each experiment. Due to the simplicity of (5.1), the convolution can be done by hand and the analytical result is in terms of error functions (see Appendix B for details). MATLAB's built-in function `lsqcurvesfit` can then be used to optimise the parameters c_1, c_2, τ_1, τ_2 and t_0 from the user-defined fit given in (B.2).

It is important to note that the temporal resolution of the setup results in a lower limit of the time constants that can be resolved. For example, if the output of the fitting process is an optimised decay constant of 500 fs, the conclusion is that the decay occurs with a time constant *faster* than 1.2 ps, not that the time constant *is* 500 fs.

Temporal response of trimer peaks

The I-M transition in Cu(DCNQI)$_2$ can be studied in two different regimes (or at two different "operating points"), as discussed in Section 2.1: just below the transition temperature, and far below the transition temperature. These two operating points are illustrated in Figure 5.5 (right) from the measurements of Karutz et al. [7] and labelled as 'op1' and 'op2' respectively. When optically exciting deuterated Cu(DMe-DCNQI)$_2$ at op1, Karutz et al. observed a rise time of the conductivity of 30 ps (time resolution limited) and decays on the order of hundreds of nanoseconds, as shown in Figure 5.8 (a) and discussed previously in Section 2.1. Additionally, the photoinduced conductivity reaches conductivity of the sample in the metallic (high temperature) phase. These two observations indicate that the crystal is pumped into its metallic phase when photoexcited at op1. However, pumping the sample at op2 yields a response corresponding to conventional photoconductivity and the metallic (high temperature) conductivity is not reached, indicating that the metal-insulator phase transition is not induced by photoexcitation at op2 and that the conducting phase is not induced in the bulk needle.

We were able to perform complimentary experiments on two different Cu(Me,Br-DCNQI)$_2$ samples at 10 K and 40 K below their respective phase transition temperatures and our results are shown in Figure 5.8 (c) and (d). If the presence of trimer peaks is taken to be equivalent to the crystal being in the insulating phase, we observe something similar to Karutz et al. [7]: when pumping close to the I-M transition temperature the trimer peaks are fully suppressed within 2 ps and remain suppressed for longer than 70 ps as shown in Figure 5.8 (c), indicating that the sample is pumped

into the metallic (high temperature) phase and stays there for longer than 70 ps—the I-M transition has been successfully photoinduced.

As the trimer peaks increase in intensity with cooling, this means the peaks tend to be very weak just below the phase transition temperature. For a greater signal to noise ratio during the experiment yielding the data shown in Figure 5.8 (c), the electron number per pulse was increased and larger time steps were taken. Thus the data shown in Figure 5.8 (c) indicates that the suppression occurs within 3 ps (the delay time between the data points taken close to time zero) and lasts more 70 ps, but does not offer any further information on the rate of suppression.

Conversely, if the sample is pumped many Kelvin below the phase transition temperature (i.e., at op2, deep in the insulating phase), we observe something *different* to the conventional photoconductivity of Karutz et al. [7]. Upon photoexcitation, a full suppression of the trimer peaks occurs within 2 ps—the structural transition is successfully photoinduced at op2 (again note that the data is resolution limited). The trimer suppression is followed by a 'recovery' of the trimer peaks within tens of picoseconds, as shown in Figure 5.8 (d). That is, the sample only briefly enters the metallic phase before relaxing back to the insulating phase. The time constant associated with the decay of the trimer peaks is less than 1.2 ps and the time constant of the rise is 6.5 ps.

It should be emphasised that our results show *structural* changes within the sample, enabling us to conclude that the short-lived trimer peak suppression at op2 is direct evidence of a structural phase transition within the sample. In comparison, Karutz et al. [7] were measuring a macroscopic property (conductivity) and were unable to induce the I-M transition when pumping at op2. The difference is likely to be a consequence of thin-film versus bulk behaviour: as discussed in depth in Section 4.2, the entire volume of our 50 nm thick samples is directly photoexcited by the pump beam, whereas the penetration depth for the 0.2 mm diameter samples of Karutz et al. is only 100 nm, meaning only unit cells near the surface are photoexcited. When pumping at op1, Karutz et al. were able to conclude that the volume of the crystal that underwent the phase transition was at least 100 times greater than the volume that was directly photoexcited, meaning that the transition was able to 'propagate' through the sample but unable to propagate when pumping at op2. As we are directly photoexciting the entire volume of our sample and sensitive to structural changes, we are able to confirm the occurrence of the phase transition at op2 in a directly excited volume (a fluence of 2 mJ/cm^2 corresponds to approximately 0.5 photons per unit cell of Cu(DCNQI)$_2$).

Temporal response of main Bragg peaks

So far the temporal analysis has been on the trimer peaks and their link to the electronic state of the sample. However, a wealth of information is contained within the dynamics of the Bragg peak intensity distribution. One possible structural change that could be reflected in the Bragg dynamics is the N–Cu–N angle α. It is well known that α plays an important role in the phase transition of Cu(DCNQI)$_2$ and experiences an abrupt increase in thermal equilibrium close to the transition temperature (e.g., [19]). Thus it is likely that a change in α may occur on ultrafast timescales when the crystal is

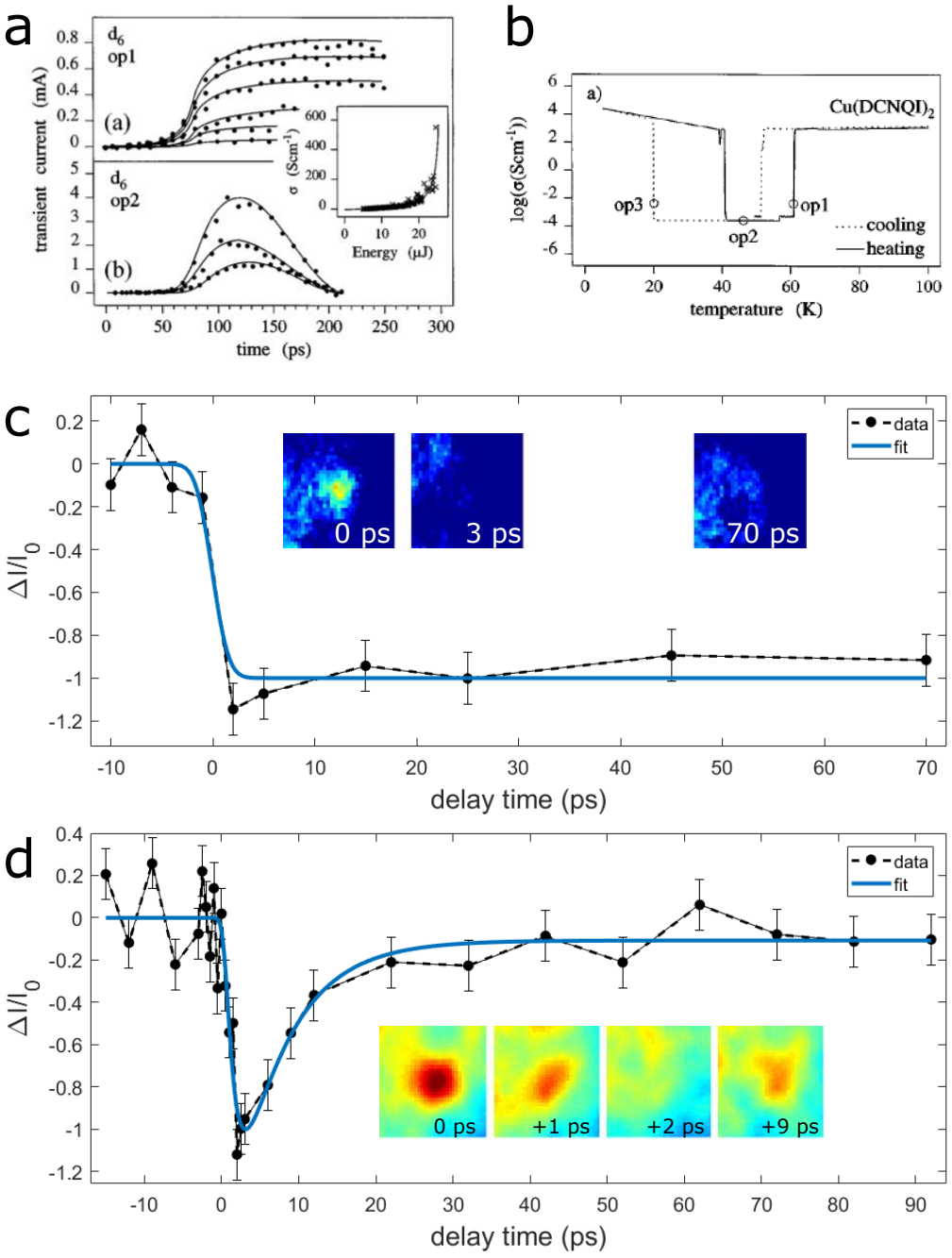

Figure 5.8: a and b: The transient current response of deuterated Cu(DMe-DCNQI)$_2$ upon photoexcitation at two different operating points, op1 and op2. **c and d:** The ultrafast response of trimer peaks when photoexcited close to the phase transition temperature (i.e., at op1), and well below the phase transition temperature (i.e., op2), shown in (c) and (d) respectively. The insets show a representative trimer peak at different time delays for visualisation of the suppression.

optically pumped across the I-M phase transition. This sort of structural change may be discernible from the ultrafast Bragg peak intensity changes.

As it is a big step to translate transients and changes in reciprocal space into the corresponding real-space changes, first the time-resolved Bragg peak data will be presented, followed by a discussion about the conclusions that can be reached from Bragg data in general, as well as our data in particular. It is important to note that changes in the Bragg peak intensities upon photoexcitation are not solely due to structural changes within the crystal unit cell. For example, heating of the sample will lead to an overall decrease in Bragg peak intensity (the Debye-Waller effect) and must not be confused with changes of the crystal lattice.

As an example we will consider a single set of results. Shown in Figure 5.9 (left) is a difference map of diffraction patterns taken at two different pump delay times, one before time zero ("unpumped") and one after time zero ("pumped"). The difference map displays "pumped minus unpumped", where red is positive and indicates peaks that increase upon pumping, and blue is negative and indicates peaks that decrease upon pumping. Green indicates no change upon pumping. It is clear that the trimer peaks (indicated by the black arrows) are blue and therefore decrease upon photoexcitation, as was discussed in detail in the previous section. Certain Bragg peaks also decrease in intensity upon pumping (e.g., the {101} peaks, circled in blue), but other peaks *increase* upon photoexcitation and show up as red in the difference map (e.g., the {402} peaks, circled in green).

Figure 5.9 (right) shows the transient response of three different {hkl} groups ({101}, {400} and {402}) upon pumping at op2, 40 K below the phase transition, with maximum intensity changes $\Delta I/I_0 = 3.6\%$, 0.12% and 4.5% respectively (note that the {400} data has been magnified by a factor of 40 in Figure 5.9).

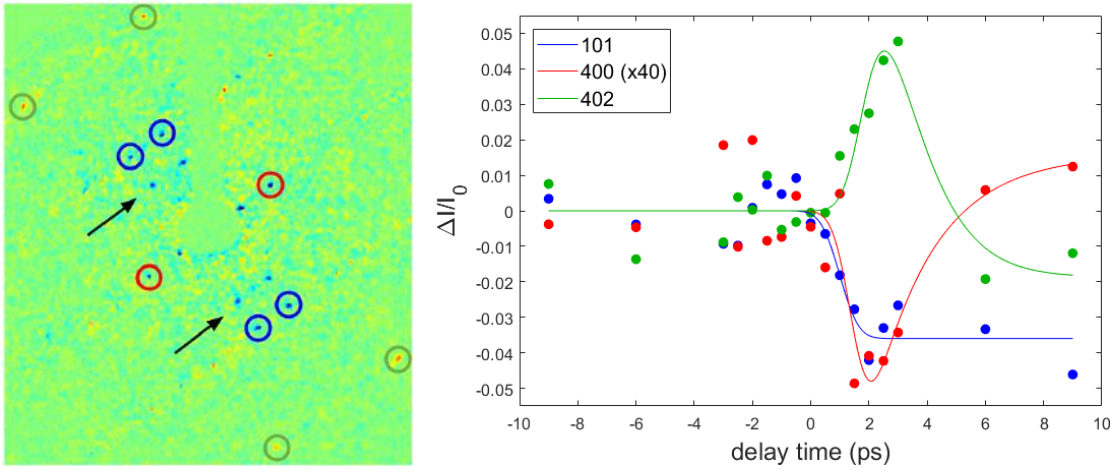

Figure 5.9: The ultrafast response of three different Bragg peak {hkl} groups upon photoexcitation at op2 (40 K below the phase transition). **Left:** A difference map highlighting the differences between the data before and after time zero. The peaks with analysable transients are circled: {101} (blue), {400} (red) and {402} (green). **Right:** Transients for the selected peak intensities (data points and fit, see Appendix B). Note that the 400 transient has been magnified by a factor of 40.

Note the Bragg peaks exhibit a range of behaviours:

- {400}: peaks that initally **decrease** in intensity and **recover**.
- {100}: peaks that initially **decrease** in intensity and **do not recover**.
- {402}: peaks that initally **increase** in intensity and **recover**.

The initial time constants τ_1 of all three Bragg families upon photoexcitation is below the temporal resolution of 1.2 ps, as is the initial decay of the trimer peaks. To emphasise, this is not the same as saying that the physical processes have the *same* time constant, just that any differences cannot be resolved by the current setup and resolution.

However, links can still be deduced from the data. The recovery time constants τ_2 associated with the {400} and {402} peaks are approximately 2 ps (this has a large error due to the few data points available and noise). Additionally, the fact that the {400} and {402} peaks recover on similar timescales suggests that there could be a strong coupling between the {400} and {402} groups and the dynamics they correspond to, or that they correspond to the same structural change. For example, a particular structural change associated with the phase transition could result in an intensity redistribution that includes a *decrease* in the {400} intensities and an *increase* in the {402} intensities. As the sample is being pumped well below the phase transition temperature, the change is only transitory. Thus if this structural change was induced upon photoexcitation and then the sample returns to its initial pre-pumped structure, we would observe something similar to what is shown in Figure 5.9.

Another interesting observation that can be made from Figure 5.9 is that the 'recovery' of the {400} and {402} Bragg peaks ($\tau_2 \approx 2$ ps) is faster than the recovery of the trimer peaks ($\tau_2 \approx 6.5$ ps). As the Bragg peak changes correspond to structural lattice changes (as well as other effects such as heating) and the trimer peaks correspond to the amplitude of the periodic lattice distortion (PLD), the differing time constants of recovery may shed light on the driving forces behind the PLD recovery. For example, if the Bragg peaks return to their initial (pre-time zero) state faster than the PLD recovers, this could suggest that the PLD recovery is only energetically favourable once the crystal structure is in a particular structural conformation.

It should be emphasised that finding similarities or relations in the dynamics of different {hkl} groups cannot be intuitively interpreted in terms of possible real-space dynamics, but this approach still offers a potential 'footprint' when it comes to simulating the effects of real-space changes and their corresponding changes in reciprocal space. Although the above discussion is largely speculation to serve as an example, it demonstrates that the analysis of Bragg peak dynamics can ultimately lead to an understanding of the real-space lattice changes. Further analysis and interpretation is the ongoing work of Bart Smit (PhD).

5.3 Interpreting Bragg intensity changes

It is one thing to identify Bragg peak dynamics and time constants from the UED transients, and another thing entirely to link these Bragg intensity changes to real-space dynamics in the crystal structure (e.g., changes in bond lengths or angles). Although interpreting the Bragg changes has mostly been the work of Bart Smit (PhD), I will briefly outline the methods used so far. Clues on where to start come from literature (e.g., the N–Cu–N angle α) and static x-ray diffraction data collected by the Barbour group (Stellenbosch University) on bulk needles of Cu(Me,Br-DCNQI)$_2$ at three temperatures: 298 K, 130 K and 90 K.

From the crystal structure files obtained from x-ray data, the static crystal structures at 298 and 130 K can be compared in real space. Firstly, there is agreement with literature values of the increase of α upon cooling: an increase in α from 125.3° to 128.2° (+ 2.9°) from room temperature to 100 K was reported by Kato et al. [11], and our x-ray data shows an increase of 125.4° to 128.3° (+ 2.9°) from 298 K to 130 K. However, changes in α are not the only structural changes occurring upon cooling, and other lattice parameters can be studied using crystal-visualisation software such as Mercury [57].

Using CrystalMaker [41], we can simulate the corresponding diffraction patterns directly from the crystal structure files and do a similar comparison of the structures but in reciprocal space. That is, for every x-ray-determined crystal structure, we can generate the diffraction pattern that it would yield (subject to certain approximations, see Section 3.3). As we know that α increases upon cooling in the x-ray structure files, we can look at the differences between the 298 K and 130 K files in reciprocal space to see what changes are 'expected' upon cooling of a (bulk) crystal sample, and see if the same changes are observed in the thin films of our time-resolved UED experiments upon photoexcitation. Although it is not expected that the highly non-equilibrium conditions of UED will yield changes identical to that of heating within several picoseconds, similarities between the two sets of results may be used to draw conclusions. However, at longer timescales it is expected that heating will dominate due to phonon-phonon coupling.

Shown in Figure 5.10 are two difference maps, "pumped minus unpumped" on the left (as shown before in Figure 5.9), and the simulated difference map between the 298 and 130 K x-ray structures (a change in α, among other changes). Although there are clearly many differences, a few similarities are indicated by the black lines. For example, the {402} peaks are red in both difference maps, while their neighbours are blue. Comparisons such as this will enable us to link known real-space changes to changes in reciprocal space.

To further investigate the possible photoinduced molecular dynamics, possible motions (such as the changing of angles between bonds or the stretching of bonds) can be individually simulated and compared to the pump-probe difference maps.

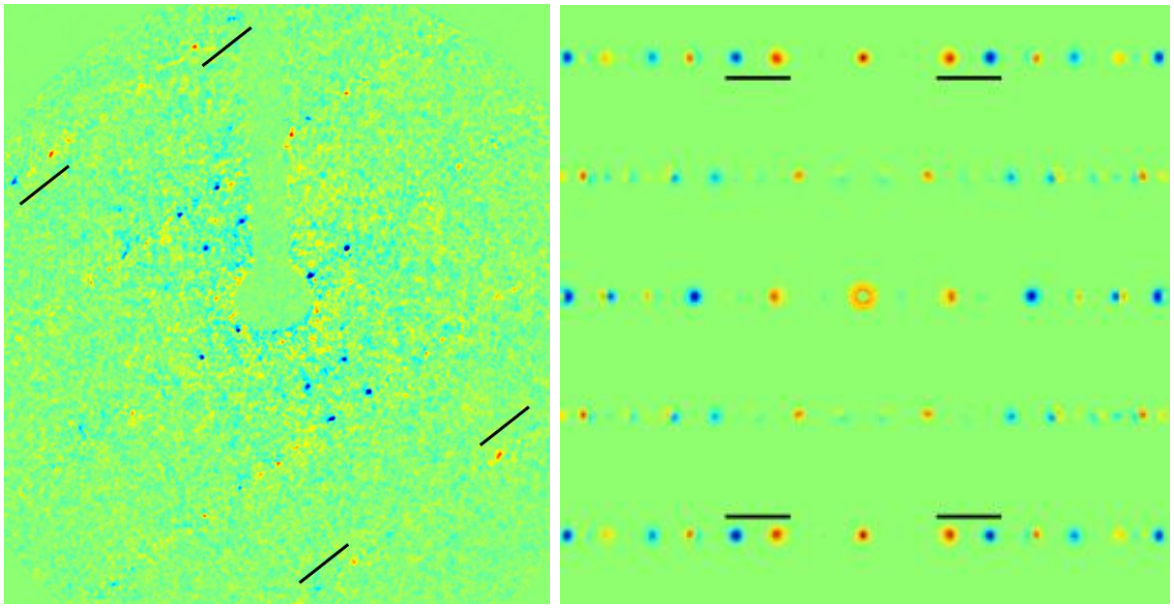

Figure 5.10: Left: Difference map of a diffraction pattern taken 3 ps after time zero minus a diffraction pattern taken before time zero. **Right:** Difference map simulated using the data obtained from x-ray measurements at 298 K and 130 K (Barbour group, Stellenbosch University).

6. Summary

The radical-ion $Cu(DCNQI)_2$ salts are highly conducting at room temperature and undergo a dramatic metal-insulator (M-I) transition upon cooling or under pressure. The insulator-metal (I-M) transition can be induced on ultrafast timescales by an optical laser pulse. Due to the highly variable nature of organic solids, $Cu(DCNQI)_2$ salts can exhibit a wide range of systematically tunable transition temperatures, depending on the exact chemical composition of the salt, with potential applications such as high-speed optical switches in solid state electronics.

To study the structural changes associated with the phase transition, 50 nm thick monocrystalline samples of $Cu(Me,Br\text{-}DCNQI)_2$ were prepared using an ultramicrotome and studied using ultrafast electron diffraction in transmission. The samples were observed to undergo the M-I transition upon cooling in our vacuum chamber, inferred from the appearance of 'trimer' peaks at $\frac{1}{3}c^*$ in the diffraction pattern that are a direct consequence of the increased three-fold periodicity of the crystal structure in the insulating phase. The trimer peaks serve as evidence that the phase transition has occurred and that 50 nm films behave similarly to bulk samples, even though the films are only 23 unit cells thick. The trimer peak intensities (proportional to the square of the amplitude of the periodic lattice distortion) have a strong temperature dependence, growing in intensity as the temperature is further decreased over many tens of Kelvin.

Once a sample undergoes the M-I phase transition and trimer peaks are observed in the steady-state diffraction patterns, we were able to photoinduce the insulator-metal phase transition by homogeneously exciting the sample with a 620 nm laser pulse generated by a noncollinear optical parametric amplifier (NOPA). The induced structural dynamics within the crystal lattice can be followed using our UED setup which has a temporal resolution of 1.2 ps. We studied two different regimes: photoexcitation of the sample at approximately 10 K and 40 K below the phase transition temperature. When photoexcited 10 K below the transition temperature, the crystal is pumped into its high temperature (conducting) phase with a time constant of less than 1.2 ps (resolution limited) and remains in the high temperature phase for timescales longer than 70 ps, inferred from the full and lasting suppression of the trimer peaks. Conversely, when photoexcited 40 K below the transition temperature, the sample again enters the high temperature phase with a time constant of less than 1.2 ps but *returns* to the low temperature (insulating) phase on slower timescales of 6.5 ps—the trimer suppression is short-lived.

Time-resolved analysis of the Bragg peak intensity distribution upon photoexcitation can be linked to the real-space structural lattice changes associated with the I-M transition. Three groups of Bragg peaks were identified as having a significant intensity change upon photoexcitation, followed by a range of behaviours. For example, in the short-lived trimer suppression data, two Bragg peak groups recover to their equilibrium intensities on faster timescales than the trimer peak recovery (approximately 2 ps, compared to 6.5 ps). Such observations hint at the interplay and cooperation between different degrees of freedom within the crystal unit cell.

The next step for the project is to translate the ultrafast changes in reciprocal space into real-space dynamics in order to create a "molecular movie" of the structural dynamics as the sample undergoes the I-M phase transition, tracking the motions of atoms on timescales of picoseconds. The corresponding real-space changes will be investigated by simulating potential lattice changes using structures for the hot and the cold phase determined by x-ray diffraction. For example, the N–Cu–N angle α has been closely linked to the phase transition by previous steady-state studies on bulk samples, therefore serves as one starting place for simulation and comparison with the time-resolved diffraction data.

In general, the potential applications of UED are broad, combining the improvements in crystallisation techniques for complex organic molecules such as proteins with the advancement of temporal resolution and signal to noise ratios in UED setups. In addition to non-equilibrium studies in solid state physics, UED offers the potential to directly study chemical and biological processes on their primary timescales and at an atomic level.

Bibliography

[1] Schwoerer, M. and Wolf, H.C.: *Organic Molecular Solids*. John Wiley & Sons, 2007.

[2] Scapin, G.: Structural biology and drug discovery. *Current pharmaceutical design*, vol. 12, no. 17, pp. 2087–2097, 2006.

[3] Dudek, R.C. and Weber, P.M.: Ultrafast diffraction imaging of the electrocyclic ring-opening reaction of 1, 3-cyclohexadiene. *The Journal of Physical Chemistry A*, vol. 105, no. 17, pp. 4167–4171, 2001.

[4] Thorne, R.E.: Charge-density-wave conductors. *Physics Today*, vol. 49, no. 5, pp. 42–48, 1996.

[5] Aumüller, A., Erk, P., Klebe, G., Hünig, S., Ulrich Von Schütz, J. and Werner, H.-P.: A radical anion salt of 2, 5-dimethyl-N,N'-dicyanoquinonediimine with extremely high electrical conductivity. *Angewandte Chemie International Edition*, vol. 25, no. 8, pp. 740–741, 1986.

[6] Hünig, S., Sinzger, K., Jopp, M., Bauer, D., Bietsch, W., von Schütz, J.U. and Wolf, H.C.: Deuterium-induced phase transition of an organic metal - an unusual isotope effect. *Angewandte Chemie International Edition in English*, vol. 31, no. 7, pp. 859–862, 1992.

[7] Karutz, F., Von Schuetz, J., Wachtel, H. and Wolf, H.: Optically reversed Peierls transition in crystals of Cu(dicyanoquinonediimine)$_2$. *Physical Review Letters*, vol. 81, no. 1, p. 140, 1998.

[8] Moret, R.: Structural instabilities in molecular conductors: Silver and copper salts of dicyanoquinonediimine, (DCNQI)$_2$X (X= Ag or Cu). *Synthetic Metals*, vol. 27, no. 3-4, pp. 301–307, 1988.

[9] Yamakita, Y., Furukawa, Y., Kobayashi, A., Tasumi, M., Kato, R. and Kobayashi, H.: Vibrational studies on electronic structures in metallic and insulating phases of the Cu complexes of substituted dicyanoquinonediimines (DCNQI). A comparison with the cases of the Li and Ba complexes. *The Journal of Chemical Physics*, vol. 100, no. 4, pp. 2449–2457, 1994.

[10] Hiraki, K. and Kanoda, K.: Comparative study on the magnetism and conductivity of (DI-DCNQI)$_2$M, (M=Li, Cu, Ag). *Synthetic Metals*, vol. 86, pp. 2103–2104, 1997.

[11] Kato, R., Kobayksihi, H. and Kobayashi, A.: Crystal and Electronic Structures of Conductive Anion-Radical Salts, (2,5-R$_1$,R$_2$-DCNQI)$_2$Cu (DCNQI = N,N'-Dicyanoquinonediimine; R$_1$, R$_2$ = CH$_3$, CH$_3$0, Cl, Br). *J. Am. Chem. Soc.*, , no. 3, pp. 5224–5232, 1989.

[12] Aonuma, S., Sawa, H., Okano, Y., Kato, R. and Kobayashi, H.: Synthesis of DMe-DCNQI-d_7 and deuterium-induced metal-insulator transition of (DMe-DCNQI-d_7)$_2$Cu. *Synthetic Metals*, vol. 58, no. 1, pp. 29–38, 1993.

[13] Sinzger, K., Christoph, H., Kremer, R.K., Metzenthin, T. and Lengauer, C.L.: The Organic Metal (Me_2–DCNQ1)$_2$Cu: Dramatic Changes in Solid-state Properties. *J. Am. Chem. Soc.*, vol. 115, pp. 7696–7705, 1993.

[14] Kato, R., Aonuma, S., Sawa, H., Hiraki, K. and Takahashi, T.: Unexpected isotope effect in 13C-substituted (- C≡ N) molecular conductor (DMe-DCNQI)$_2$Cu (DMe-DCNQI= 2, 5-dimethyl-N, N'-dicyanoquinonediimine). *Synthetic Metals*, vol. 68, no. 2, pp. 195–198, 1995.

[15] Bauer, D., Maier, B., Schweitzer, D. and von Schuetz, J.U.: Thermopower of deuterated and alloyed Cu-DCNQI-crystals - Evidences for a "quite normal reentry" of the conductivity. *Synthetic Metals*, vol. 71, pp. 1887–1888, 1995.

[16] Nishio, Y., Kajita, K., Sasaki, W., Kato, R., Kobayashi, A. and Kobayashi, H.: Thermal and magnetic properties in organic metals (DMe-DCNQI)$_2$Cu, (DMeO-DCNQI)$_2$Cu and (DMe$_{1-x}$MeBr$_x$-DCNQI)$_2$Cu: Enhancement of density of states. *Solid State Communications*, vol. 81, no. 6, pp. 473–476, 1992.

[17] Kato, R., Sawa, H., Aonuma, S.i., Tamura, M., Kinoshita, M. and Kobayashi, H.: Preparation and physical properties of an alloyed (DMe-DCNQI)$_2$Cu with fully deuterated DMe-DCNQI (DMe-DCNQI = 2, 5-dimethyl-N, N'-dicyanoquinonediimine). *Solid State Communications*, vol. 85, no. 10, pp. 831–835, 1993.

[18] Vuletic, T., Pinteric, M., Loncaric, M., Tomic, S. and von Schütz, J.U.: Non-ohmic electrical transport in the Peierls-Mott state of deuterated copper-DCNQI systems. *Synthetic Metals*, vol. 120, no. 1-3, pp. 1001–1002, 2001.

[19] Kato, R.: Conductive copper salts of 2, 5-disubstituted N, N'-dicyanobenzoquinonediimines (DCNQIs): structural and physical properties. *Bulletin of the Chemical Society of Japan*, vol. 73, no. 3, pp. 515–534, 2000.

[20] Inoue, I.H., Kakizaki, A., Kobayashi, A., Kato, R., Kobayashi, H., Namatame, H. and Fujimori, A.: Electronic Structure of the Organic Conductor (DMe-DCNQI)$_2$Cu Studied by Photoemission Spectroscopy. *Physica C*, vol. 189, pp. 2691–2692, 1991.

[21] Matula, R.A.: Electrical resistivity of copper, gold, palladium, and silver. *Journal of Physical and Chemical Reference Data*, vol. 8, no. 4, pp. 1147–1298, 1979.

[22] von Schütz, J.U., Bair, M., Gross, H.J., Langohr, U., Werner, H.P., Wolf, H.C., Schmeiβer, D., Graf, K., Göpel, W., Erk, P. and Others: The conducting salts of N, N'-dicyanoquinonediimine (DCNQI). *Synthetic Metals*, vol. 27, no. 3, pp. 249–256, 1988.

[23] Bauer, D., von Schütz, J.U., Wolf, H.C., Hünig, S., Sinzger, K. and Kremer, R.K.: Alloyed Deuterated Copper-DCNQI Salts: Phase Transitions and Reentry of Conductivity, Giant Hysteresis Effects, and Coexistence of Metallic and Semiconducting Modes. *Advanced Materials*, vol. 11, no. 11, pp. 829–834, 1993.

[24] Figgis, B.N. and Hitchman, M.A.: *Ligand Field Theory and Its Applications*. Wiley, 2000. ISBN 978-0-471-31776-0.

[25] Burkert, R., Helberg, H.W. and von Schütz, J.U.: Longitudinal and Transverse Conductivity in (2,5-DMe-DCNQI)$_2$Cu Fibres. *Synthetic Metals*, vol. 57, pp. 2519–2524, 1993.

[26] von Schütz, J.U., Gómez, D., Schmitt, H. and Wachtel, H.: Conductivity without spin-signal, spin signal without conductivity-switchable radical ion salts of deuterated Cu (DCNQI)$_2$. *Synthetic Metals*, vol. 86, no. 1, pp. 2095–2096, 1997.

[27] Kittel, C.: *Introduction to Solid State Physics*. Wiley, 2005.

[28] Erasmus, N.: *Ultrafast Structural Dynamics in 4H_b-$TaSe_2$ observed by Femtosecond Electron Diffraction*. Ph.D. thesis, 2013.

[29] Rossnagel, K.: On the origin of charge-density waves in select layered transition-metal dichalcogenides. *Journal of Physics: Condensed Matter*, vol. 23, no. 21, p. 213001, 2011.

[30] Kobayashi, A., Kato, R., Kobayashi, H., Mori, T. and Inokuchi, H.: The Organic π-Electron Metal System With Interaction Through Mixed-Valence Metal Cation: Electronic And Structural Properties Of Radical Salts Of Dicyano-Quinodiimine, (DMe-DCNQI)$_2$Cu And (MeCl-DCNQI)$_2$Cu. *Solid State Communications*, vol. 64, no. 1, pp. 45–51, 1987.

[31] Tomic, S., Jérome, D., Aumuller, A., Erk, P., Hünig, S. and von Schütz, J.U.: Pressure-temperature phase diagram of the organic conductor (DM-DCNQI)$_2$Cu. *Synthetic Metals*, vol. 27, no. 3, pp. 281–288, 1988.

[32] Kobayashi, H., Miyamoto, A., Kato, R., Sakai, F., Kobayashi, A., Yamakita, Y., Furukawa, Y., Tasumi, M. and Watanabe, T.: Mixed valency of Cu, electron-mass enhancement, and three-dimensional arrangement of magnetic sites in the organic conductors (R_1, R_2-N, N'-dicyanoquinonediimine)$_2$Cu (where R_1, R_2 = CH_3, CH_3O, Cl, Br). *Physical Review B*, vol. 47, no. 7, p. 3500, 1993.

[33] Kashimura, Y., Sawa, H., Aonuma, S., Kato, R., Takahashi, H. and Môri, N.: Anomalous pressure-temperature phase diagram of the molecular conductor (DI-DCNQI)$_2$Cu (DI-DCNQI= 2,5-DI-dicyanoquinonediimine). *Solid State Communications*, vol. 93, no. 8, pp. 675–679, 1995.

[34] Nogami, Y., Date, T., Oshima, K. and Arimoto, O.: Single crystal X-ray study of pressure-induced metal-insulator transition in (DMeDCNQI)$_2$Cu. *Synthetic Metals*, vol. 86, pp. 2073–2074, 1997.

[35] Schmitt, H., Wachtel, H., Wolf, H.C. and Stuttgart, U.: Light, pressure and stress induced phase transitions of deuterated Cu(DCNQI)$_2$ radical ion salts. *Synthetic Materials*, vol. 86, pp. 2257–2258, 1997.

[36] Nishio, Y., Tamura, M., Kajita, K., Aonuma, S., Sawa, H., Kato, R. and Kobayashi, H.: Thermodynamical Study of (DMe-DCQNI)$_2$ Cu System-Mechanism of Reentrant Metal-Insulator Transition. *Journal of the Physical Society of Japan*, vol. 69, no. 5, pp. 1414–1422, 2000.

[37] Eibenberger, S., Gerlich, S., Arndt, M., Mayor, M. and Tüxen, J.: Matter–wave interference of particles selected from a molecular library with masses exceeding 10000 amu. *Physical Chemistry Chemical Physics*, vol. 15, no. 35, pp. 14696–14700, 2013.

[38] Hecht, E.: *Optics*. Pearson Education, Inc.,, 2002.

[39] Kirkland, E.J.: *Advanced Computing in Electron Microscopy*. Springer Science & Business Media, 2010.

[40] Simon, S.H.: *The Oxford Solid State Basics*. OUP Oxford, 2013.

[41] David Palmer: CrystalMaker 9.2 and SingleCrystal 2.3.
Available at: `http://www.crystalmaker.com/index.html`

[42] Näsänen, R., Ojanpää, H., Tanskanen, T. and Päällysaho, J.: Estimation of temporal resolution of object identification in human vision. *Experimental Brain Research*, 2006.

[43] van Oudheusden, T., Pasmans, P.L.E.M., van der Geer, S.B., de Loos, M.J., van der Wiel, M.J. and Luiten, O.J.: Compression of subrelativistic space-charge-dominated electron bunches for single-shot femtosecond electron diffraction. *Phys. Rev. Lett.*, vol. 105, p. 264801, Dec 2010.

[44] Ahmed, E.T.M.: *A Near Infrared Femtosecond Laser Source for Observation of Charge transfer Processes in Semiconductors*. MSc thesis, Stellenbosch University, 2017.

[45] Rohwer, A.: *Introducing organic molecular crystals into ultrafast electron diffraction*. MSc thesis, Stellenbosch University, 2014.

[46] Haupt, K.: *Phase Transitions in Transition Metal Dichalcogenides studied by Femtosecond Electron Diffraction*. PhD thesis, Stellenbosch University, 2013.

[47] Smit, A.B.: *A New Femtosecond Electron Diffractometer for Structural Dynamics Experiments at Cryogenic Temperatures*. MSc thesis, Stellenbosch University, 2014.

[48] Kassier, G.H.: *Ultrafast electron diffraction : source development, diffractometer design and pulse characterisation*. Ph.D. thesis, Stellenbosch University, 2010.

[49] Sascha Meykopff: ASTRA - A Space Charge Tracking Algorithm.
Available at: `http://tesla.desy.de/ meykopff/`

[50] Kassier, G.H., Haupt, K., Erasmus, N., Rohwer, E., Von Bergmann, H., Schwoerer, H., Coelho, S. and Auret, F.: A compact streak camera for 150 fs time resolved measurement of bright pulses in ultrafast electron diffraction. *Review of Scientific Instruments*, vol. 81, no. 10, p. 105103, 2010.

[51] Pinteric, M., Vuletić, T., Lončarić, M., Petukhov, K., Gorshunov, B., von Schütz, J.U., Tomić, S. and Dressel, M.: Mott-Peierls phase in deuterated copper-DCNQI systems: a comprehensive study of longitudinal and transverse conductivity and ageing effects. *J. Phys.: Condens. Matter*, vol. 15, pp. 7351–7364, 2003.

[52] Huewe, F.: *Growth and Characterization of Radical Anion Salt Single Crystals*. MSc thesis, University of Wurzburg, 2012.

[53] Giannuzzi, L.A. and Stevie, F.A.: A review of focused ion beam milling techniques for TEM specimen preparation. *Micron*, vol. 30, pp. 197–204, 1999.

[54] Kamitsos, E., Chryssikos, G.D. and Gionis, V.: Spectroscopic Investigation of (2,5-DM-DCNQI$_2$M Materials in Bulk and Thin Film Forms. In: *Lower-Dimensional Systems and Molecular Electronics*, pp. 197–204. Springer, 1990.

[55] Gonzalez, R.C. and Woods, R.E.: *Digital Image Processing (3rd Edition)*. Prentice-Hall, Inc., Upper Saddle River, NJ, USA, 2006. ISBN 013168728X.

[56] Ishikawa, T., Hayes, S.A., Keskin, S., Corthey, G., Hada, M., Pichugin, K., Marx, A., Hirscht, J., Shionuma, K., Onda, K. *et al.*: Direct observation of collective modes coupled to molecular orbital–driven charge transfer. *Science*, vol. 350, no. 6267, pp. 1501–1505, 2015.

[57] Macrae, C.F., Edgington, P.R., McCabe, P., Pidcock, E., Shields, G.P., Taylor, R., Towler, M. and van de Streek, J.: Mercury: visualization and analysis of crystal structures. *Journal of Applied Crystallography*, vol. 39, no. 3, pp. 453–457, Jun 2006.

[58] Agar Scientific: Lacey-carbon TEM grids.
Available at: `http://www.agarscientific.com/lacey-carbon-films.html`

A. Sample preparation: TEM grid types

Our most commonly used TEM grid is the uncoated copper grid with 300 lines per inch (55 μm $\times$ 55 μm mesh holes) and this grid has yielded successful results for both sample preparation and during experiments. However, certain problems led us to experiment with different mesh coatings and line densities. For example, the sample "popping" whilst drying lead to the loss of many high quality samples.

This problem was addressed by considering grids with a higher line density (e.g., 1500 lines per inch) or with a thin film or coating on the mesh to support the sample. No satisfactory results were obtained using 1500 lpi grids; when imaged in the vacuum chamber, the diffraction patterns were of very low quality. The different mesh coatings trialled were Lacey carbon grids which are coated with a cobweb-like layer of carbon, as shown in Figure A.1. Formvar grids are coated with a thin transparent polymer film, which helped prevent "popping" of samples during drying. However, the diffraction patterns of such samples were also often of lower quality. The poor results obtained from both denser lpi grids and different coatings may be due to the fact that the extra support allowed low quality (e.g., damaged) samples to survive also, whereas only higher quality samples (e.g., without cracks) can survive the popping process on an uncoated copper grid. The formvar also produces an unwanted background in diffraction images, although the ring from Lacey carbon meshes is negligible. As some very high quality diffraction patterns have been obtained from samples on Lacey carbon, they remain an alternative to uncoated TEM grids for very brittle or delicate samples.

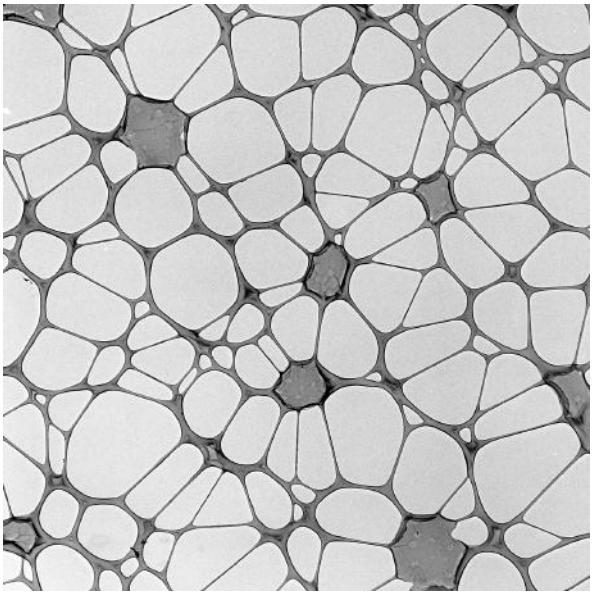

Figure A.1: The cobweb-like layer of holey carbon on so-called 'Lacey carbon' copper TEM grids. The carbon gives delicate samples extra support. Image from Agar Scientific [58].

B. Fitting the data

The time-resolved data can be modelled as the sum of an exponential decay and an exponential rise, with time constants of τ_1 and τ_2, and amplitudes c_1 and c_2, respectively:

$$\frac{\Delta I(t)}{I_0} = \begin{cases} 0, & \text{for } t < t_0 \\ c_1(1 - \mathrm{e}^{-t/\tau_1}) + c_2(1 - \mathrm{e}^{-t/\tau_2}), & \text{for } t \geq t_0 \end{cases} \tag{B.1}$$

To account for the finite temporal length of the electron pulse and other effects which will 'smear out' the data, we must convolve (B.1) with a Gaussian with a full width at half maximum (FHWM) determined by the response time of the system. Due to the simplicity of (B.1), the convolution can be done by hand and the analytical result can be found in terms of error functions:

$$\begin{aligned} \frac{\Delta I(t)}{I_0} = \frac{\sqrt{\pi}}{2} \cdot \frac{A}{\sigma} \Bigg[& c_1 \operatorname{erfc}\Big(-\sigma(t - t_0)\Big) \\ & - c_1 \, \mathrm{e}^{-(t-t_0)/\tau_1} \operatorname{erfc}\Big(-\sigma(t - t_0) + \frac{1}{2\sigma\tau_1}\Big) \\ & + c_2 \operatorname{erfc}\Big(-\sigma(t - t_0)\Big) \\ & - c_2 \, \mathrm{e}^{-(t-t_0)/\tau_2} \operatorname{erfc}\Big(-\sigma(t - t_0) + \frac{1}{2\sigma\tau_2}\Big) \Bigg]. \end{aligned} \tag{B.2}$$

MATLAB's built-in function `lsqcurvesfit` can then be used to optimise the parameters c_1, c_2, τ_1, τ_2 and t_0 given the user-defined fit shown in (B.2). The amplitude before time zero is also a free parameter. The optimised output parameters are given in the legend of each fit.

The MATLAB script for the fitting is given below. The inputs are the vectors of the experimental transient data (both time and intensity vectors), the response of the system in picoseconds, and an estimate for the starting point of the free parameters.

MATLAB code for fitting transients

```
function fitting_transients(time, data)
% the required inputs are a vector of the timesteps
% and a vector of the data for the measurement

before_t0 = mean(data(1:8));    % average before t0, e.g., over 8 data points
data = data - before_t0;        % bring data down to zero before t0
errbar = 0.12;                  % define size of error
fwhm = 1.2;                     % estimate temporal resolution of setup
sigma = 2*sqrt(log(2))/fwhm;    % turn fwhm into fitting parameter

% guess suitable initial parameters for the fit
c1 = -10e4;     % amplitude before t0
c2 = 10e4;      % amplitude of rise
c3 = 0;         % vertical offset
t0 = 0;         % time zero
t1 = 1;         % decay time
t2 = 5;         % rise time

% --- create vector of free parameters
p =  [   c1,   c2, t0,  t1, t2,   c3 ];
lb = [ -inf, -inf, -5,   0,  0, -inf ];         % lower bounds
ub = [  inf,  inf,  5, inf, inf, inf ];         % upper bounds

% --- define function that you're going to fit the data to
my_convolved_fit = @(p,t) 0.5* ...
    ( p(1)*erfc(-sigma*(t-p(3))) - ...
    p(1)*exp(-(t-p(3))/p(4)).*erfc(-sigma*(t-p(3))+1/(2*sigma*p(4))) + ...
    p(2)*erfc(-sigma*(t-p(3))) - ...
    p(2)*exp(-(t-p(3))/p(5)).*erfc(-sigma*(t-p(3))+1/(2*sigma*p(5)))) + p(6);

% --- use lsqcurvefit to optimise the initial guess for the paramters
p = lsqcurvefit(my_convolved_fit, p, time, data, lb, ub)
tt = linspace(time(1), time(end), 1001);  % vector of timesteps for fit
my_fit = my_convolved_fit(p,tt);          % create vector from fit parameters

figure(1), clf, hold on
h1 = errorbar(time, data, errbar*ones(length(time),1), 'k');
h2 = plot(time, data, 'k--o', 'MarkerFaceColor', 'k', 'LineWidth', 2);
h3 = plot(tt, my_fit, 'LineWidth', 3);
hold off
```